Development of Attitude Controllers and Actuators for a Solar Sail Cubesat.

by

Philip Hendrik Mey

Thesis presented in partial fulfilment of the requirements for the degree of Master of Science in Electronic Engineering at Stellenbosch University
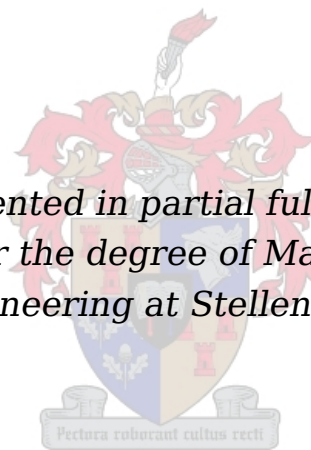
Supervisor: Prof. W.H. Steyn

March 2011

Declaration

By submitting this thesis electronically, I declare that the entirety of the work contained therein is my own, original work, that I am the sole author thereof (save to the extent explicitly otherwise stated), that reproduction and publication thereof by Stellenbosch University will not infringe any third party rights and that I have not previously in its entirety or in part submitted it for obtaining any qualification.

March 2011

Date: . . . .

Abstract

CubeSats are small, lightweight satellites which are often used by academic institutions due to their application potential and low cost. Because of their size and weight, less powerful attitude controllers, such as solar sails, can be used.

In 2010, the Japanese satellite, *Ikaros*, was launched to illustrate the usage of solar sails as a propulsion system. Similarly, by exploiting the solar radiation pressure, it is possible to use a solar sail, together with three magnetorquers, to achieve 3-axis attitude control of a 3-unit CubeSat.

Simulations are required to demonstrate the attitude control of a sun-synchronous, low Earth orbit CubeSat using a solar sail. To allow the adjustment of the solar sail, and its resulting torque, a mechanical structure is required which can be used to position the sail within two orthogonal axes. Although the magnetorquers and solar sail are sufficient to achieve 3-axis attitude control, the addition of a reaction wheel can be implemented in an attempt to improve this control.

Uittreksel

CubeSats is klein, ligte satelliete wat dikwels deur universiteite gebruik word weens hul lae koste en groot toepassings potensiaal. As gevolg van hulle gewig en grootte, kan minder kragtige posisie beheerders, soos byvoorbeeld sonseile, gebruik word.

Die Japannese satelliet, *Ikaros*, was in 2010 gelanseer om die gebruik van 'n sonseil as aandrywingstelsel te illustreer. Net so is dit moontlik om die bestraling van die son te gebruik, met behulp van 'n sonseil, en drie magneetstange om 3-as posisiebeheer op 'n 3-eenheid *CubeSat* te bekom.

Simulasies word benodig om die posisie beheer van 'n sonsinkrone, lae-aard wentelbaan *CubeSat* met 'n sonseil te demonstreer. 'n Meganiese struktuur word benodig vir die posisionering van die sonseil in twee ortogonale asse sodat die sonseil, en dus die ge-assosieerde draaimoment, verskuif kan word. Alhoewel die magneetstange en sonseil voldoende is om 3-as posisiebeheer te bekom, kan 'n reaksiewiel bygevoeg word om hierdie beheer te probeer verbeter.

Contents

List of Figures

List of Tables

Nomenclature

Abbreviations and Acronyms

AU	Astronomical Unit
CMOS	Complimentary Metal Oxide Semiconductor
CoM	Centre of Mass
CoP	Centre of Pressure
COTS	Commercial off the Shelf
DCM	Direction Cosine Matrix
ECI	Earth Centred Inertial
GCI	Geocentric Inertial
IC	Integrated Circuit
IGRF	International Geomagnetic Reference Field
ORC	Orbit Reference Coordinates
PCB	Printed Circuit Board
PD	Proportional Derivative
PID	Proportional Integral Derivative
PIC	Programmable Integrated Circuit
P-POD	Poly Picosatellite Orbital Deployer
Q-Feedback	Quantitative Feedback
RAAN	Right Ascension of the Ascending Node
RMS	Root Mean Square
RPY	Roll, Pitch, and Yaw
SBC	Satellite Body Coordinates
SCI	Spacecraft Centred Inertial
USART	Universal Synchronous Asynchronous Receiver Transmitter
VLSI	Very Large Scale Integration

Greek Letters

α	Angle of Incidence (Chapter 2), Atmospheric Velocity Incidence Angle Normal to the Solar Sail (Chapter 3)
ϵ	Specific Mechanical Energy
θ	Pitch Angle
λ	Wavelength
μ	Earth's Gravitational Constant (Chapter 3), Permeability (Chapter 4)
μ_r	Relative Permeability
μ_0	Permeability of Free Space
μ_{rod}	Magnetic Amplification of Ferromagnetic Rod
ν	True Anomaly
ρ	Atmospheric Density
ρ_a	Fraction of Absorbed Photons
ρ_s	Fraction of Specularly Reflected Photons
ρ_d	Fraction of Diffusely Reflected Photons
$\boldsymbol{\tau}$	Torque
ϕ	Roll Angle
ψ	Yaw Angle
ω	Argument of Perigee
$\omega^{B/I}$	ECI Referenced Angular Body Rates
$\omega^{O/B}$	ORC Referenced Angular Body Rates
$\tilde{\omega}(t)$	Instantaneous Angular Velocity
ω_{yref}	Reference Body Y-Axis Spin Rate
Ω	Right Ascension of the Ascending Node

Lowercase Letters

a	Acceleration (Chapter 2), Semimajor-axis (Chapter 3)
a_r	Acceleration due to Solar Radiation Pressure
c	Speed of Light
e	Eccentricity
f	Frequency
h	Planck's Constant (Chapter 2), Angular Momentum (Chapter 3)
i	Inclination

l	Total Winding Length
m	Mass
n	Mean Motion (Chapter 3), Number of Windings (Chapter 4)
$\boldsymbol{n}_{sail}$	Solar Sail Normal Unit Vector
p	Momentum
q	Attitude Quaternion
$\boldsymbol{q}_{err}$	Attitude Quaternion Error Vector
r	Reflection Factor (Chapter 2), Radius (Chapter 3)
$\vec{r}$	Distance Vector between Two Bodies
$\boldsymbol{r}_{m/p}$	Centre of Mass to Centre of Pressure Vector
r_{cntr_x}, r_{cntr_z}	Translation Stage Control Outputs
s	Arc Length
$\bar{\boldsymbol{s}}_B$	SBC Sun to Satellite Unit Vector
$\bar{\boldsymbol{s}}_I$	ECI Sun to Satellite Unit Vector
t	Time
v	Velocity
v_{cir}, v_{esc}	Circular, Escape Velocity

Uppercase Letters

A	Enclosed Area of Coil
A_{sail}	Area of Solar Sail
B_r	Remnant Magnetic Field Density
B_{sat}	Saturation Magnetic Field Density
$\boldsymbol{B}_{meas}$	Magnetometer Measured Magnetic Field Vector in SBC
$\boldsymbol{C}$	Direction Cosine Matrix
$\boldsymbol{C}^{O/I}$	ECI to ORC Transformation Matrix
$\boldsymbol{C}^{B/O}$	ORC to SBC Transformation Matrix
C_D	Satellite Drag Coefficient
E	Energy
F	Force
$\boldsymbol{F}_n$, $\boldsymbol{F}_t$, $\boldsymbol{F}_{Solar}$	Normal, Transverse, Full Solar Force Vectors
G	Universal Gravitational Constant

I	Direct Current
$\boldsymbol{I}_0$	Pre-Deploy Moment of Inertia Tensor
$\boldsymbol{I}$	Post-Deploy Moment of Inertia Tensor
$\boldsymbol{J}$	Moment of Inertia Matrix
K_D	Reaction Wheel Derivative Gain
K_P	Reaction Wheel Proportional Gain
K_Y	Y-axis Magnetorquer Derivative Gain
$\boldsymbol{L}$	Angular Momentum
M	Mean Anomaly (Chapter 3), Magnetic Moment (Chapter 4)
M_r	Remnant Magnetic Moment
M_{sat}	Saturation Magnetic Moment
$\boldsymbol{N}$	Total Torque Vector of Satellite
$\boldsymbol{N}_{AERO}$	Aerodynamic Disturbance Torque Vector
$\boldsymbol{N}_{GG}$	Gravity Gradient Disturbance Torque Vector
$\boldsymbol{N}_M$	Magnetic Control Torque Vector
$\boldsymbol{N}_{solar}$	Solar Sail Torque Vector
$\boldsymbol{N}_{wheel}$	Reaction Wheel Torque Vector
R_E	Earth's Equatorial Radius
T	Orbital Period
T_s	Sampling Time
V	Total Volume of Torquer Rod

Acknowledgements

First and foremost, I would like to thank my supervisor, professor Herman Steyn, for his continued support and input on my thesis work during my two year period at Stellenbosch University.

Thanks must also go to Wessel Croukamp for his knowledge and input on the mechanical systems which I have designed for this project.

Furthermore, I would like to thank the people at the Electronic Systems Laboratory, with whom I spent these last two years, for their suggestions and help.

And lastly, I would like to thank you, the reader, without whom these acknowledgements would be meaningless.

Chapter 1

Introduction and Problem Description

The small size and low mass characteristics of CubeSats reduces the control requirements of the attitude determination and control subsystem.

This decrease in weight and size also increases the effectiveness of the control systems which, in turn, allows the implementation of less powerful attitude controllers, such as solar radiation pressure controllers.

1.1 Objectives

The main objective of this thesis is to investigate the active 3-axis attitude control of a 3-unit CubeSat using a solar sail and three magnetorquers. This primary objective was further divided into the following goals.

- The theoretical possiblity of a solar sail controller must be illustrated with computer simulations.

- The practical feasibility of these controllers must be investigated.

  - A magnetic torquer rod must be designed and built for the CubeSat.
  - A structure that allows the positioning of the solar sail panel in two orthogonal axes must be designed and built.
  - The drive circuitry used to control these actuators, as well as to interface with a magnetometer, must be developed and implemented.

Finally, the hardware components must be tested using a hardware-in-the-loop simulation while possible improvements to the simulations, as well as mechanical and electronic hardware, should be considered.

1.2   Previous Work

One satellite has already been developed at Stellenbosch University and as a result the company *SunSpace* was established. The second satellite of South Africa, *Sumbandila*, was developed at *Sunspace*, and has been successfully launched in 2009. As such, a lot of satellite related control research has been done at the Electronic Systems Laboratory of the university.

With the development of the CubeSat, further research regarding the attitude control of small satellites is possible.

1.3   Thesis Layout

The layout of this thesis are as follows. Chapter 2 discusses the background information relating to CubeSats, solar sails, and reaction wheel technology while Chapter 3 introduces the mathematics that are used for the control algorithms and simulation design. The mechanical structure and magnetorquer designs, as well as the circuits and software that were developed and implemented, are described in Chapter 4.

Chapter 5 discusses the simulation setup and compares the simulated results focusing on a reaction wheel scenario against the basic solar sail scenario. Finally this thesis concludes, Chapter 6, with a concise summary of the achieved objectives in addition to providing recommendations regarding improvements and further research.

Chapter 2

Literature Study

Background information, relating to the research and technological development of satellites, is required before progress can be made. The three main subjects discussed within this chapter are satellites; solar sails; and attitude control devices.

Firstly, a short review of satellites is given with the emphasis placed on the decreasing size of satellites and the development of the CubeSat. An introduction of solar radiation pressure and the application fields of solar sails are then considered. Afterwards, the chapter is concluded with a discussion of attitude control devices which accentuates the use of reaction wheels.

2.1   The Evolution of Satellites

On 4 October 1957, the first artificial satellite, *Sputnik-1*, was successfully launched into space and entered an orbit around the Earth, [1]. Although it only provided information on the density and temperature of the upper atmosphere, it successfully illustrated the practical possibilities of satellites. The research and development of spacecraft and satellites, as well as other space technologies, have been steadily expanding ever since this original success.

Initially, the focus was placed on the development of communication, meteorology, and scientific exploration satellites. With these goals in mind, the capabilities and complexity of satellites increased necessitating the development of larger and heavier satellites. However, the size and weight of the satellites were still largely limited due to the capabilities of the rockets that were used as launch vehicles, [2].

One of the main advancements in launcher technology, was the development of multi-stage rockets. As the rocket's fuel is depleted, the empty fuel containers would be jettisoned thereby decreasing the weight of the rocket and increasing the power efficiency of the remaining fuel.

Even after overcoming the limitations associated with the launch vehicles, the deployment of satellites started to stagnate since only a few nations could meet the advanced

technological and high financial[1] requirements associated with the development and launch of large satellites.

The financial limitation remained a major deterrent until the 1970s, where improvements in the field of very large scale integration (VLSI) and the miniaturisation of electronics allowed the devolopment of smaller, lighter, and more powerful satellites.

The decrease in satellite weight and the integration of electronics lead to a noticeable decrease in development and deployment costs making it possible for more countries to become involved in the field of satellites. As technology advanced, the weight as well as the cost of satellites continued to decrease.

Modern materials and the capabilities of microelectronics have made it possible to construct satellites that weigh less than 1 kg. As such, satellites have been categorised into a variety of weight classes. The weight as well as the approximate cost[2] associated with these classes, [2], are illustrated in table 2.1.

Table 2.1 – Satellite Weight Classes

Category	Mass [kg]	Cost [£M]
Large Conventional Satellite	> 1000	> 100
Small Conventional Satellite	500 - 1000	25 - 100
Minisatellite	100 - 500	7 - 25
Microsatellite	10 - 100	1 - 7
Nanosatellite	1 - 10	0.1 - 1
Picosatellite	< 1	< 0.1

For the successful operation of a satellite, the following basic functions are required.

- The positioning of a satellite within an orbit, necessitates the presence of a propulsion system such as rocket motors. A satellite's lifetime is often limited to the amount of fuel available in these scenarios.

- The power system is essential to a satellite and most often consists of a combination of solar panels and batteries.

- To communicate with other satellites and ground based antennae, microwave or optical laser systems can be employed.

- The stabilisation of satellites is important since certain components, such as solar panels, cameras, and antennae, need to be aligned to operate effectively.

- Finally, the radiation and temperature range experienced in space neccessitates the use of temperature control and robust components.

---

[1]In the 1960s, the Apollo-program amounted to US$25.4 billion over a period of 11 years, [3].

[2]This is an approximation of the cost associated with the development and deployment of satellites as was available in the year 2003.

The immediate advantage of satellites above terrestrial communication systems, is that a larger coverage area is made possible due to the altitude of the satellites. In addition, satellites also have higher bandwidth capabilities while providing precision satellite-to-satellite communications. However, as expected, there are also inherent disadvantages associated with the use of satellite systems.

As the distance between communication points increase, the propagation delay associated with transmissions also increase and therefore satellite communication will remain relatively slower than ground-based communication systems. It is also more expensive to launch satellites into orbit, as mentioned previously, and the available bandwidth is gradually decreasing.

Satellites have played a major role in the advancement of our civilisation and technological infrastructure. Because of this, the utilisation of satellites have undergone various stages of development.

The first space missions were fueled by a technology race between the United States of America (USA) and Russia, formerly known as the Union of Soviet Socialist Republics (USSR), [4]. These technological demonstrations were succeeded by a need for scientific exploration, which was considered to be a primary concern and goal of the satellite developing nations.

Scientific experiments and observations continue to remain the goals of research institutions and even governments. However, the return on investment associated with satellite communication technologies has lead to the commercialisation of satellites by the private sector for entertainment purposes.

In addition to its communication capabilities, the utilisation of satellites have expanded to include navigation and tracking systems as well as internet access. Therefore the advantages of satellites are becoming ever more accessible by the general public.

As a result of these development stages, the application range of satellites has become vast and is still expanding each year as technologies improve. Satellites are often grouped into categories according to the main functionality of the specific satellite, as illustrated below.

Entertainment Oriented Satellites

> The advancements in communication satellites have lead to an effective global communication network, improving the communication possibilities of the current telephone and cellphone networks. With the additional data transmission capabilities, satellites have become a major influence in the entertainment industries. Television programmes, as well as high-speed internet, are examples of the current entertainment value provided by satellites.

Earth Observation Satellites

Improvements in camera technologies have increased the capabilities of Earth monitoring satellites. Meteorology satellites also fall into this category, making updated meteorological information available for weather forecasts. Global positioning satellites and the mapping of the Earth has lead to major improvements in the field of navigation systems which can be used over land and sea.

Scientific Exploration Satellites

The vast distances of space makes uncharted voyages a difficult and dangerous operation. Scientific exploration satellites are exploited not only for interplanetary missions and space exploration, but also to investigate the unknown effects of the space environment. Examples of scientific missions include the investigation of the effects of the solar wind and the Earth's magnetic field, as well as the exploration of other orbiting bodies.

The orbit location has a major influence on the efficiency of these various satellites. As expected, more fuel is required to obtain higher orbits thereby increasing the deployment cost of the satellite. In many cases higher orbits are unnecessary and as a result a variety of orbits have been established, each of which having different advantages that can be exploited depending on the designated functionality of a satellite.

Satellites within a geostationary orbit[3] are usually implemented for multipoint applications such as television broadcasts. Since they do not move relative to an observer on the Earth, these satellites provide a 24 hour view of a specific area and it is possible to communicate with them via stationary ground based antennae.

The altitude of the geostationary orbit enables a global view of meteorological events and provides a large coverage area. They are also aptly suited to provide tracking information and serve as a relay for satellites in a lower Earth orbit, [5].

To achieve a geostationary orbit, however, is a complex and expensive task wherein the satellite utilises an elliptical transfer orbit in order to achieve the necessary altitude. This results in an increase in propagation delay and a decrease in signal strength thereby reducing the effectiveness of point-to-point communications. Because of the unique properties of a geostationary satellite, the visibility of these satellites are greatly restricted within the polar regions.

Russia has been using highly elliptical orbits, also known as Molniya orbits, to overcome these visibility problems. The highly elliptical orbit lengthens the coverage time at its apocenter[4], therefore Molniya orbit satellites remain visible to a fixed position on the Earth for up to eight hours. A minimum constellation of three satellites are required to

---

[3]The geostationary orbit is located 35786 km above the equator where satellites revolve around the Earth at the same speed as the Earth rotates.

[4]The apocenter refers to the point furthest away from the Earth.

exhibit quasi-geostationary properties and provide continuous communication for a specific region. Since the satellite remains in motion, continuous pointing adjustments are required to the ground based antennae.

Molniya orbit satellites remain a reliable and cost effective alternative to provide continuous communication to polar regions. These satellites are also often used for Earth mapping and Earth observation applications as well as for scientific purposes, since the orbit enables the monitoring of the Earth's magnetosphere and the effects of solar-terrestrial interactions.

Constellations of Medium Earth Orbit (MEO)[5] satellites are used in Global Position System (GPS) applications in which 24 satellites are positioned in a circular orbit in such a way that a minimum of six of these satellites are continuously visible from any location on Earth, except in the polar regions, [5]. Users can accurately determine their location by using the information provided by these satellites. The Russian based navigation system, Global Navigation Satellite System (GLONASS), also utilise satellites in a MEO constellations to provide accurate positioning information.

MEO satellites provide a longer duration of visibilty, with orbital periods ranging between two and eight hours, while providing a larger coverage area than low earth orbit satellites. The altitude of these satellites still contribute greatly to the propagation delay experienced however the signal strength is better than that of geosynchronous (GEO) satellites.

The low Earth orbit (LEO)[6] consists of fast moving satellites close to the Earth. Satellites in a LEO typically provide fifteen to twenty minutes of visibility and a network of these satellites are required to be useful for communication and navigational purposes. Individual LEO satellites are however also employed for scientific and Earth monitoring applications.

The proximity of these satellites to the Earth results in a minimal propagation delay and very good signal strength. LEO satellites are therefore well suited for high resolution photography and point-to-point communications, such as the IRIDIUM system.

The speed at which these satellites revolve around the Earth makes it necessary to compensate for doppler effects. Another disadvantage associated with LEO satellites are that they have a relatively limited lifetime due to atmospheric drag and the gravitational pull of the Earth.

The lifetime of higher orbit satellites, where the effects of atmospheric drag are negligible, are primarily restricted to the lifetime of the electronic equipment or the amount of fuel remaining.

---

[5]Satellites with an altitude between about 10000 km and 20000 km are considered as MEO satellites.
[6]Satellites between 160 km and 2000 km are considered to be in LEO.

When taking these conditions into account, different design objectives and mission outcomes become apparent regarding the variety of Earth orbits, [2]. The costly nature of geostationary satellites contributes to the necessity of a longer operational lifetime to maximise efficiency. It is necessary for geostationary satellites to accommodate powerful transmitters, therefore the power requirements are higher which leads to a larger, heavier satellite. In addition, they also require greater processing capabilities due to the large coverage area. Stationkeeping capabilities are often necessary therefore additional fuel and radiation resistant electronics are required to extend the operational lifetime of these satellites.

In contrast, satellites that are deployed in low earth orbit often have a mission specific design but must remain cost effective when taking the operational lifetime into account. Because of the reduced transmitter requirements and lower communication traffic associated with these satellites the power consumption is drastically reduced. Smaller, light weight satellites are therefore more aptly suited for low earth orbit (LEO) situations.

In 1999, Stanford University and California Polytechnic State University formulated a set of specifications for the development of a picosatellite known as the CubeSat, illustrated in figure 2.1[7]. The CubeSat was designed to decrease the cost and development time of a satellite and thereby increase the accessibility to space, [6]. Consequently, the CubeSat has addressed the niche for small, scientific satellites required by academia.

Figure 2.1 – The Skeleton of a CubeSat

CubeSat The CubeSat is a cube satellite which can be classified as a small nanosatellite, or large picosatellite. The dimensions of a CubeSat are $10 \times 10 \times 10$ cm^3 and the weight of one unit is restricted to 1 kg.

---

[7]This skeleton is part of a CubeSat development kit available at http://www.cubesatkit.com/

The CubeSat has a modular design, meaning that two or even three CubeSats can be combined to form a satellite 20 or 30 cm in length, with a weight limit of 2 and 3 kg respectively. With the reduction in weight, the CubeSat inadvertently increases the effectiveness of various components, such as small reaction wheels, and it also provides advantages in the field of solar sailing, discussed in section 2.2.

A Poly Picosatellite Orbital Deployer (P-POD) was designed to house and deploy a maximum of three individual CubeSats[8]. The P-POD is responsible for the safety of the CubeSats during the launch process and is also used to establish these satellites within the desired orbit field.

The first CubeSat was launched in 2003 and during 2004 it was possible to develop and orbit a CubeSat for between US$65000 and US$ 80000, [7]. Because of the size and weight limitations introduced by the CubeSat design, commercial-off-the-shelf (COTS) components are widely used. These components also reduce production costs without impeding the satellites' capabilities.

The relatively low cost of these satellites, coupled with the usage of COTS components, has therefore established the CubeSat as a valuable learning platform for many academic institutions. As such, a variety of missions have been envisioned and employed to illustrate the use of CubeSats.

nCube-1 was a satellite built by several Norwegian universities, [8]. The main goal of this satellite was to monitor the movement of ships and also reindeer herds via Automatic Identification Transponders (AIS). A gravity gradient boom was used for passive control, while magnetic coils were employed to actively control the attitude of the satellite. A Kalman filter using a three-axis magnetometer and the current measurements from the solar panels was investigated for the attitude determination part of the attitude determination and control subsystem (ADCS), [9] and [10]. Unfortunately neither nCube-1 nor its successor nCube-2, [11], were operational because of launch and deployment failures, respectively.

The SwissCube was developed by *Ecole Polytechnique Fédérale de Lausanne* in association with various Swiss universities. The mission objective was to illustrate effective attitude control of a CubeSat by using a newly developed inertial wheel assembly, [12]. It was also intended to employ a camera to photograph the luminescence of atomic oxygen in high levels of the Earth's atmosphere. The satellite was launched in September 2009 and currently remains operational although, due to the current rotation speed of the satellite, it has not been possible to use the camera yet, [13].

The 2-Unit CubeSat, Cute-1.7, was developed at the Tokyo Institute of Technology to demonstrate the use of low cost commercial devices in orbit, [14]. An additional goal was the performance evaluation of the avalanche photodiode charged particle detector. The attitude determination of the satellite employed a three-axis gyrosensor; a three-axis

---

[8]This can either be three 1-Unit CubeSats; a combination of a 2-Unit and a 1-Unit CubeSat; or a single 3-Unit CubeSat.

magnetometer; a sun sensor and an Earth sensor. However, to illustrate its effectiveness, only three magnetic torquers were used for attitude control. The satellite was launched in February 2006 and operated successfully until it later deorbited in October 2009, [15].

CubeSats continue to provide an easily accessible platform for space experimentation and exploration at a reduced cost, thus also contributing to the advancement of space technologies.

2.2 Solar Sailing as a Propulsion System

Solar sailing is a form of a propellant-less attitude control and propulsion system. As the name implies, solar sailing refers to a method of sailing by using the energy from the Sun. To understand the nature of solar sailing, a brief introduction into solar energy is required.

The Sun in our solar system provides an almost inexaustible[9] amount of energy which is emitted in the form of electromagnetic radiation, [16]. The electromagnetic radiation carries energy and momentum which is imparted to matter with which the electromagnetic waves interact.

According to quantum physics, these electromagnetic waves are composed of discrete packets of energy called photons, [17]. Not only is the photon the unit for all forms of electromagnetic energy, but it is also the force carrier of the electromagnetic force, [18].

As an elementary particle, the photon follows the rules of quantum mechanics, [19], and photons can therefore be seen as transporters of energy. The energy and momentum of a photon can be calculated using equations 2.2.1 to 2.2.3[10].

$$c = f\lambda \tag{2.2.1}$$

$$E = h\omega = hf = \frac{hc}{\lambda} \tag{2.2.2}$$

$$\mathbf{p} = h\mathbf{k} \tag{2.2.3}$$

---

[9]Current theories estimate the remaining lifetime of our Sun at 5.5 billion years.

[10]Equation 2.2.2 is also referred to as the Planck-Einstein equation.

where $h = 6.626 \times 10^{-34}$ Js is Planck's constant; $c \approx 3 \times 10^8$ m.s^{-1} is the speed of light; λ is the wavelength; f is the frequency of the wave; and $\mathbf{k}$ is the wave vector.

The magnitude of the momentum can be calculated using

$$|p| = \frac{hf}{c}$$

The electromagnetic radiation from the Sun is perceived by humans in the form of thermal energy (heat) and visible light. This perception has lead to the discovery of the photoelectric[11] effect, [18], and the development of photovoltaic[12] devices such as solar cells, [20] and [21].

This accounts for the energy transferral from electromagnetic waves to matter with which they interact. By using solar cells, electricity can be generated when the solar cells are exposed to sunlight and thereby power can be provided to the satellite. To expand on the concept of the transferral of momentum we first need to refer to the classic laws of physics.

Newton's second law of physics, equation 2.2.4, can be expanded by using the definition that acceleration is equal to the change in velocity over a period of time, as illustrated in equation 2.2.5.

$$\vec{F} = m\vec{a} \tag{2.2.4}$$

$$\vec{F} = m\frac{\mathrm{d}\vec{v}}{\mathrm{d}t} \tag{2.2.5}$$

From classical mechanics, it is apparent that momentum is equal to the product between mass and velocity, illustrated in equation 2.2.6. When this is applied to equation 2.2.5, the resultant force becomes defined as a change in momentum over a period of time, illustrated in equation 2.2.7.

$$\vec{p} = m\vec{v} \tag{2.2.6}$$

$$\vec{F} = \frac{\mathrm{d}\vec{p}}{\mathrm{d}t} \tag{2.2.7}$$

---

[11]The photoelectric effect refers to the phenomenon in which electrons are emitted when certain metals are exposed to light.

[12]The photovoltaic effect describes the build-up of voltage between two electrodes because of the transferral of electrons between energy bands within the same material when it is exposed to light.

Therefore, when an electromagnetic wave is incident upon an object, a force is imparted upon the object. This is a very small force because the mass of a photon is infinitesimally small. Thus, to summarise, photons from the Sun that are incident on the satellite produce a small force, commonly referred to as solar radiation pressure, which pushes the satellite away from the Sun.

In 1903 the pressure of radiation was investigated and measured by Nichols and Hull, [22]. The effects of solar radiation pressure are more visible on satellites, as this small force acting upon a satellite results in a perturbation to the normal movement of the satellite. This becomes most apparent with satellites which have a large surface area that is exposed to the Sun wherein, as expected, more photons are incident upon the satellite resulting in a larger solar radiation pressure perturbation.

The magnitude of the solar radiation pressure on a satellite can be calculated using equation 2.2.8, [23].

$$|F| = K A_{sail} P \tag{2.2.8}$$

where K is a dimensionless number between 0 (transparent) and 2 (perfect mirror) indicating the degree of reflection; A_{sail} is the area exposed to the Sun; and P is the momentum flux from the Sun. At 1 astronomical unit (AU), the distance between the Sun and the Earth [13], the magnitude of the momentum flux is approximately 4.5×10^{-6} kg/ms^2. This allows one to rewrite equation 2.2.8 as equation 2.2.9 for satellites in the vicinity of the Earth, [23].

$$|F| = 4.5 \times 10^{-6}(1 + r)A_{sail} \tag{2.2.9}$$

with a reflection factor, r, between 0 (absorption) and 1 (specular reflection). According to [24], the acceleration arising from the solar radiation pressure can be calculated using equation 2.2.10.

$$a_R \approx -4.5 \times 10^{-6}(1 + r)A_{sail}/m \tag{2.2.10}$$

where m is the mass of the satellite. The negative sign indicates that the acceleration is experienced in a direction away from the Sun. It is apparent from this equation that the resulting acceleration is very small and it would take a long time to reach a noticeable velocity. However, the larger the exposed area and the lighter that the satellite is, the larger the acceleration due to solar radiation pressure would be. This is the principle on which solar sails are based.

Solar Sail A solar sail is effectively a large area covered in a thin film of reflective material which reflects the incoming photons from the Sun and thereby experiences an acceleration.

---

[13]1 AU $\approx 1.5 \times 10^{11}$ m

In this way, solar sails provide us with the means to convert the unwanted effects of solar radiation pressure into a method of propellant-less propulsion. An alternative method of describing solar sailing, is to compare a solar sail to the sail of a ship, the only difference being that solar radiation pressure is exploited for propulsion instead of the wind.

A perfect, flat solar sail would experience acceleration which is always normal to the exposed sail area. Such a perfect solar sail is not practically possible and it is therefore important to realise that the acceleration which occurs is due to a combination of forces that arises when the photons impinge upon the sail, [25].

A fraction ρ_a of the photons incident upon the solar sail is absorbed; a fraction ρ_s of the photons is specularly reflected; and a fraction ρ_d is diffusely reflected giving rise to equation 2.2.11, [26].

$$\rho_a + \rho_s + \rho_d = 1 \tag{2.2.11}$$

Depending on the absorption; reflection; and emission characteristics of the solar sail, the total force vector is comprised of three force components as illustrated in equation 2.2.12, [25].

$$\vec{F}_T = \vec{F}_a + \vec{F}_r + \vec{F}_e \tag{2.2.12}$$

These forces, which are associated with the incident photons, are composed as follow.

- $\vec{F}_a$ is a force generated due to the photons that are absorbed. The direction in which this force is experienced is therefore in the same direction as the incident photons.

- $\vec{F}_e$ is the force generated due to the re-emission of absorbed photons as thermal radiation. The direction of this force is normal to the surface of the solar sail and directed away from the incident photons.

- $\vec{F}_r$ is the force due to the reflected photons which can be further divided into specularly and diffusely reflected forces.

  - The directions of photons which are diffusely reflected is impossible to predict since these photons are uniformly scattered. This results in a force which is normal to the surface of the sail and is also directed in the opposite direction of the diffusely reflected photons.

  - When the angle of incidence, α, of the photons is equal to the angle of reflection, the photons are said to be specularly reflected. The force generated in this scenario is therefore directed in the opposite direction to that of the specularly reflected photons.

Figure 2.2 illustrates these force vectors as they act upon the solar sail.
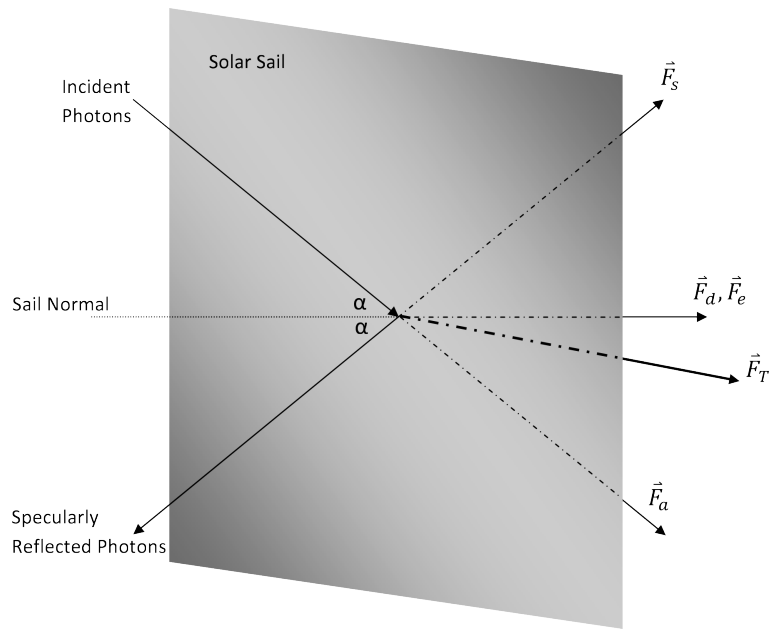
Figure 2.2 – Solar Radiation Pressure Forces on a Solar Sail

As can be seen from figure 2.2, the total force vector $\vec{F_T}$ is obtained by adding the various forces in vector format. The direction of this vector is biased in the direction of the absorbed force vector because slightly more photons are absorbed than they are reflected. This example is adequate to explain the effective forces generated by solar radiation pressure, however to increase the accuracy of the model one should take the billowing of the solar sail into account as well as the specific sail film characteristics.

The direction in which the satellite is accelerated can thus be altered by changing the orientation of the solar sail, and thereby the angle of incidence, α, at which the solar radiation pressure hits the solar sail.

Solar sailing was proposed as early as the 1920s by Fridrickh Tsander, and in the 1970s a *National Aeronautics and Space Administration* (NASA) mission was proposed in which an $800 \times 800 \ m^2$ solar sail would have been used to rendezvous with the Halley comet.

Although the mission was cancelled, it did awaken an interest for solar sailing which lead to the formation of the *World Space Foundation* (WSF), in 1979, and the *Union pour la Promotion de la Propulsion Photonique* (U3P), in 1981, [25]. Both of these groups attributed to the development and advancement of solar sailing.

The reasoning behind solar sailing is that although the forces acting upon the sail are very small, it provides a constant source of acceleration. This acceleration can eventually cause the velocity to, theoretically, approach the speed of light.

It is necessary, however, to realise that the acceleration that is imparted via the solar sail reduces as one moves away from the Sun. The opposite is also true, making solar sailing

14

highly efficient close to the Sun or similar fuel source.

The propellant-less aspect of solar sailing, makes it an excellent low cost alternative for a variety of application areas, [27]. Solar sails can be employed to transfer satellites between orbits and it could even replace the current propulsion systems that are used for satellite manoeuvring. They can also be used for interplanetary transportation or for the exploration of the solar system.

Although solar sails are more aptly suited for long distance missions where they have the capability to outperform any current chemical-based propulsion system, the effectiveness of using solar radiation pressure for attitude control and stationkeeping has already been researched and implemented, [26]. Solar sails can therefore maximise this attitude control capability of satellites while they are exposed to the Sun.

Until recently, satellites were heavy, large and costly equipment, thus necessitating a large solar sail[14] to prove solar sailing successful within a satellite's lifetime. Consequentially, the size of the solar sail made the development of the sail structure an engineering difficulty and the deployment of such a sail in space a very risky endeavour, [28].

The use of solar sailing was therefore mainly discouraged due to the unproven effectiveness of solar sailing in the space environment and the difficulties related to the development and deployment of large solar sails, not to mention the cost associated with a project with an unknown outcome.

However, with the recent improvements in solar sail technology and the development of the CubeSat, discussed in section 2.1, there has been renewed interest in solar sailing, [28]. Because of the light weight and small size of a CubeSat[15] it is possible to reduce the size of the solar sail, simplifying solar sail deployment, while still experiencing the verifiable effects of solar radiation pressure.

In 2008 a *NASA* solar sail mission, known as *NanoSail-D*, was scheduled to demonstrate the use of solar sails on nanosatellites, [29]. For the mission, it was proposed to use a 3-Unit CubeSat that contained the satellite payload as well as a 25 m^2 deployable solar sail, or solar kite. The main goal of this mission was to demonstrate the successful storage and deployment of a solar sail. Before the sail can be deployed, the satellite has to be stabilised to prevent the deformation of the sail material. Passive attitude control was considered in which permanent magnets would be used to detumble and align the satellite to the Earth's magnetic field. Simultaneously, the satellite would rely upon the effects of atmospheric drag for stabilisation. Unfortunately the satellite never reached orbit due to a launch failure with the Falcon 1 rocket, [30].

The utilisation of solar sails is an attractive concept for the investigation of the Earth's magnetotail. In August 2007, it was proposed to use a constellation of solar kites

---

[14]Such as the 800×800 m^2 sail proposed for the Halley comet mission.

[15]A 1 kg satellite with dimensions $10 \times 10 \times 10$ cm^3.

that would be permanently positioned within the Earth's magnetotail to provide continuous scientific returns, [28]. A simple, light and robust ADCS was investigated in which thrusters would be used for spin control. For the attitude determination a micro-electromechanical system (MEMS) low-power gyro, a star sensor, and a magnetometer was considered.

Simulations with a $40{\times}40$ m^2, 160 kg sailcraft have been done to advance sailcraft attitude control in order to enable solar sail spaceflights for the validation of stability and thrust-vector pointing performance, [26]. The use of windmill torques, generated by the assymetrical offset of solar array wings, have already been demonstrated with geosynchronous communication satellites such as OTS, TELECOM-1, and INMARSAT-2. To further the concept of three-axis control for sailcraft, three scenarios were proposed and investigated.

The use of small, reflective control vanes mounted at the spar tips in addition to a two-axis gimballed control boom, which would allow the change of the centre of mass location relative to the centre of pressure to be adjusted, enabled the simulation of a three-axis stabilised, square sailcraft. *Team Encounter* and *L'Garde* also proposed to use control vanes for the passive stabilization of a $76{\times}76$ m^2 sailcraft, [26].

For the *New Millennium Program Space Technology 7* sailcraft, a gimballed thrust vector control system, reaction wheels, and reaction jets were proposed to realise three-axis attitude control. A linear quadratic regulator design was employed to determine the controller gains and the effectiveness and practicality of a gimballed control system was illustrated through simulations.

To illustrate the possibility of a propellantless attitude control system, the shifting and tilting of sail panels were proposed for the *New Millenium Program Space Technology 6* mission. The objective was to develop a propellantless attitude control subsystem and algorithm to validate the concept of airplane-like control of a sailcraft, [26]. For this simulation, a non-linear proportional-integral-derivative (PID) control logic was employed with an attitude-error angle feedback loop.

To achieve three-axis attitude control, triangular sail panels which are supported by four booms were proposed. The outer two corners would be attached via constant-force springs to spreader bars, while the inner corner would be attached to a tether that feeds from a spool. The booms were also designed to be rotated in order to lift or lower the outer corners. The entire system would therefore consist of four triangular sail panels used for the aileron (roll), rudder (yaw), and elevator (pitch) of the sailcraft. Several challenging hardware design problems and technical issues were however associated with this design.

The first successful solar sail satellite, IKAROS, was launched in May 2010, [31] and [32]. The objective of this satellite, with its 200 m^2 solar sail, is to illustrate the acceleration and navigation possibilities of solar sails, [33]. The solar sail was deployed, and is kept flat, by exploiting the spinning motion of the satellite and the concept of centrifugal

forces. Because of this spinning motion, it is possible to avoid the use of rigid booms. The satellite was equipped with thrusters to adjust the angle of the sail, however the usage of liquid crystal displays that have an adjustable reflectivity will also be investigated. Although the solar sail has been successfully deployed at this point in time, it was not yet possible to ascertain the effectiveness and overall success of the solar sail.

The advantages and abilities of solar sailing therefore still remain greatly unproven and the opportunities to illustrate this breakthrough in technology continue to exist.

2.3 The Importance of Attitude Control Devices

The stability or alignment of a satellite is very important for the effective operation of various components. Communication antennae have to be pointed in the correct direction to function properly while cameras usually have to provide photographs of specific objects or areas. As such, a variety of attitude control devices have been developed and tested to successfully stabilise a satellite in orbit.

These devices produce the torque that is necessary for the attitude control of a spacecraft and are primarily achieved through the following techniques, [34].

The Earth's magnetic field.

> Magnetic torquer rods can be used to provide continuous, smooth control of satellites in close proximity to the Earth. The satellite's inclination as well as altitude affect the effectiveness of this control technique. The Earth's magnetic field strength is in the microtesla[16] range, thus the torques that can be generated are generally low which results in slow changes to a spacecraft's attitude.

Reaction forces produced by the expulsion of gas or ion particles.

> Reaction controllers, such as thrusters, usually provide torques of constant amplitude but with a modulated time duration. High levels of torque are possible with these controllers although it is usually limited to the amount of fuel available. Fast control manoeuvres are therefore possible, however smooth attitude changes are unfeasible because of the impulsive nature of these thrusters.

Solar radiation pressure on spacecraft surfaces.

> To date, solar torques have primarily been used to counteract disturbances with geostationary satellites. It is however possible to exploit solar radiation pressure for three-axis attitude control, as well as for propulsion systems, as discussed in section 2.2.

---

[16]On the surface of the Earth the field strength varies between approximately 25 and 60 μT, which decreases as the altitude increases.

Momentum exchange devices.

> Reaction wheels, momentum wheels, and control moment gyros are considered momentum exchange devices. These devices rotate masses within the spacecraft body to transfer momentum between different parts of the spacecraft. Very accurate control for moderately fast manoeuvres are possible with these devices.

Magnetorquers, reaction thrusters, and solar torques are categorised as inertial controllers since only the overall inertial angular momentum of a satellite is changed using these techniques, [34]. Momentum exchange devices, however only transfer the angular momentum between the different parts of a satellite without changing the overall inertial angular momentum of the satellite.

The exchange of angular momentum within the satellite relies on the law of conservation of angular momentum. This law states that the angular momentum of an object remains constant if there is no external, unbalanced torque acting upon it, [18]. Torque is defined as the change in angular momentum over a period of time, as illustrated in equation 2.3.1.

$$\boldsymbol{\tau} = \frac{\mathrm{d}\mathbf{L}}{\mathrm{d}t} \tag{2.3.1}$$

where $\boldsymbol{\tau}$ is the torque, $\mathbf{L}$ is the angular momentum, and t is the time. To achieve a torque, $\boldsymbol{\tau} = 0$, it is apparent that the change in angular momentum, $\mathrm{d}\mathbf{L} = 0$, which implies that the angular momentum should remain constant.

Thus if a symmetrical rotating body, located within a satellite, is accelerated about its axis of rotation the overall momentum of the satellite would not change. If the body is accelerated in the same direction as the satellite is spinning, the spinning motion of the satellite would decrease and vice versa. The momentum change is thus merely transferred from the rotating body to the satellite.

Momentum exchange devices are an attractive technique for attitude control since they do not require any fuel. The drawback associated with the conservation of angular momentum, is that momentum exchange devices cannot remove the excess angular momentum that accumulates due to external disturbances. This would lead to the saturation of the momentum wheels thereby preventing its attitude control capabilities. It is however possible to remove this excess momentum[17] by changing the overall momentum of the satellite.

Momentum and reaction wheels are two of the basic kinds of momentum exchange devices and are distinguished by their mode of operation, [34]. Momentum wheels are primarily used for providing a spacecraft with a momentum bias to obtain inertial attitude stability while reaction wheels are implented for fast and accurate attitude manoeuvres.

---

[17]This process is also known as dumping of the momentum.

The total angular momentum, $\mathbf{L}_{total}$, of a satellite is a combination of the angular momentum of the satellite, $\mathbf{L}_{sat}$, as well as the reaction wheel, $\mathbf{L}_{wheel}$, as illustrated in equation 2.3.2.

$$\mathbf{L}_{total} = \mathbf{L}_{sat} + \mathbf{L}_{wheel} \qquad (2.3.2)$$

The angular momentum, of which the magnitude can be calculated using equation 2.3.3, is defined as the product between the object's mass, m, velocity v, and distance from the rotation axis, r, [18].

$$|L| = mvr \qquad (2.3.3)$$

As can be seen from this relationship the mass of the reaction wheel is an important factor in calculating the angular momentum capabilities of the wheel. This implies that a heavier reaction wheel would produce a larger angular momentum than a lightweight wheel. However small, low mass reaction wheels can be successfully implemented for the attitude control of low mass satellites because of the relatively small weight difference.

The Hubble Space Telescope, launched April 1990, utilises four reaction wheels, weighting 45 kg each, to accurately point at a target galaxy or object to be photographed, [35] and [36]. However smaller, lightweight reaction wheels have been employed throughout the *Canadian Advanced Nanospace eXperiment Program* (CanX) range of satellites, [37] and [38].

The applicability and effectiveness of reaction wheels are therefore not limited to the weight class of a satellite, but rather by the required attitude control performance and application field of a satellite.

Chapter 3

Theoretical Knowledge

Theoretical knowledge is critical for the interpretation and implementation of satellite systems, especially within simulations. This chapter discusses the theoretical knowledge that is implemented in the satellite simulation with the focus placed on the proposed CubeSat's design. Most of the formulae used here are therefore, as indicated, only applicable to circular orbits.

A satellite's orbit and its movement through this orbit is discussed first. Then the interpretation methods, such as attitude reference frames and attitude representations, used to describe a satellite's motion are introduced.

After this basic overview, the mathematics used for attitude determination and propogation are represented. The attitude determination and control subsystem is also defined with a description of various sensors and actuators, as well as estimation and control techniques.

Finally, the chapter concludes with details regarding the proposed CubeSat simulation featuring the specific orbital elements, torques, and ADCS.

3.1   The Application of Astrodynamics

Astrodynamics describes the motion of natural and artificial satellites in space. The movement of the planets around the Sun, or an artificial satellite around the Earth are based on Kepler's three laws of planetary motion, [24].

- The orbit of each planet is an ellipse, with the Sun at one focus.

- The line joining the planet to the Sun, sweeps out equal areas in equal times.

- The square of the period of a planet is proportional to the cube of its mean distance from the Sun.

These laws can thus be used to develop a model that illustrates the motion of a satellite orbiting the Earth.

3.1.1 The Orbital Movement of Satellites

The elliptical orbits of planets are mathematically explained by Newton's Law of Universal Gravitation[1], equation 3.1.1, which states that two bodies attract each other with a force directly proportional to the product of their masses and inversely proportional to the square of the distance between them.

$$\vec{\mathbf{F}} = \frac{-GMm}{r^2} \cdot \frac{\vec{\mathbf{r}}}{r} \tag{3.1.1}$$

where $\vec{\mathbf{F}}$ is the gravitational force; G is the universal gravitational constant; M is the mass of one of the bodies; m is the mass of the second body; $\vec{\mathbf{r}}$ is the distance vector between the two bodies; and r is the magnitude of the distance vector.

Using this information we can also determine the relative motion of a satellite as it orbits the Earth. The acceleration vector of a satellite can be calculated by combining Newton's second law, equation 2.2.4, with the the law of gravitation, equation 3.1.1, [23]. The resultant equation can be further simplified as illustrated in equation 3.1.2.

$$m\vec{\mathbf{a}} = \frac{-GMm}{r^2} \cdot \frac{\vec{\mathbf{r}}}{r}$$

$$\vec{\mathbf{a}} + \frac{GM}{r^3} \cdot \vec{\mathbf{r}} = \vec{\mathbf{0}} \tag{3.1.2}$$

with the Newtonian gravitational constant, $G \approx 6.7 \times 10^{-11}$ m³kg⁻¹s⁻², and the mass of the Earth, $M = m_{earth} \approx 6.0 \times 10^{24}$ kg. It is known that acceleration is the second derivative of distance with respect to time, thus

$$\vec{\mathbf{a}} = \ddot{\vec{\mathbf{r}}}$$

while the Earth's gravitational constant, $\mu = GM = 3.986 \times 10^{14}$ m³s⁻². When applying this knowledge to equation 3.1.2, one can derive the two-body equation of motion which describes the acceleration vector of a satellite orbiting the Earth, equation 3.1.3.

$$\ddot{\vec{\mathbf{r}}} + \frac{\mu}{r^3} \cdot \vec{\mathbf{r}} = \vec{\mathbf{0}} \tag{3.1.3}$$

In the derivation of equation 3.1.3, it was assumed that the Earth is spherically symmetric; the Earth's mass is much greater than that of the satellite; the Earth and the satellite are the only two bodies in the system; and gravity is the only force acting upon

---

[1]Albert Einstein's general theory of relativity accounted for the discrepancy in Newton's theory with regards to the orbit of Mercury, which was confirmed by Arthur Eddington in 1919.

the system. A conic section can be exploited to solve equation 3.1.3 and elaborate on the satellite's orbit.

A conic section is a curve, formed by the intersection of a plane passing through a right circular cone, [24]. The polar equation of such a conic section, equation 3.1.4, provides a solution to the two-body equation of motion, equation 3.1.3.

$$r = \frac{a(1 - e^2)}{1 + e \cos \nu} \tag{3.1.4}$$

where a is the semimajor axis of the orbit; e is the eccentricity; and ν is the true anomaly or the angle between the satellite and the perigee[2]. These elements are discussed in detail in section 3.1.2.

The four conic sections[3] can be defined in terms of the eccentricity and are used to describe the orbits of a satellite as follow, [24].

- A closed elliptical orbit is obtained when $0 < e < 1$.

- The circular orbit is similar to an elliptic orbit with the foci collocated, thus $e = 0$.

- To leave the Earth altogether, a parabolic trajectory is chosen where $e = 1$ resulting in an open orbit.

- For interplanetary missions a hyperbolic trajectory, with $e > 1$, is used.

Another important property of the satellite orbit is the orbital velocity, which can be obtained by investigating the energy of the satellite. Because of the restricted two-body problem approach, the specific mechanical energy, ϵ, and specific angular momentum, $\mathbf{h}$, remain constant. The specific mechanical energy is simply the sum of the satellite's kinetic and potential energies per unit mass, equation 3.1.5, [23] and [24].

$$\begin{aligned} E_{kinetic} + E_{potential} &= \frac{mv^2}{2} - \frac{\mu m}{r} \\ \epsilon &= \frac{v^2}{2} - \frac{\mu}{r} \\ &= \frac{-\mu}{2a} \end{aligned} \tag{3.1.5}$$

The specific angular momentum can be obtained by calculating the cross product of the position and velocity vectors, as illustrated in equation 3.1.6.

$$\mathbf{h} = \mathbf{r} \times \mathbf{v} \tag{3.1.6}$$

---

[2]The perigee refers to the point of the orbit which is closest to the Earth.
[3]The circle, ellipse, parabola and hyperbola are considered to be conic sections.

By rearranging equation 3.1.5, one obtains the *Vis Viva* equation that is used to calculate the orbital velocity of a satellite, equation 3.1.7.

$$v = \sqrt{\mu\left(\frac{2}{r} - \frac{1}{a}\right)} \tag{3.1.7}$$

From this equation it is apparent that the speed of a satellite varies according to its distance r, with the satellite moving slowest at apogee and fastest at perigee. For a circular orbit, the distance and semimajor axis are equal, $r = a$, therefore the orbital velocity does not change and equation 3.1.7 simplifies to

$$v_{cir} = \sqrt{\frac{\mu}{r}} \approx 631.3481 r^{-1/2} \quad [\text{km.s}^{-1}]$$

For certain satellite missions it may be required to leave Earth's orbit. The escape velocity required to achieve this can be calculated by investigating the parabolic orbit case in which the semimajor axis approaches infinity, $a = \infty$, thus reducing equation 3.1.7 to

$$v_{esc} = \sqrt{\frac{2\mu}{r}} \approx 892.8611 r^{-1/2} \quad [\text{km.s}^{-1}]$$

If the orbital velocity is known, it is possible to calculate the period of a satellite in a circular orbit. From geometry it is clear that the arc length, s, of a circle is the product of the radius, r, and the angle of the arc, θ, therefore

$$s = r\theta$$

Furthermore, in physics it has been shown that the distance, s, is the product between the velocity, v, and the period of time, t, giving

$$s = vt$$

Combining these equations with the equation for the circular velocity, where $r = a$, we can obtain the orbital period, T, for a circular orbit, illustrated in equation 3.1.8.

$$r\theta = v_{cir}t$$

$$a(2\pi) = v_{cir}T$$

$$T = 2\pi a \sqrt{\frac{a}{\mu}}$$

$$= 2\pi\sqrt{\frac{a^3}{\mu}} \tag{3.1.8}$$

The orbital period of a circular orbit, equation 3.1.8, could also have been obtained by relating the specific angular momentum to the equation for the area of an ellipse, [23]. Therefore, by using Newton's and Kepler's laws it is possible to describe the orbital motion of a satellite in terms of its orbital properties.

3.1.2 The Elements of an Orbit

The orbit of a satellite can be completely described by six elements, known as the classical orbital elements. The geocentric inertial (GCI) coordinate system, section 3.2.1, is used to define these elements as follow, [23], [24] and [39].

The semimajor axis, a [km].

> The semimajor axis indicates the size of the ellipse and thus the size of the satellite's orbit. For a circular orbit, this element also indicates the altitude of the satellite.

The eccentricity, e.

> This dimensionless element describes the shape, or "flatness", of the ellipse. This is used to identify whether an orbit is circular, elliptical, parabolic or hyperbolic.

The inclination, i [°].

> The tilt of the orbit plane, that is the counter-clockwise angle between the equator and the orbit plane, is called the inclination of an orbit. A prograde orbit, in which the satellite is moving with the Earth's rotation, is obtained when $0° \leq i < 90°$. When a satellite moves opposite to the rotation of the Earth, it is called a retrograde orbit with $90° < i \leq 180°$.

The Right Ascension of the Ascending Node (RAAN), Ω [°].

> This is the angle measured from the vernal equinox to the ascending node[4]. The RAAN describes the orientation of the orbital plane with respect to the sun, and therefore the solar illumination of the satellite. The initial RAAN of an orbit is determined by the time of launch on a given day, giving rise to launch windows as discussed in section 3.1.3.

The argument of perigee, ω [°].

> The orientation of the orbit within its own orbit plane is defined with the argument of perigee, which also describes the latitude of the apogee and perigee. This angle is measured in the direction of motion of the satellite from the ascending node to the perigee point on the line of apsides.

The true anomaly, ν [rad].

> The true anomaly of the satellite varies with time and indicates where the satellite is along its orbit, relative to the perigee direction. Thus, this is the angle measured at the primary focus, between the perigee and the satellite's radius vector.

---

[4]The ascending node is the point of intersection at which the satellite crosses the equator from the south to the north.

The orbital elements, except for the eccentricity and semimajor axis, are illustrated in figure 3.1 to give a visual representation of their descriptions[5].
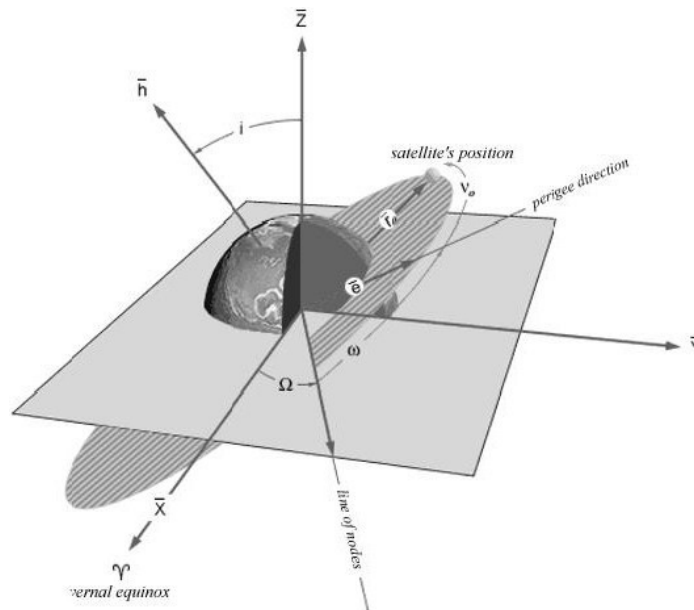
Figure 3.1 – Representation of the Orbital Elements

To accurately determine the true anomaly for an elliptical orbit, the mean anomaly, M, as well as the eccentric anomaly, E is required. This is because the true anomaly sweeps through 2π radians at differing speeds within an orbit. However, in the case of a circular orbit, where $e = 0$, the true anomaly is equal to the mean anomaly, equation 3.1.9, [24].

$$M = M_0 + n(t - t_0) \tag{3.1.9}$$

where M_0 is the mean anomaly at starting time t_0; and $n = \frac{2\pi}{T}$ is the mean motion, which is the average angular velocity of the satellite. It is apparent that the true anomaly changes over time, while it seems that the other orbital elements remain constant. However, unwanted perturbations exist which affect the "normal" orbital motion of a satellite. As a result, the orbital elements, and thus the orbit itself, changes slowly as time progresses.

3.1.3   The Effects of Continual Disturbances

The perturbations that are experienced by a satellite cannot be ignored and must be counteracted to ensure the continuous performance of most satellites. To achieve this, information regarding the perturbations are required to produce an accurate model that describe the perturbations' effects.

---

[5]This figure was adapted from http://spaceflight.nasa.gov/realdata/elements/graphs.html, 2010.

Secular variations represent a linear variation in orbital elements, causing them to continuously increase or decrease. Secular variations have long-term effects on the orbital motion but to precisely determine the orbit, periodic variations should also be taken into account, [24]. These are either short-period variations, with a period less than the orbital period, or long-period variations, with a period longer than the orbital period.

The primary causes of these perturbations are third-body gravitational forces; the non-spherical mass distribution of the Earth due to its oblateness; atmospheric drag in LEO; and solar radiation pressure.

Third-body gravitational forces, attributed to the Sun and the Moon, cause periodic as well secular variations in the orbital elements. These secular effects are greatest on the RAAN and argument of perigee elements and can be calculated, via approximations for a circular orbit with $e \approx 0$, using equations 3.1.10 to 3.1.13, [24].

$$\dot{\Omega}_{Moon} = -0.00338 \left(\cos i \right) / n \tag{3.1.10}$$

$$\dot{\Omega}_{Sun} = -0.00154 \left(\cos i \right) / n \tag{3.1.11}$$

$$\dot{\omega}_{Moon} = 0.00169 \left(4 - 5 \sin^2 i \right) / n \tag{3.1.12}$$

$$\dot{\omega}_{Sun} = 0.00077 \left(4 - 5 \sin^2 i \right) / n \tag{3.1.13}$$

where $\dot{\Omega}_{Moon}$, $\dot{\Omega}_{Sun}$, $\dot{\omega}_{Moon}$ and $\dot{\omega}_{Sun}$, in [°/day], are the secular changes to the RAAN and argument of perigee, respectively, caused by the Moon and the Sun as indicated; i is the orbital inclination; and n is the number of orbit revolutions per day.

The non-spherical mass distribution of the Earth also causes dominant secular variations in the RAAN and argument of perigee elements. The J_2 zonal coefficient of the geopotential function represents these effects as illustrated in equations 3.1.14 and 3.1.15, [23].

$$\dot{\Omega}_{J_2} = -1.5 n J_2 \left(\frac{R_E}{a} \right)^2 \frac{\left(\cos i \right)}{\left(1 - e^2 \right)^2} \tag{3.1.14}$$

$$\dot{\omega}_{J_2} = 0.75 n J_2 \left(\frac{R_E}{a} \right)^2 \frac{\left(4 - 5 \sin^2 i \right)}{\left(1 - e^2 \right)^2} \tag{3.1.15}$$

where n is the mean motion in [°/day]; R_E is the Earth's equatorial radius; a is the semimajor axis in [km]; e is the eccentricity; i is the inclination; and $\dot{\Omega}_{J_2}$ and $\dot{\omega}_{J_2}$ are the changes to the RAAN and argument of perigee, in [°/day], caused by the Earth's oblateness.

Atmospheric drag is directly related to atmospheric density, thus this perturbation is only relavent for satellites below a height of 1000 km. Atmospheric drag causes the semimajor axis of a satellite in a circular orbit to decrease. Consequently, the speed and effects of atmospheric drag increases resulting in the eventual re-entry of a satellite. The change in semimajor axis per revolution for a circular orbit can be calculated using equation 3.1.16, [24].

$$\Delta a_{rev} = -2\pi \left(C_D A/m \right) \rho a^2 \tag{3.1.16}$$

where C_D is the satellite's drag coefficient; A is the cross-sectional area; m is the satellite's mass; and ρ is the atmospheric density.

Solar radiation pressure causes periodic perturbations, but have recently been exploited by using solar sails, as discussed in section 2.2. It is noticable, for satellites not equipped with a solar sail, that the acceleration due to atmospheric drag is dominant below a height of 800 km while the acceleration due to solar radiation pressure is greater above 800 km.

Although perturbations continuously affect the orbital motion of a satellite, they can be managed and even exploited. A sun-synchronous orbit, in which the satellite is constantly illuminated by the Sun, can be obtained by letting the orbit plane rotate at the same angular velocity as the Earth moves around the Sun, [23]. That is to say, by ensuring that the satellite's RAAN rate of change is equal to 0.986 °/day, using equation 3.1.14.

Similarly, by adjusting the time and date of launch, it is possible to obtain a predetermined RAAN and, by varying the launch location, inclination angle for a satellite. These launch windows are exploited to reduce the need for expensive orbital manoeuvres that may be required to install a satellite within a desired orbit.

The presence of orbital perturbations has an effect on a satellites' attitude and must therefore be controlled, actively or passively, to ensure the continuous and successfull operation of satellites.

3.2   The Attitude of Satellites

A coordinate system must be defined in order to understand the apparent motion of satellites and the effects which perturbations have upon their orbital movement. Although the GCI coordinate system was used to describe the classical orbital elements, there exist various coordinate systems, or attitude reference frames. The choice of an appropriate coordinate system often provides useful insight into a problem while the probability of causing errors is also reduced.

3.2.1 The Definition of Attitude Reference Frames

The coordinate systems, or attitude reference frames, that are used in space applications are defined by two properties, [24].

- The location of the centre of the coordinate system which describes the origin, or position, from where the system is observed.

- The object or direction that the coordinate system is fixed with respect to.

These properties are chosen for a specific problem that needs to be investigated. As a result, a variety of coordinate systems exist with common centre locations but different reference directions, and vice versa.

For problems pertaining to the geometry on the surface of the Earth or orbit analysis, the Earth is commonly chosen as centre location, [24]. Whereas, the satellite can be chosen as centre location to view the apparent position and motion of objects from the satellite's point of view. It is also useful to choose a specific satellite component as the centre when obstructions in its field of view need to be observed.

To simplify the mathematical equations of motion, the coordinate system can be fixed: with respect to inertial space; to the direction of the Earth; or to the spacecraft, to name but a few examples.

Although the choice of a coordinate system might seem arbitrary, it is often advantageous to use different reference frames depending on the mission application. Choosing the "correct" coordinate system may increase insight into a problem and even simplify attitude calculations.

The Earth centred inertial frame, used in section 3.1.2, is discussed below. In addition the inertial; orbit; and body reference frames, centred on the centre of mass of the satellite, are also discussed here, [23].

The geocentric inertial (GCI) reference frame.

>   The Earth is centred in the GCI reference frame with the x-axis pointing towards the vernal equinox; and the z-axis pointing towards the north pole. The y-axis completes the right hand set as illustrated in figure 3.2. It is primarily used for orbit analysis; astronomy and inertial motion.
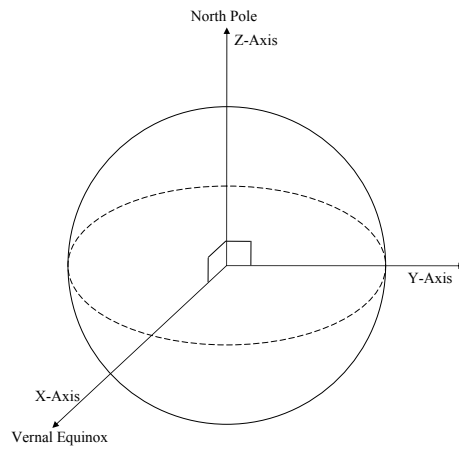
Figure 3.2 – GCI Reference Frame

The spacecraft centred inertial (SCI) reference frame.

> The SCI reference frame is fixed in inertial space, as illustrated in figure 3.3, with the satellite at its centre and the z-axis pointing in the direction of apogee. It is commonly used for the satellites' dynamic equations of motion.
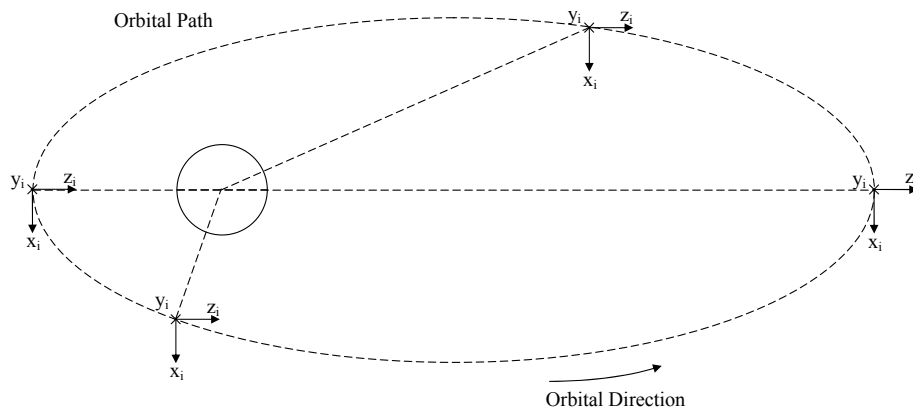
Figure 3.3 – SCI Reference Frame

The orbit reference coordinates (ORC) frame.

> The ORC frame is fixed to the orbit position and rotates with the orbital motion as illustrated in figure 3.4. This reference frame, also known as the Local Vertical/Local Horizontal (LVLH) or Roll, Pitch, Yaw (RPY) reference frame, is often used for the spacecraft attitude where the Z-axis conveniently points towards the centre of the Earth.
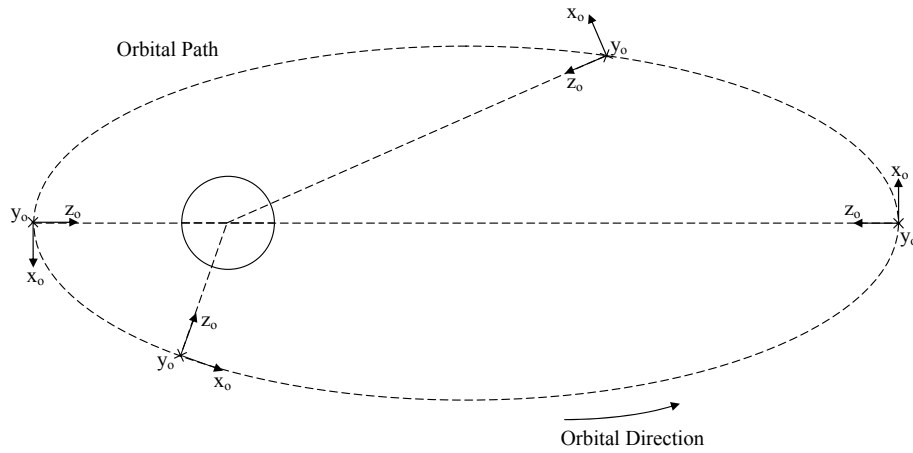
Figure 3.4 – ORC Reference Frame

The satellite body coordinates (SBC) reference frame.

> Specifying the orientations of satellite components such as actuators and sensors, as well as their measurements, are usually done with the SBC reference frame. In this scenario, the centre is fixed to the spacecraft body and the axes are chosen to be aligned with certain sensors or other satellite components. For the solar sail cubesat, the x and z-axes were chosen to be aligned with the sail translation panel and the y-axis was aligned along the length of the satellite body, illustrated in figure 3.5 (not to scale).
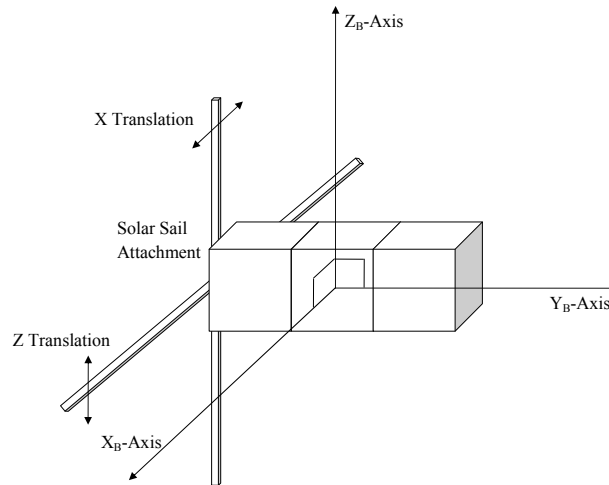
Figure 3.5 – SBC Reference Frame

With the advantages and applications attributed to these coordinate systems, it becomes commonplace that a variety of reference frames are employed for a single satellite mission. Each of the reference frames are mathematically correct, however to switch between the different attitude coordinate systems requires a representation of the attitudes that describe the motion of a satellite.

3.2.2 The Representation of Attitude

As there exist various attitude reference frames, the attitude of a satellite can be represented by the orientation of one reference relative to another. Consequently, there are also different methods to represent the attitude of a satellite.

The direction cosine matrix (DCM) is one of these methods and will be discussed using figure 3.6, which illustrate the reference frames A and B, each of which have a right hand set of orthogonal vectors $\vec{a}_1, \vec{a}_2, \vec{a}_3$ and $\vec{b}_1, \vec{b}_2, \vec{b}_3$, respectively.
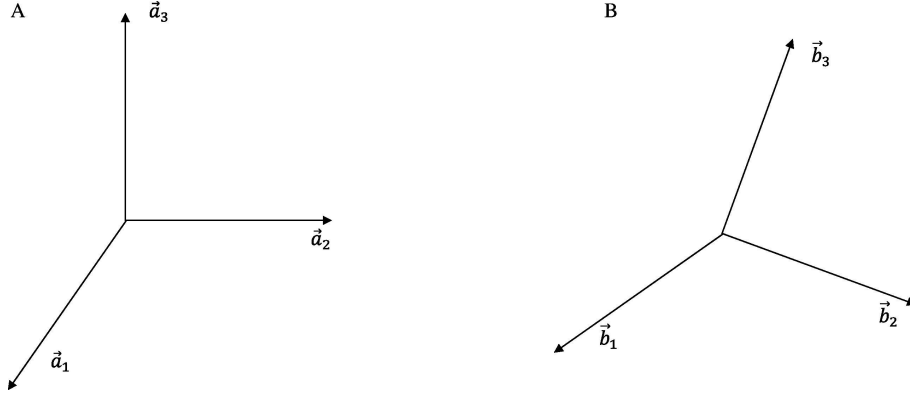
Figure 3.6 – DCM Example Reference Frames A and B

The reference frames were chosen arbitrarily for this example, however the same concept applies, for example, to the body and orbit reference frames. The basis vectors of B can be expressed in terms of A as illustrated in equation 3.2.1.

$$\mathbf{b}_1 = C_{11}\mathbf{a}_1 + C_{12}\mathbf{a}_2 + C_{13}\mathbf{a}_3$$
$$\mathbf{b}_2 = C_{21}\mathbf{a}_1 + C_{22}\mathbf{a}_2 + C_{23}\mathbf{a}_3$$
$$\mathbf{b}_3 = C_{31}\mathbf{a}_1 + C_{32}\mathbf{a}_2 + C_{33}\mathbf{a}_3 \tag{3.2.1}$$

where the direction cosine, $C_{ij} = \mathbf{b}_i \cdot \mathbf{a}_j$, is the cosine of the angle between $\mathbf{b}_i$ and $\mathbf{a}_j$. The direction cosine matrix $\mathbf{C}^{B/A}$ can thus be written as

$$\begin{bmatrix} \mathbf{b}_1 \\ \mathbf{b}_2 \\ \mathbf{b}_3 \end{bmatrix} = \begin{bmatrix} C_{11} & C_{12} & C_{13} \\ C_{21} & C_{22} & C_{23} \\ C_{31} & C_{32} & C_{33} \end{bmatrix} \begin{bmatrix} \mathbf{a}_1 \\ \mathbf{a}_2 \\ \mathbf{a}_3 \end{bmatrix} = \mathbf{C}^{B/A} \begin{bmatrix} \mathbf{a}_1 \\ \mathbf{a}_2 \\ \mathbf{a}_3 \end{bmatrix} \tag{3.2.2}$$

Similarly, the direction cosine matrix $\mathbf{C}^{A/B}$, describing the orientation of the reference frame A relative to reference frame B, can be written as

$$\mathbf{C}^{A/B} = \left[\mathbf{C}^{B/A}\right]^{-1} = \left[\mathbf{C}^{B/A}\right]^T$$

because the direction cosine matrix is orthonormal. As a result, any vector that is represented in reference frame A can be transformed to reference frame B with the DCM.

Representing the attitude with the DCM produces no singularities and does not require the use of trigonometric functions, [23]. In addition, various direction cosine matrices can be multiplied in the case of successive rotations. The main disadvantage with regards to the DCM, is the existence of redundant parameters. DCMs are primarily used in the transformation of vector components between different reference frames.

The second method of attitude representation relies on three successive rotations about the axes of the rotated, body-fixed reference frame. These are called Euler angle rotations in which the first rotation can be about any body axis; the second rotation can be about either of the two remaining axes; and the third rotation is about either of the two axes not used for the second rotation, for example Euler 1-2-3 or Euler 3-1-3.

An Euler 2-1-3 rotation, illustrated in figure 3.7, is discussed in detail here. The first rotation is about the original Y-axis, Y_o, with a pitch angle θ after which a rotation about the new X-axis, X', with a roll angle ϕ is performed. The final rotation is about the final Z-axis, Z, with a yaw angle ψ.
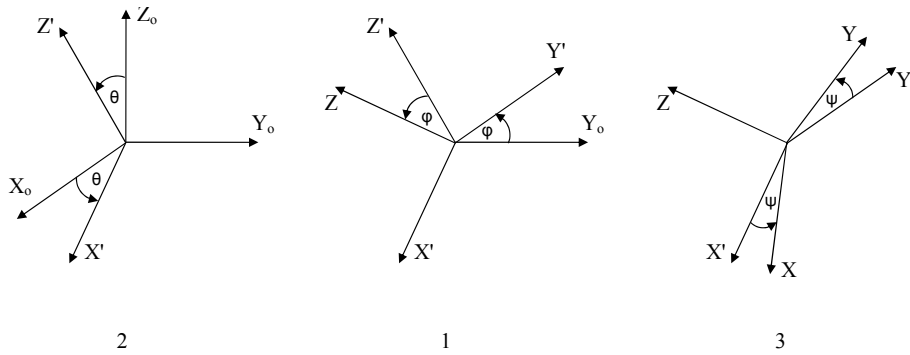
Figure 3.7 – Euler 2-1-3 Rotations

The mathematical process of this transformation is illustrated in equation 3.2.3.

$$
\begin{aligned}
\begin{bmatrix} \mathbf{a}_1' \\ \mathbf{a}_2' \\ \mathbf{a}_3' \end{bmatrix} &= \begin{bmatrix} \cos\theta & 0 & -\sin\theta \\ 0 & 1 & 0 \\ \sin\theta & 0 & \cos\theta \end{bmatrix} \begin{bmatrix} \mathbf{a}_1 \\ \mathbf{a}_2 \\ \mathbf{a}_3 \end{bmatrix} = \mathbf{C}_2^{A'/A}(\theta) \begin{bmatrix} \mathbf{a}_1 \\ \mathbf{a}_2 \\ \mathbf{a}_3 \end{bmatrix} \\
\begin{bmatrix} \mathbf{a}_1'' \\ \mathbf{a}_2'' \\ \mathbf{a}_3'' \end{bmatrix} &= \begin{bmatrix} 1 & 0 & 0 \\ 0 & \cos\phi & \sin\phi \\ 0 & -\sin\phi & \cos\phi \end{bmatrix} \begin{bmatrix} \mathbf{a}_1' \\ \mathbf{a}_2' \\ \mathbf{a}_3' \end{bmatrix} = \mathbf{C}_1^{A''/A'}(\phi) \begin{bmatrix} \mathbf{a}_1' \\ \mathbf{a}_2' \\ \mathbf{a}_3' \end{bmatrix} \\
\begin{bmatrix} \mathbf{b}_1 \\ \mathbf{b}_2 \\ \mathbf{b}_3 \end{bmatrix} &= \begin{bmatrix} \cos\psi & \sin\psi & 0 \\ -\sin\psi & \cos\psi & 0 \\ 0 & 0 & 1 \end{bmatrix} \begin{bmatrix} \mathbf{a}_1'' \\ \mathbf{a}_2'' \\ \mathbf{a}_3'' \end{bmatrix} = \mathbf{C}_3^{B/A''}(\psi) \begin{bmatrix} \mathbf{a}_1'' \\ \mathbf{a}_2'' \\ \mathbf{a}_3'' \end{bmatrix}
\end{aligned} \tag{3.2.3}
$$

By combining the formulae for the successive rotations of these Euler angles one can obtain a single direction cosine matrix which can be used to convert Euler 2-1-3 angles to the DCM, equation 3.2.4.

$$\mathbf{C}^{B/A} = \mathbf{C}_3(\psi)\mathbf{C}_1(\phi)\mathbf{C}_2(\theta)$$

$$= \begin{bmatrix} c\psi & s\psi & 0 \\ -s\psi & c\psi & 0 \\ 0 & 0 & 1 \end{bmatrix} \begin{bmatrix} 1 & 0 & 0 \\ 0 & c\phi & s\phi \\ 0 & -s\phi & c\phi \end{bmatrix} \begin{bmatrix} c\theta & 0 & -s\theta \\ 0 & 1 & 0 \\ s\theta & 0 & c\theta \end{bmatrix}$$

$$= \begin{bmatrix} c\psi & s\psi c\phi & s\psi s\phi \\ -s\psi & c\psi c\phi & c\psi s\phi \\ 0 & -s\phi & c\phi \end{bmatrix} \begin{bmatrix} c\theta & 0 & -s\theta \\ 0 & 1 & 0 \\ s\theta & 0 & c\theta \end{bmatrix}$$

$$= \begin{bmatrix} c\psi c\theta + s\psi s\phi s\theta & s\psi c\phi & -c\psi s\theta + s\psi s\phi c\theta \\ -s\psi c\theta + c\psi s\phi s\theta & c\psi c\phi & s\psi s\theta + c\psi s\phi c\theta \\ c\phi s\theta & -s\phi & c\phi c\theta \end{bmatrix} \qquad (3.2.4)$$

where c and s are the $\cos$ and $\sin$ functions of the indicated angles, respectively. By investigating the DCM representation, the Euler 2-1-3 angles can also be obtained, equation 3.2.5.

$$\theta = \arctan 2\left(C_{31}, C_{33}\right)$$
$$\phi = -\arcsin\left(C_{32}\right)$$
$$\psi = \arctan 2\left(C_{12}, C_{22}\right) \qquad (3.2.5)$$

with $\arctan 2$ defined as the four-quadrant inverse tangent function. Euler angles have no redundant parameters while providing a clear physical interpretation, therefore making it useful for the human interpretation of attitudes, [23].

However, the use of trigonemetric functions increases calculation time and the complexity of the program. This representation is also inconvenient for numerical integration and singularities exist at certain angles, such as $\phi = \pi/2$ radians. In view of this, it becomes apparent that a third attitude represenation method is necessary.

The last method to be discussed here, although others exist[6], employs Euler symmetric parameters, also known as quaternions, for attitude representation. The orientation of reference frame B relative to reference frame A can be represented by a unit vector $\mathbf{e}$ along the Euler axis[7] and a rotation angle Θ about this axis such that

$$\mathbf{e} = e_1\mathbf{a}_1 + e_2\mathbf{a}_2 + e_3\mathbf{a}_3$$
$$= e_1\mathbf{b}_1 + e_2\mathbf{b}_2 + e_3\mathbf{b}_3 \qquad (3.2.6)$$

Using this information with equation 3.2.6, the four quaternions can be defined as

$$q_1 = e_1 \sin\left(\Theta/2\right)$$
$$q_2 = e_2 \sin\left(\Theta/2\right)$$
$$q_3 = e_3 \sin\left(\Theta/2\right)$$
$$q_4 = \cos\left(\Theta/2\right) \qquad (3.2.7)$$

---

[6]The Gibbs vector and Cayley-Klein parameters can also be used for rotation representation.

[7]The Euler axis, or eigenaxis, is the axis of rotation whose orientation relative to both reference frames remains unchanged throughout the motion.

Upon inspection, it is found that the quaternions are not independent but are constrained by

$$q_1^2 + q_2^2 + q_3^2 + q_4^2 = 1 \tag{3.2.8}$$

This property can be used to formulate the direction cosine matrix in terms of the quaternion parameters, as illustrated in equation 3.2.9, which can then be used to obtain the respective Euler angles, as discussed previously.

$$\mathbf{C}^{B/A} = \begin{bmatrix} q_1^2 - q_2^2 - q_3^2 + q_4^2 & 2\left(q_1 q_2 + q_3 q_4\right) & 2\left(q_1 q_3 - q_2 q_4\right) \\ 2\left(q_1 q_2 - q_3 q_4\right) & -q_1^2 + q_2^2 - q_3^2 + q_4^2 & 2\left(q_2 q_3 + q_1 q_4\right) \\ 2\left(q_1 q_3 + q_2 q_4\right) & 2\left(q_2 q_3 - q_1 q_4\right) & -q_1^2 - q_2^2 + q_3^2 + q_4^2 \end{bmatrix} \tag{3.2.9}$$

From the DCM, equation 3.2.9, it is also possible to formulate the transformation of a direction cosine matrix representation to a quaternion attitude representation, equation 3.2.10.

$$q_4 = \frac{1}{2}\sqrt{C_{11} + C_{22} + C_{33} + 1}$$
$$q_1 = \frac{1}{4q_4}\left(C_{23} - C_{32}\right)$$
$$q_2 = \frac{1}{4q_4}\left(C_{31} - C_{13}\right)$$
$$q_3 = \frac{1}{4q_4}\left(C_{12} - C_{21}\right) \tag{3.2.10}$$

It is important to note that $q_4 \neq 0$ for the quaternion calculation illustrated in equation 3.2.10. If the scenario occurs in which $q_4 = 0$, the equation should be reformulated in terms of another quaternion, often q_3, in order to calculate the rest of the quaternion parameters.

The quaternion representation does not have any singularities and avoids the usage of trigonometric functions. It is also suitable for numerical integration and successive rotations.

Because of the lack of a clear physical interpretation, quaternions are primarily used for attitude propagation and control laws after which it can be converted to Euler angles, via a DCM, for easier attitude visualisation.

The requirement and usage of these different attitude representations are, as in the case for coordinate systems, validated by their respective advantages and implementation areas.

3.3 The Mathematics of Satellite Motion

With the representations available to present a satellite's attitude, it is possible to formulate the propagation of a satellite, as discussed below. The first group of formulae, categorised as kinematic equations, can be used to determine the next attitude vector using the current attitude and angular rates. The calculation of the angular rates, however, are influenced by various disturbance torques.

The second group of formulae, called the dynamic equations of motion, define the applicability and interaction that the disturbance torques have on the satellite. Only by implementing both of these categories, is it possible to calculate the resultant motion of a specific satellite.

3.3.1 Kinematics - Motion Without Force

A study of the satellite motion, irrespective of the forces that cause the motion, can be achieved through the kinematic equations for a satellite. Various representations of the kinematics are desired depending on the interpretation to be employed. To describe this motion, it is necessary to define the angular velocity vector, $\boldsymbol{\omega}$, of the satellite for the reference frame that is used.

The Euler 2-1-3 representation of the angular velocity vector for reference frame B relative to reference frame A, defined in section 3.2.2, is illustrated in equation 3.3.1.

$$
\begin{aligned}
\boldsymbol{\omega} = \boldsymbol{\omega}^{B/A} &= \boldsymbol{\omega}^{B/A''} + \boldsymbol{\omega}^{A''/A'} + \boldsymbol{\omega}^{A'/A} \\
&= \dot{\psi}\mathbf{b}_3 + \dot{\phi}\mathbf{a}_1'' + \dot{\theta}\mathbf{a}_2' \\
&= \begin{bmatrix} 0 \\ 0 \\ \dot{\psi} \end{bmatrix} + \mathbf{C}_3(\psi) \begin{bmatrix} \dot{\phi} \\ 0 \\ 0 \end{bmatrix} + \mathbf{C}_3(\psi)\mathbf{C}_1(\phi) \begin{bmatrix} 0 \\ \dot{\theta} \\ 0 \end{bmatrix}
\end{aligned}
$$

$$
\begin{bmatrix} \omega_1 \\ \omega_2 \\ \omega_3 \end{bmatrix} = \begin{bmatrix} \cos\psi & \sin\psi\cos\phi & 0 \\ -\sin\psi & \cos\psi\cos\phi & 0 \\ 0 & -\sin\phi & 1 \end{bmatrix} \begin{bmatrix} \dot{\phi} \\ \dot{\theta} \\ \dot{\psi} \end{bmatrix} \tag{3.3.1}
$$

where $\mathbf{C}_3(\psi)$ and $\mathbf{C}_1(\phi)$ are as illustrated in equation 3.2.3. By rewriting equation 3.3.1, the kinematic equation of motion in Euler 2-1-3 representation, illustrated in equation 3.3.2, can be achieved.

$$
\begin{bmatrix} \dot{\phi} \\ \dot{\theta} \\ \dot{\psi} \end{bmatrix} = \frac{1}{\cos\phi} \begin{bmatrix} \cos\psi\cos\phi & -\sin\psi\cos\phi & 0 \\ \sin\psi & \cos\psi & 0 \\ \sin\psi\sin\phi & \sin\phi\cos\psi & \cos\phi \end{bmatrix} \begin{bmatrix} \omega_1 \\ \omega_2 \\ \omega_3 \end{bmatrix} \tag{3.3.2}
$$

With the attitude representations discussed in section 3.2.2, the kinematic equation of motion and direct conversion from Euler rates to body rates, can be rewritten for the DCM representation, equations 3.3.3 and 3.3.4, respectively.

$$\dot{\mathbf{C}}^{B/A} = -\mathbf{\Omega}\mathbf{C}^{B/A} = - \begin{bmatrix} 0 & -\omega_3 & \omega_2 \\ \omega_3 & 0 & -\omega_1 \\ -\omega_2 & \omega_1 & 0 \end{bmatrix} \mathbf{C}^{B/A} \tag{3.3.3}$$

$$\omega_1 = \dot{C}_{21}C_{31} + \dot{C}_{22}C_{32} + \dot{C}_{23}C_{33}$$
$$\omega_2 = \dot{C}_{31}C_{11} + \dot{C}_{32}C_{12} + \dot{C}_{33}C_{13}$$
$$\omega_3 = \dot{C}_{11}C_{21} + \dot{C}_{12}C_{22} + \dot{C}_{13}C_{23} \tag{3.3.4}$$

The quaternion representation of the kinematics, equation 3.3.5, and the conversion between body and quaternion rates, equation 3.3.6, can be obtained similar to the DCM conversion process.

$$\begin{bmatrix} \dot{q}_1 \\ \dot{q}_2 \\ \dot{q}_3 \\ \dot{q}_4 \end{bmatrix} = \frac{1}{2} \begin{bmatrix} 0 & \omega_3 & -\omega_2 & \omega_1 \\ -\omega_3 & 0 & \omega_1 & \omega_2 \\ \omega_2 & -\omega_1 & 0 & \omega_3 \\ -\omega_1 & -\omega_2 & -\omega_3 & 0 \end{bmatrix} \begin{bmatrix} q_1 \\ q_2 \\ q_3 \\ q_4 \end{bmatrix} \tag{3.3.5}$$

$$\begin{bmatrix} \omega_1 \\ \omega_2 \\ \omega_3 \end{bmatrix} = 2 \begin{bmatrix} q_4 & q_3 & -q_2 & -q_1 \\ -q_3 & q_4 & q_1 & -q_2 \\ q_2 & -q_1 & q_4 & -q_3 \end{bmatrix} \begin{bmatrix} \dot{q}_1 \\ \dot{q}_2 \\ \dot{q}_3 \\ \dot{q}_4 \end{bmatrix} \tag{3.3.6}$$

It is useful to reduce the processing and memory requirements by implementing the direct conversion equations to determine the body rates from the currently known data. Quaternions are primarily used for the calculation of the changes to the satellite kinematics, equations 3.3.7 and 3.3.8, whereafter the DCM, discussed in section 3.2.2, would be used to convert the results to Euler 2-1-3 angles for interpretation purposes.

$$\dot{\mathbf{q}} = \frac{1}{2}\mathbf{\Omega}\mathbf{q}$$

$$\begin{bmatrix} \dot{q}_1 \\ \dot{q}_2 \\ \dot{q}_3 \\ \dot{q}_4 \end{bmatrix} = \frac{1}{2} \begin{bmatrix} 0 & \omega_3 & -\omega_2 & \omega_1 \\ -\omega_3 & 0 & \omega_1 & \omega_2 \\ \omega_2 & -\omega_1 & 0 & \omega_3 \\ -\omega_1 & -\omega_2 & -\omega_3 & 0 \end{bmatrix} \begin{bmatrix} q_1 \\ q_2 \\ q_3 \\ q_4 \end{bmatrix} \tag{3.3.7}$$

$$\dot{\mathbf{q}}(k) = \frac{\mathbf{q}(k+1) - \mathbf{q}(k)}{T_s}\mathbf{\Omega} = \frac{1}{2}\mathbf{\Omega}\mathbf{q}$$
$$\mathbf{q}(k+1) = \left(\frac{T_s}{2}\mathbf{\Omega} + \mathbf{I}\right)\mathbf{q}(k) \tag{3.3.8}$$

where T_s is the sampling time; $\mathbf{q}(k)$ and $\mathbf{q}(k+1)$ are the attitudes at time k and $k+1$ respectively; and $\mathbf{I}$ is a 4×4 identity matrix. This process describes the attitude of the satellite as it propogates, irrespective of the forces that are applied to the satellite.

3.3.2 The Dynamic Motion of a Satellite

The attitude dynamics of a satellite can be represented by the Euler dynamic equation of motion, equation 3.3.9.

$$\mathbf{J}\dot{\boldsymbol{\omega}}^{B/I} = \mathbf{N} - \boldsymbol{\omega}^{B/I} \times \left(\mathbf{J}\boldsymbol{\omega}^{B/I} + \mathbf{h}\right) - \dot{\mathbf{h}} \tag{3.3.9}$$

where $\mathbf{J}$ is the moment of inertia matrix of the satellite; $\dot{\boldsymbol{\omega}}^{B/I}$ is the angular acceleration and $\boldsymbol{\omega}^{B/I}$ is the angular rate vector in the body-fixed reference frame with respect to the inertial reference frame; $\mathbf{N}$ is the total torque that is applied to the satellite body; $\mathbf{h}$ is the angular momentum of the reaction wheels and $\dot{\mathbf{h}}$ is the rate of change of the reaction wheels.

The inertia of an object is simply the resistance which an object has to a change in its state of motion, similarly the moment of inertia of an object defines the resistance that an object has against changes to its rotation. The moment of inertia matrix, $\mathbf{J}$, thus relates the angular velocity vector to the angular momentum vector. A prinicipal axis exist, in which the products of inertia[8] are all zero and the resulting moment of inertia matrix becomes

$$\mathbf{J} = \begin{bmatrix} J_{11} & 0 & 0 \\ 0 & J_{22} & 0 \\ 0 & 0 & J_{33} \end{bmatrix} \tag{3.3.10}$$

When regarding the principal axes, the Euler dynamic equations, equation 3.3.9, can be reduced to

$$J_{11}\dot{\omega}_1^{B/I} = N_1 - \omega_2^{B/I}\left(J_{33}\omega_3^{B/I} + h_3\right) + \omega_3^{B/I}\left(J_{22}\omega_2^{B/I} + h_2\right) - \dot{h}_1$$

$$J_{22}\dot{\omega}_2^{B/I} = N_2 + \omega_1^{B/I}\left(J_{33}\omega_3^{B/I} + h_3\right) - \omega_3^{B/I}\left(J_{11}\omega_1^{B/I} + h_1\right) - \dot{h}_2$$

$$J_{33}\dot{\omega}_3^{B/I} = N_3 - \omega_1^{B/I}\left(J_{22}\omega_2^{B/I} + h_2\right) + \omega_2^{B/I}\left(J_{11}\omega_1^{B/I} + h_1\right) - \dot{h}_3 \tag{3.3.11}$$

As have been discussed in section 2.3, the derivative of the angular momentum of a body equals the torque that is applied to that body, thus the derivative of the reaction wheels' angular momentum can be written as

$$\frac{\mathrm{d}\mathbf{h}}{\mathrm{d}t} = \dot{\mathbf{h}} = \mathbf{N}_{wheel} \tag{3.3.12}$$

It is possible, using these dynamic equations of motion, to propogate the angular rates of the satellite body. However, in order to propogate the attitude of the satellite, the angular rates of the satellite body relative to the orbit reference frame, $\boldsymbol{\omega}^{B/O}$, are required.

---

[8]The products of inertia is the term used for all the non-diagonal elements of the moment of inertia matrix.

From section 3.2.1, it is apparent that the orbit reference frame rotates, relative to the inertial reference frame, about the negative Y-axis with an instantaneous angular velocity

$$\tilde{\omega}(t) \approx \omega_0 \left(1 + 2e \cos \nu\right)$$

where ω_0 is the orbit mean motion; e is the orbit eccentricity; and ν is the true anomaly. The angular velocity of the orbit frame relative to the inertial frame can be expressed in the basis vectors of the body frame, using the DCM of the body frame relative to the orbit frame, as

$$\boldsymbol{\omega}^{O/I} = -C_{12}\tilde{\omega}(t)\mathbf{b}_1 - C_{22}\tilde{\omega}(t)\mathbf{b}_2 - C_{32}\tilde{\omega}(t)\mathbf{b}_3$$

It can thus be found that the angular velocity of the body-fixed frame relative to the inertial frame is equal to the sum of the angular velocities of the body-fixed frame relative to the orbit frame and that of the orbit frame relative to the inertial frame, equation 3.3.13.

$$\boldsymbol{\omega}^{B/I} = \boldsymbol{\omega}^{B/O} + \boldsymbol{\omega}^{O/I}$$

$$\begin{bmatrix} \omega_1^{B/I} \\ \omega_2^{B/I} \\ \omega_3^{B/I} \end{bmatrix} = \begin{bmatrix} \omega_1^{B/O} \\ \omega_2^{B/O} \\ \omega_3^{B/O} \end{bmatrix} - \begin{bmatrix} C_{12}\tilde{\omega}_o \\ C_{22}\tilde{\omega}_o \\ C_{32}\tilde{\omega}_o \end{bmatrix} \tag{3.3.13}$$

The total torque, $\mathbf{N}$, that affects the satellite can be attributed to a combination of various of the following torques.

Gravity gradient disturbance torque. The variations in the Earth's gravitational force generates a disturbance torque, $\mathbf{N}_{GG}$, which tends to keep the long axis of a satellite nadir pointing. This disturbance torque can be calculated with

$$\mathbf{N}_{GG} = \frac{3GM}{R^3} \left(J_{33} - \frac{J_{11} + J_{22}}{2} \right) (\mathbf{a}_3 \cdot \mathbf{b}_3)(\mathbf{a}_3 \times \mathbf{b}_3) \tag{3.3.14}$$

Aerodynamic disturbance torque. The atmospheric drag which LEO satellites experience decreases the satellite's energy and altitude, which in turn increases its velocity. The resultant torque, $\mathbf{N}_{AERO}$, can be calculated using

$$\mathbf{N}_{AERO} = \rho_a V^2 A_p (\mathbf{c}_a \times \mathbf{V}_{unit}) \tag{3.3.15}$$

Magnetic disturbance torque. The magnetic torque, $\mathbf{N}_M$, can be generated from the interaction of the dipole moment, $\mathbf{M}$, of the magnetic torquer rods and the Earth's geomagnetic field, $\mathbf{B}$, illustrated in equation 3.3.16.

$$\mathbf{N}_M = \mathbf{M} \times \mathbf{B} \tag{3.3.16}$$

Solar radiation pressure torque. As mentioned in section 2.2, the solar radiation pressure torque, $\mathbf{N}_{solar}$, that can be generated with a solar sail is calculated with

$$\mathbf{N}_{solar} = \mathbf{C}_p \times \mathbf{F}_s \tag{3.3.17}$$

By calculating the disturbance and control torques which are applied to the satellite, it is possible to determine, as well as control, the propagation of the attitude vectors of the orbiting satellite.

3.4 Attitude Determination and Control

The attitude determination and control subsystem is one of the most important parts of a satellite. It is required to provide positional information as well as facilitating in-orbit manoeuvres such as stationkeeping, alignment and pointing of satellite components.

Various sensors can be implemented on the satellite for scientific purposes. These sensors also provide orbital position information based on their measurements which can be used to estimate the attitude of the satellite. This process is known as attitude determination.

Attitude control can be achieved through the use of actuators. Depending on the desired "final" attitude and the current estimated attitude, a control command can be used to employ the available actuators to realise this change in attitude.

3.4.1 Determining Satellite Attitude

Due to the dynamic motion of an orbiting satellite, it is difficult to obtain the exact attitude of the satellite. However, the necessary accuracy of the attitude estimate can be obtained depending on the sensors, and estimation techniques, used. Based on the satellite's requirements, the design is adjusted to utilise various of the following sensors, [24], [40] and [41].

Gyroscopes.

> A gyroscope implements a rapidly spinning mass to measure the speed or angle of rotation in the satellite's inertial orientation. Since gyroscopes do not have any knowledge of an external, absolute reference, they must be used in conjunction with external references to provide precision attitude sensing, with bias drift accuracies ranging between 0.1 and 0.001 °/hr.

Horizon Sensor.

> Horizon sensors exploit the infrared wavelengths to detect the contrast between the heat of the Earth's atmosphere and the cold of deep space. The detected horizon is used to directly determine the satellite's orientation with respect to the Earth with accuracies ranging from 0.03° to 0.1°.

Magnetometer.

> Magnetometers measure the direction and size of the Earth's magnetic field which can be compared to the known magnetic field information allowing attitude estimation. Due to the changing nature of the Earth's magnetic field and the uncertainties of the field strength, the accuracy, between 0.5° and 3°, of this method is very low when compared to other methods.

Star Sensors.

Star sensors are used to measure the coordinates of stars, with respect to the satellite, which can then be compared to star directions obtained from a star catalogue thereby providing attitude information. Although star sensors are heavier and more expensive than other sensors, they provide the best accuracy, between 1 arcsec and 1 arcmin.

Sun Sensors.

Sun sensors detect visible-light and are used to determine one or two angles between their mounting base and the incident sunlight. They have a good accuracy, between $0.005°$ and $3°$, but require an unobstructed field of view.

GPS Receivers.

GPS receivers use the differential signals from different antennae on a satellite to determine the satellite's attitude and are theoretically capable of a $0.1°$ accuracy.

To increase the overall accuracy of the attitude measurements, combinations of these sensors can be used. However, regardless of the sensors employed, estimation techniques are required to maximise attitude determination accuracy and provide continuous attitude information.

The implemented estimation technique acts as a dynamic model for the prediction of the satellite's attitude in the event that no sensor measurements are available. These techniques include, but are not limited to, the following.

A Kalman filter is most often used to determine the satellite body angular rates from sensor measurements and a known model, such as magnetometer readings and the International Geomagnetic Reference Field (IGRF) model. But when it is necessary to estimate all the states, an extended Kalman filter must be used due to the non-linear dynamic and kinematic models, [42].

Another alternative is the TRIAD algorithm which uses star vector pairs, consisting of observed and reference triads, to predict only the satellite's attitude, [23]. A star sensor is implemented to track numerous stars with this algorithm. Optimal variations of the TRIAD algorithm, such as the QUEST algorithm [43] and recursive DCM estimation methods [44], have also been implemented.

3.4.2 Controlling the Attitude of a Satellite

The ability to control a satellite's attitude depends upon the available actuators and the control algorithms that implement these actuators. A variety of actuators have already been discussed in section 2.3. As mentioned before, these actuators apply forces to the

satellite which result in torques about the satellite axes.

To achieve the required attitude control capabilities, combinations of these actuators can be implemented. However, utilising these torques in order to achieve a desired attitude change necessitates the usage of suitable control algorithms.

The control algorithms can be divided into two main categories: active control and passive control algorithms. Passive attitude control techniques, such as gravity gradient torques, permanent magnets and spin-stabilisation, exploit the available natural torques to maintain a required attitude. The advantage is that the effect of passive controls are experienced throughout the satellite's orbit without requiring any control input from the satellite.

Because passive control methods do not require any control input, it also means that these passive control torques cannot be managed. Thus, for precise pointing applications and three-axis attitude control, active control techniques are required that can be continually adjusted throughout the satellite's orbit.

Active attitude control incorporates the entire ADCS process, as listed below, to realise the necessary changes to the satellite's attitude, [40].

- Sensor measurements of the satellite's attitude with respect to external references.

- The determination of the current attitude using the sensor measurements.

- The computation of the necessary control commands for a desired attitude.

- Execution of the control commands.

- Propagation of the satellite's attitude.

This process, illustrated in figure 3.8, is continuously repeated at a specified sampling rate in order to determine and control the attitude of the satellite, [23].
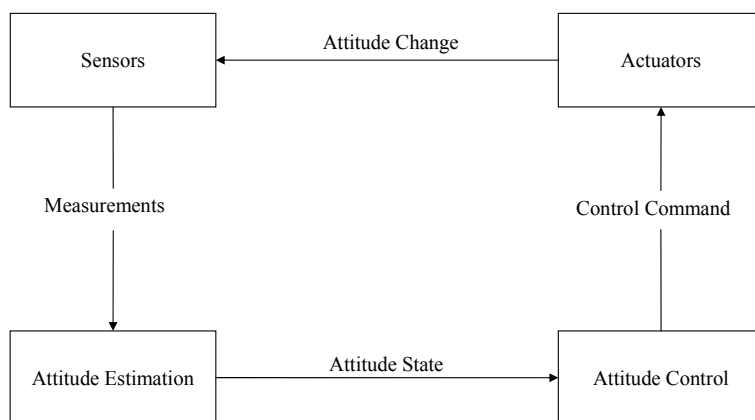
Figure 3.8 – ADCS Process

The control algorithms that can be implemented are often limited by the satellite's processing capabilities as well as the applicable actuators. Some examples of satellite control systems include fuzzy logic; switch-mode; and proportional-integral-derivative controllers.

Fuzzy logic represents a mathematical process for defining the degrees of truth using linguistic variables. A set of rules consisting of *If-Then* statements describes a fuzzy control system. A fuzzy logic controller design and implementation for magnetic torquer rods is illustrated in [42].

Switch-mode controllers, also known as bang-bang controllers, are attractive because of their relatively simple implementation and the minimum control time utilisation for this type of algorithm. Though, a smooth change in attitude is not possible when the change in attitude occurs in such a minimum time period.

Linear quadratic controllers, [8], as well as linear state feedback controllers, [45], have also been successfully implemented in the past. However, the most widely used satellite attitude control systems are proportional-integral-derivative (PID) controllers, with variations such as the *cross product* and *B-dot* control laws, [46].

The PID controllers can be tuned for the specific actuator and process requirements, while the feedback term would consist of the attitude error that must be minimised. A quaternion error feedback term is most aptly suited, as discussed in section 3.2.2, although other attitude representations can also be implemented. Such a quaternion feedback PD controller is illustrated in [47].

As in most scenarios the resultant control, rather than the type of control algorithm, is important. Stability is paramount for satellites even though fast control is not necessarily required. There may, however, be a specified period of time in which an attitude change has to be realised. Taking this into consideration, it is apparent that the eventual control system implementation depends not only on the actuators, but also on the required attitude changes and the satellite's capabilities.

3.5   CubeSat Simulation Details

The properties of a satellite, such as the orbital elements; attitude representations; and equations of motion, have to be taken into account for the simulation models and setup.

To demonstrate the attitude control capabilities of a solar sail CubeSat, it was proposed to simulate a 3-Unit CubeSat in an approximate 800 km, circular, sun-synchronous low Earth orbit, [48]. The initial orbital elements, discussed in section 3.1.1, that were used for the simulation are listed in table 3.1, [48].

Table 3.1 – Initial Orbital Elements

Semi-major axis a	7169.65	km
Inclination i	98.24	°
Orbital Period T	6041.7	s
Eccentricity e	0.001	

The orbit orientation of the proposed satellite is illustrated in figure 3.9, reproduced from [48].
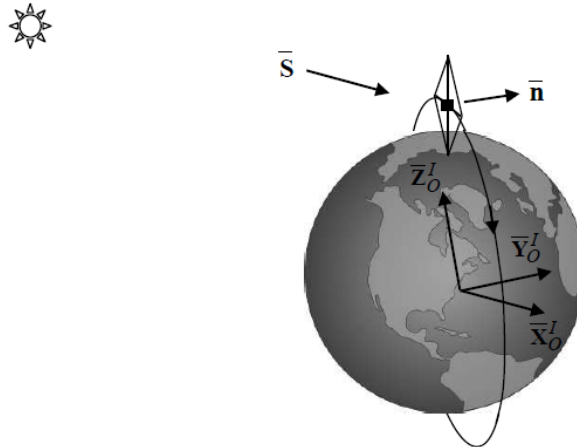
Figure 3.9 – Satellite Orientation

Since the attitude measurements are often defined in the SBC reference frame while the comparative model is in the ORC frame, it is necessary to convert between the reference frames. The attitude reference frames discussed in section 3.2.1 are used for the attitude determination models. The use of quaternions were proposed for attitude propagation calculations, thereby avoiding the possibility of singularities.

In each of these cases, the direction cosine matrix is used to convert between the different reference frames and attitude representations. For the visual attitude representation, an Euler 213 rotation sequence was chosen, figure 3.7. This allows unlimited rotations in the pitch and yaw axes while limiting[9] the rotations in the roll axis to a maximum of $\pm\,90°$.

3.5.1 Torques Applied to the CubeSat

It is possible to reduce the complexity of the mathematical models by using intelligent approximations and assumptions. These simplifications can greatly decrease the processing time required for attitude propagation. As already mentioned in section 3.1.1, a circular orbit is assumed which results in the satellite having a constant[10] orbital velocity.

---

[9]Singularities in the Euler representation are thus limited to the roll axis.
[10]When ignoring the effects of disturbance torques.

Furthermore, because the products of inertia of the CubeSat are in the order of two magnitudes less than the moments of inertia, these products can be ignored resulting in the moment of inertia matrix illustrated in equation 3.5.1.

$$\boldsymbol{I}_0 = diag \begin{bmatrix} I_{xx0} & I_{yy0} & I_{zz0} \end{bmatrix} = diag \begin{bmatrix} 0.022 & 0.027 & 0.022 \end{bmatrix} \text{kg.m}^2$$
$$\boldsymbol{I} = diag \begin{bmatrix} I_{xx} & I_{yy} & I_{zz} \end{bmatrix} = diag \begin{bmatrix} 0.703 & 1.376 & 0.703 \end{bmatrix} \text{kg.m}^2 \qquad (3.5.1)$$

where $\boldsymbol{I}_0$ indicates the moments of inertia before the deployment of the solar sail and $\boldsymbol{I}$ refers to the moments of inertia after sail deployment. Equation 3.5.2 illustrates the centre of pressure (CoP) to centre of mass (CoM) vector, $\boldsymbol{r}_{m/p}$, of the sail attachment, which is used in the orbital propagation of the satellite.

$$\boldsymbol{r}_{m/p} = \begin{bmatrix} r_{cntr\_x} & -7.5 & r_{cntr\_z} \end{bmatrix}^T \text{cm} \qquad (3.5.2)$$

where r_{cntr_x} and r_{cntr_z} are the control outputs for the translation stage.

It was proposed to implement a Simplified General Perturbations No. 4 (SGP4) orbit model; an accurate sun orbit model; and a 10th order International Geomagnetic Reference Field (IGRF) model for the geomagnetic field vector.

The attitude dynamics of the CubeSat can be derived with equation 3.3.9, which is repeated here for the sake of convenience

$$\mathbf{J}\dot{\boldsymbol{\omega}}^{B/I} = \mathbf{N} - \boldsymbol{\omega}^{B/I} \times \left(\mathbf{J}\boldsymbol{\omega}^{B/I} + \mathbf{h} \right) - \dot{\mathbf{h}}$$

The simplification of this dynamic equation has been shown in section 3.3.2, however the mathematical models of the torques, [48], that were proposed for the CubeSat are discussed in detail below.

The aerodynamic drag force depends upon the satellite orbital velocity and the Earth's rotation. The resultant atmospheric drag velocity vector, in satellite body coordinates, is

$$\boldsymbol{v}_A^B = \left(\|\boldsymbol{v}_o\| - \left(\omega_E \|\boldsymbol{R}\| \cos\left(i\right) \right) \right) \boldsymbol{C}^{B/O} \begin{bmatrix} -1 & \left(\omega_E \|\boldsymbol{R}\| / \|\boldsymbol{v}_o\| \right) \sin\left(i\right) \cos\left(\lambda\right) & 0 \end{bmatrix}^T$$

where $\boldsymbol{C}^{B/O}$ is the DCM used to convert between the body and orbit coordinate systems. The atmospheric density can be calculated with

$$\rho = \rho_o e^{-(h-h_o)/H}$$

where h is the orbital altitude in the range of 700 to 800 km; h_o = 700 km; the atmospheric density during the sun-lit part of the orbit[11] $\rho_o = 3.614 \times 10^{-14}$ kg/m³; and the scale height H = 88.667 km. The aerodynamic disturbance torque which will be implemented in the simulation can then be calculated as

$$\boldsymbol{N}_{Aero} = \rho \left\| \boldsymbol{v}_A^B \right\|^2 A_p \left[\sigma_t \left(\boldsymbol{r}_{m/p} \times \bar{\boldsymbol{v}}_A^B \right) + \left(\sigma_n \left(v_b / \left\| \boldsymbol{v}_A^B \right\| \right) + \left(2 - \sigma_n - \sigma_t \right) \cos\left(\alpha\right) \right) \left(\boldsymbol{r}_{m/p} \times \bar{\boldsymbol{n}}_{sail} \right) \right]$$

---

[11] Mean solar conditions are assumed over a period of 1 year with 50% of ρ_o applicable during eclipse.

which is further reduced to equation 3.5.3[12].

$$\boldsymbol{N}_{Aero} = \rho \left\| \boldsymbol{v}_A^B \right\|^2 A_p \left[0.8 \left(\boldsymbol{r}_{m/p} \times \bar{\boldsymbol{v}}_A^B \right) + (0.04 + 0.4 \cos{(\alpha)}) \left(\boldsymbol{r}_{m/p} \times \bar{\boldsymbol{n}}_{sail} \right) \right] \qquad (3.5.3)$$

with α being the incidence angle of the atmospheric velocity normal to the solar sail. The Heaviside function, $H\{x\}$ in $A_p = H\{\cos(\alpha)\} \cos(\alpha) A_{sail}$, ensures that the correct instance of this equation is used, since the sign of $\cos{(\alpha)}$ determines whether the velocity vector impacts on the front or rear of the solar sail.

The solar pressure torque model can be described with the normal, $\boldsymbol{F}_n$, and tangential, $\boldsymbol{F}_t$, forces, illustrated in equation 3.5.5, of the solar radiation pressure force[13].

$$\begin{aligned} \boldsymbol{F}_n &\approx 1.83 P A_{sail} \cos^2{(\beta)} \, \bar{\boldsymbol{n}}_{sail} \\ \boldsymbol{F}_t &\approx 0.17 P A_{sail} \cos{(\beta)} \sin{(\beta)} \left(\perp \bar{\boldsymbol{n}}_{sail} \right) \end{aligned} \qquad (3.5.4)$$

where $P = 4.563 \times 10^{-6}$ N/m²; β is the incidence angle of the sun normal to the solar sail; and the exposed area of the sail $A_{sail} = 25$ m². The cos, sin and the perpendicular component of the sail normal vector, $\bar{\boldsymbol{n}}_{sail}$, can be calculated with

$$\begin{aligned} \cos{(\beta)} &= \bar{\boldsymbol{s}}_B \cdot \bar{\boldsymbol{n}}_{sail} = |s_{yb}| \\ \sin{(\beta)} &= \sqrt{1 - s_{yb}^2} \\ \perp \bar{\boldsymbol{n}}_{sail} &= \left[\begin{array}{ccc} s_{xb}/\sqrt{s_{xb}^2 + s_{zb}^2} & 0 & s_{zb}/\sqrt{s_{xb}^2 + s_{zb}^2} \end{array} \right]^T \end{aligned}$$

where

$$\bar{\boldsymbol{s}}_B = \boldsymbol{C}^{B/O} \boldsymbol{C}^{O/I} \bar{\boldsymbol{s}}_I = \left[\begin{array}{ccc} s_{xb} & s_{yb} & s_{zb} \end{array} \right]^T$$

with $\boldsymbol{C}^{B/O}$ and $\boldsymbol{C}^{O/I}$ being the DCMs used to convert between body and orbit; and between orbit and inertial coordinate systems.

The sign of the normal component of the total force vector is dependent upon the side of the solar sail which is at that moment exposed to the sun. That is, if the solar pressure impinges upon the sail front then $\bar{\boldsymbol{n}}_{sail} = \left[\begin{array}{ccc} 0 & -1 & 0 \end{array} \right]^T$ whereas if the solar pressure impinges upon the sail rear then $\bar{\boldsymbol{n}}_{sail} = \left[\begin{array}{ccc} 0 & 1 & 0 \end{array} \right]^T$. The resultant total force vector is illustrated in equation 3.5.5, where the sign of $\boldsymbol{F}_{Solar}(2)$ is negative for the case in which the solar pressure impacts the front of the sail, otherwise the positive instance is used.

$$\boldsymbol{F}_{Solar} = \left[\begin{array}{c} F_{tx} \\ F_n \\ F_{tz} \end{array} \right] = \left[\begin{array}{c} \| \boldsymbol{F}_t \| \, s_{xb}/\sqrt{s_{xb}^2 + s_{zb}^2} \\ \mp \| \boldsymbol{F}_n \| \\ \| \boldsymbol{F}_t \| \, s_{zb}/\sqrt{s_{xb}^2 + s_{zb}^2} \end{array} \right] \qquad (3.5.5)$$

The effective solar disturbance torque can therefore be calculated with

$$\boldsymbol{N}_{solar} = \boldsymbol{r}_{m/p} \times \boldsymbol{F}_{solar} \qquad (3.5.6)$$

---

[12] For more details regarding this simplification process, refer to [48].
[13] Refer to [25] and [26] regarding the optical properties of a sail, assuming negligible billowing effects.

The formulae for the gravity gradient, magnetic, and reaction wheel torques have been discussed in section 3.3.2 remain unchanged and will not be repeated here.

These torque formulae are implemented in the satellite's attitude determination and control subsystem to calculate the satellite position along its orbit. Although implemented, the determination part of the ADCS for the proposed CubeSat is not a part of this thesis, and is therefore only briefly summarised here.

Miniature complimentary metal oxide semiconductor (CMOS) cameras were proposed for use as Sun and nadir sensors. A robust Kalman filter using only the Sun vector information was proposed as the primary determination algorithm to estimate the angular rates. Whereas a TRIAD algorithm using both Sun and nadir sensors was additionally implemented in the simulation to estimate the satellite's attitude.

Measurement noise is applicable to all types of sensors and must be added to the ideal measurement components of the simulation model. A uniform random number generator was used for the generation of noise signals which were then low pass filtered to obtain an uncorellated error for each vector component. The characteristics associated with this noise generation are listed in table 3.2, [48].

Table 3.2 – Simulation Sensor Noise

	LPF Noise Output (1-σ)	Vector Angular Noise (1-σ)	LPF Time Constant (seconds)
Magnetometer	20 nT	0.28°	25
Sun Sensor	0.0005 units	0.42°	100
Nadir Sensor	0.0005 units	0.42°	100

The control outputs for the magnetorquers and solar sail translation actuators are based upon these noisy sensor measurements. As such, to prevent the excessive operation of these actuators, the solar sail control outputs and the magnetic error were both low pass filtered with filtering time constants of 50 s.

The operation of these determination methods, briefly discussed in section 3.4.1, are critical for the effective attitude control of the satellite.

3.5.2 CubeSat Control Algorithms

As previously mentioned, the satellite will rely on magnetic torquer rods that interact with the Earth's geomagnetic field; 2D translation of a solar sail exploiting solar radiation pressure; and the spinning of a y-axis reaction wheel to provide full three-axis attitude control.

The control algorithms that were proposed, are mostly variations of proportional-derivative (PD) controllers that have been successfully implemented in previous work, [48]. The simulation was designed to provide the user with a choice of which combination of controllers to implement for attitude control.

For the magnetic controller, *cross product* [23], *y-spin* [49], and *B-dot* [46] control laws were implemented. The *cross product* control law uses a quaternion feedback error vector,

$$\boldsymbol{e} = K_P \hat{\boldsymbol{\omega}}_o + K_D \hat{\boldsymbol{q}}_{err} \tag{3.5.7}$$

with $\hat{\boldsymbol{\omega}}_o$ the estimated orbit referenced angular rates; and $\hat{\boldsymbol{q}}_{err}$ the estimated quaternion error vector[14]. The K_P and K_D terms are only used as an indication for the proportional and derivative gains, respectively, which have to be tuned[15]. The error vector is then used to calculate the magnetic moment as

$$\boldsymbol{M} = \boldsymbol{e} \times \boldsymbol{B}_{meas} / \left\| \boldsymbol{B}_{meas} \right\|$$

The second type of magnetic torquer control is a combination of the *y-spin* and *B-dot* control laws. This control method is often used as an alternative to the *cross product* control law, since no attitude or rate estimates and no measurements are required. The *B-dot* controller, equation 3.5.8, is used for the detumbling of the satellite while the *y-spin* controller is responsible for the body y-axis spin rate, equation 3.5.9.

$$M_y = K_D \dot{\beta} \tag{3.5.8}$$

$$M_x = K_S \left(\omega_{yi} - \omega_{yref} \right) sgn \left(B_z \right)$$
$$M_z = -K_S \left(\omega_{yi} - \omega_{yref} \right) sgn \left(B_x \right) \tag{3.5.9}$$

where $\beta = \cos^{-1} \left(B_y / \left\| \boldsymbol{B}_{meas} \right\| \right)$ is the angle between the body y-axis and the local magnetic field; ω_{yref} is the reference body y-axis spin rate; and K_D and K_S are the terms used to indicate the detumbling and spin controller gains, respectively. The magnetic moment, implemented for the spin rate controller, depends upon the Earth's magnetic field. Therefore the most effective moment is chosen, with M_x being implemented when $|B_z| > |B_x|$ while M_z is used when $|B_x| > |B_z|$.

The sail controller is also based on a PD attitude controller employing a quaternion error feedback vector. The quaternion error as well as the body rates are used to determine the required change in translation of the sail panel, equation 3.5.10.

$$r_{cntr\_x} = K_D \hat{\omega}_z + K_P \hat{q}_{3e}$$
$$r_{cntr\_z} = K_D \hat{\omega}_x + K_P \hat{q}_{1e} \tag{3.5.10}$$

---

[14]Only $\hat{q}_{1e}$, $\hat{q}_{2e}$, and $\hat{q}_{3e}$ are used in equation 3.5.7.
[15]They do not refer to any fixed value or relationship between other formulae that use these terms.

with r_{cntr} being the translation stage control outputs; and K_D and K_P the proportional and derivative gains[16].

The implementation of the reaction wheel is a special case in which only the reaction wheel is used to control the y-axis attitude. The reaction wheel controller was also based on a quaternion error feedback PD control scheme and must be implemented in conjunction with the *cross product* controller, where the magnetic control law is altered in such a way that the y-axis component is only used for momentum dumping of the reaction wheel. The y-axis component of the quaternion error used for the magnetic controller, equation 3.5.7, thus changes to

$$e_y = K_Y \left(H_{wy} - H_{wy-ref} \right) \tag{3.5.11}$$

with K_Y being the magnetic controller derivative gain which controls the speed of the reaction wheel; H_{wy} the wheel momentum; and H_{wy-ref} the reference wheel momentum. The y-axis torque generated by the reaction wheel can be calculated with equation 3.5.12, [23].

$$N_{wy} = K_P J_{yy} \hat{q}_{2e} + K_D J_{yy} \hat{\omega}_y \tag{3.5.12}$$

where J_{yy} is the inertia of the satellite along the y-axis; and K_P and K_D are the proportional and derivative gains. The implementation of the actuators and controllers of the proposed CubeSat are discussed in chapter 4, while the simulation results can be found in chapter 5.

---

[16]As previously mentioned, these terms are an indication of the gain type and not the values or relationships between equations.

Chapter 4

Design and Implementation

The design and implementation of the mechanical and electronic components are vital for the correct operation of the attitude controllers. This chapter discusses the design of a solar sail translation stage as well as a magnetic torquer rod which are used as actuators on the CubeSat. In addition, the requirements and implementation of the electronic circuits used to operate these actuators are discussed in detail.

In conclusion, the software design and implementation for the hardware, the computer simulations, and the hardware-in-the-loop simulations are described.

4.1   Mechanical System Design

A mechanical design is required to position the solar sail in order to generate a control torque around the body X_B (roll) and Z_B (yaw) axes. In fundamental terms one can state that a structure is needed which can be moved in two orthogonal directions, thereby exploiting the solar pressure induced torque by controlling the centre-of-pressure (CoP) to centre-of-mass (CoM) vector, [48].

In this section, the requirements of the mechanical system are firstly discussed, after which two design approaches are introduced. In conclusion, the design approaches are evaluated and compared to obtain the best solution.

4.1.1   System Requirements and Specifications

An inherent requirement of the structure is for it to be lightweight and stable. This is important because the heavier the satellite becomes, the less effective any positioning control systems become. The structure needs to be stable, not just in outer space, but also in the presence of gravity due to the additional stress which the satellite undergoes during the launch procedure.

The specifications for the structure are listed in table 4.1. The *Volume*, *Mass*[1] and *Range*[2] of the system were identified as the critical goals of the design phase.

Table 4.1 – Mechanical Design Specifications

Width	100	mm
Height	50	mm
Length	100	mm
Volume	500000	mm^3
Mass	200	g
Range	$\pm\,30$	mm

Various options exist to facilitate the movement of a structure within two axes, typically referred to as translation stages. However, these commercially available systems are too large and heavy to be considered for a CubeSat. A custom design and construct was therefore decided on using the concept of a rack and pinion system which can be moved using a stepper motor.

The rack, pinion, and motor choices are globally consistent, that is to say they remain the same regardless of the final translation structure, and must be taken into consideration before designing the mechanical structure.

4.1.1.1 Stepper Motor Specifications

The selection and performance of the stepper motors are discussed in section 4.3.1.3, however the specifications that are necessary for the structural design are listed in table 4.2.

Table 4.2 – Stepper Motor Specifications

Diameter	8	mm
Mass	7.9	g
Length	34.7	mm

To put these dimensions into perspective, a photograph of the actual stepper motor is illustrated in figure 4.1.

---

[1]The mass specification refers to the mechanical structure's mass including its components.

[2]The range pertains to the maximum positive or negative distance that can be moved on the two axes.

Figure 4.1 – Actual Stepper Motor

4.1.1.2 Rack and Pinion Selection

With a rack and pinion system, one can translate the rotational motion of the pinion into a linear movement on the rack. *Delrin* has a low density and coefficient of friction and was therefore chosen as the material to be used for the rack and pinion. In addition it does not require any lubrication and is therefore well suited for use outside the Earth's atmosphere.

The requirements of the rack and pinion system, listed in table 4.3, are defined by taking into consideration the overall diameter as well as shaft diameter of the stepper motor, and also the dimensions of the CubeSat.

Table 4.3 – Rack and Pinion Requirements

	Required		Achieved	
Rack Length	100	mm	100	mm
Pinion Inner Diameter	1.5	mm	1.5	mm
Pinion Outer Diameter	≤ 8	mm	6	mm
Pinion Width	≤ 3.75	mm	3	mm

It is important to notice that the rack dimensions depend on the designed structure. The length is set at 100 mm to provide the maximum available traversible distance for translation.

For the rack and pinion to be compatible, their pitch must be the same. The *ZR0.4-400* rack and *ZPG0.4-13* spur gear from *HPC Gears* achieved the requirements listed in table 4.3 and was therefore selected as the rack and pinion gears for the structure. The specifications of the rack and pinion are listed in table 4.4.

Table 4.4 – Rack Specifications

Pitch	0.4	mm
Length	100	mm
Width	6	mm
Height	12	mm

Table 4.5, in turn, lists the specifications of the selected pinion gear.

Table 4.5 – Pinion Specifications

Pitch	0.4	mm
Inner Diameter	1.5	mm
Outer Diameter	6	mm
Teeth	13	
Mass	0.1	g

Further information regarding the gear choices as well as material information is available in Appendix A.

4.1.2 Design Approaches

The physical structure design, utilising the stepper motor and gear specifications, is the final step in the design process. Two differing structures are obtained depending on the design objectives that are prioritised.

A volume based approach is followed to minimise the overall volume of the structure, which in turn delivers a small, lightweight structure. In contrast, a stability based approach prioritises the overall stability and height of the structure while keeping the weight to a minimum.

In both of these cases, aluminium is used for the structure because of its low density and machining properties.

4.1.2.1 Volume Based Approach

The volume of a structure typically refers to the amount of physical space which the stationary structure displaces. This volume, which can be defined as the static volume, therefore describes the physical construction of the structure.

It is, however, also important to note the total volume of empty space that is required for the movement of the translation stage. Thus, by minimising the dynamic volume[3], the amount of wasted space is thus minimised.

Keeping the dynamic volume in mind, a two layer system was envisioned in which each layer was responsible for the linear movement in one of the axes' directions, as illustrated in figure 4.2.

---

[3]The dynamic volume refers to the volume of empty space that is used by the structure.
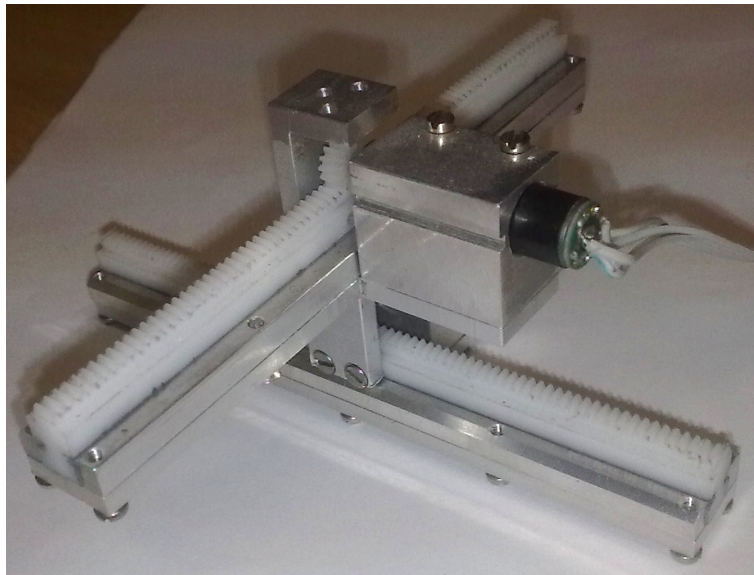
Figure 4.2 – Volume Based Approach Structure

As one can see from figure 4.2, the structure was designed to accommodate the sail attachment in the centre of the structure. The centre is therefore the zero position from which the sail can be moved along the two axes. The approximate volumes as well as specifications of this structure are listed in table 4.6.

Table 4.6 – Volume Based Structure Specifications

Physical Volume	30064	mm^3
Dynamic Volume	133235	mm^3
Calculated Mass	85.62	g
Actual Mass	88	g
Range	$\pm\,40$	mm
Height	46.1	mm

The specified masses represents the overall mass of the structure including the motors and gears that are implemented. The increased actual mass can be attributed to the weight of the screws as well as the non-ideal material properties. Although a movement range of $\pm\,40$ mm is possible along the axes, this range is limited to the required $\pm\,30$ mm to increase the stability of this approach.

Upon further investigation, it is apparent that the sliding rack has a very small support area for the top layer, thus reducing the stability. Furthermore the motors must be elevated to accommodate the interaction between the pinion and rack gears.

This structure adequately demonstrates the two-axis translation of a sail panel while satisfying all of the requirements stated in section 4.1.1. However, the stability of the system is not likely to hold during a satellite launch and an alternative design which improves upon the stability is required.

4.1.2.2 Stability Based Approach

The stability of a structure is influenced by the centre of mass and also the distribution of any forces acting upon the structure. Thus, to improve the stability of the structure one would ideally have either a larger support area or multiple support areas which could distribute the forces between the structure's load and structure's base more effectively.

The structure, illustrated in figure 4.3, is designed to utilise three layers: a bottom layer that is fixed to the satellite; a middle layer which moves upon the bottom layer; and a top layer to which the sail panel is attached. These various layers effectively distribute the forces across a larger area thereby increasing stability.
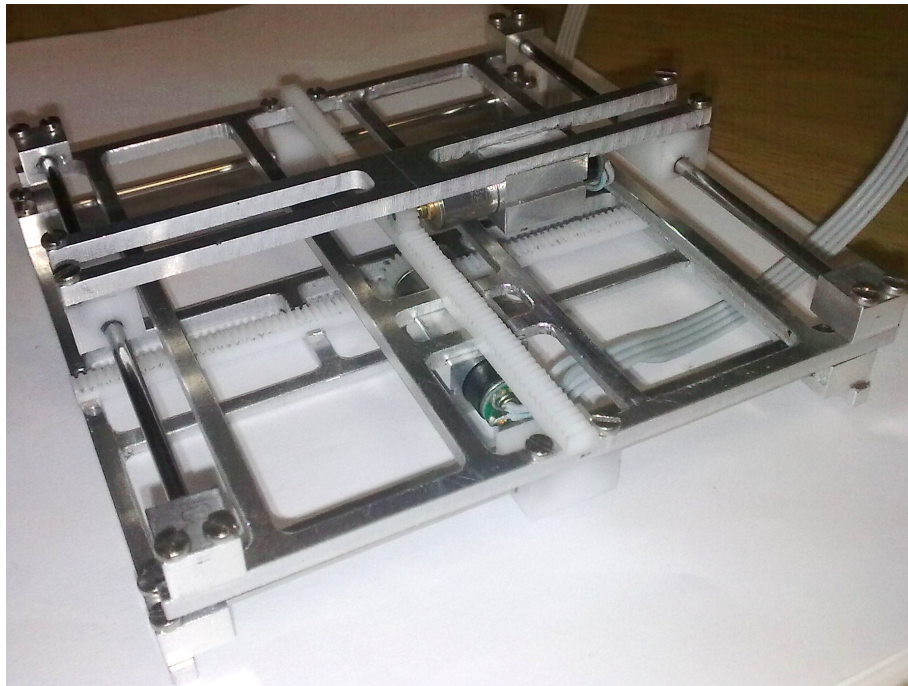
Figure 4.3 – Stability Based Approach Structure

As can be seen in this design, the rack remains stationary while the upper levels, including the stepper motor, move along two stainless steel support beams. These beams are located at the ends of the structure to improve the equal distribution of forces between the layers. All of the requirements in section 4.1.1 are satisfied by this design, the specifications of which are listed in table 4.7.

Table 4.7 – Stability Based Structure Specifications

Physical Volume	23492	mm^3
Dynamic Volume	207098	mm^3
Calculated Mass	78.5	g
Actual Mass	81.5	g
Range	$\pm$ 36	mm
Height	25	mm

The stability of the structure is greatly improved since two support beams are used while the mass of the structure, 81.5 g which includes the mass of the motors, is well below the specification of 200 g. In addition, the height has been reduced to a mere 25 mm.

4.1.3 Structure Selection

In conclusion, the two structures were empirically investigated with the results being compared in table 4.8. The best performance between the structures are indicated in bold.

Table 4.8 – Mechanical Structure Comparison

Specification	Volume		Stability	
Physical Volume	30064	mm^3	**23492**	mm^3
Dynamic Volume	**133235**	mm^3	207098	mm^3
Calculated Mass	85.6	g	**78.5**	g
Actual Mass	88	g	**81.5**	g
Range	$\pm$ **40**	mm	$\pm$ 36	mm
Height	46.1	mm	**25**	mm

As the stability and reliability of the structure are of utmost importance, the stability based design is preferred and is used for the hardware simulations. Further information regarding the construction of the structures, with focus on the various subparts, is available in Appendix B.

4.2 Magnetic Torquer Design

Magnetic torquer rods are often implemented on LEO satellites to provide magnetic attitude control by exploiting the Earth's magnetic field. As such, the requirements of these rods vary between satellites therefore necessitating a custom solution for the CubeSat design.

4.2.1 Torquer Requirements and Specifications

A magnetic torquer is essentially a length of wire that has been wound around an air or ferromagnetic core, thus giving it the potential to generate a magnetic field when current passes through the wire. Magnetic torquers can be divided into two categories, according to their cores.

The first type of magnetic torquer rod has an air core. With this type of torquer rod, the magnetic field is only active while current passes through the wire. Thus no magnetic field is generated while the torquer rod is switched off. The disadvantage associated

with this, is that one needs a lot more electrical power to generate the required magnetic moment. This increase in power requirements, makes an air core unfeasible for use on a CubeSat.

Elements can be categorised according to their relative permeability (μ_r), which is the ratio of permeability[4] (μ) of a specific material to the permeability of free space (μ_0), as given by equation 4.2.1

$$\mu_r = \frac{\mu}{\mu_0} \tag{4.2.1}$$

with $\mu_0 = 4\pi \times 10^{-7} N.A^{-2}$. The relative permeability for a few different materials are listed in table 4.9.

Table 4.9 – Magnetic Torquer Core Relative Permeabilities

Material	Relative Permeability
Mumetal	20000
Iron	5000
Nickel	600
Air	≈ 1

The second type of magnetic torquer, which is used on the CubeSat, utilises a ferromagnetic core because of the high relative permeability, thereby producing a greater magnetic moment at less electrical power. The disadvantage of using a ferromagnetic core is that there is a small remnant magnetic moment when the circuit is switched off. This remnant magnetic moment is due to the magnetisation effect that is caused by the magnetic field when the circuit is turned on.

The requirements for the magnetic torquer design are listed in table 4.10.

Table 4.10 – Magnetic Torquer Design Requirements

Required Magnetic Moment	0.2	Am^2
Saturation Magnetic Moment	≥ 0.4	Am^2
Rod Core Diameter	≤ 6	mm
Rod Length	≤ 100	mm
Total Diameter	≤ 8	mm
Wire Diameter	≥ 0.11	mm

A *Mumetal* ferromagnetic core is used for the CubeSat since it has a very high relative permeability and a material density of 8.747 g/cm^3.

---

[4]The permeability of an element is an indication of how easy a material can become magnetised.

4.2.2 Torquer Design Approach

The first step in designing the magnetorquers is to determine the rod dimensions that would deliver a magnetic moment of 0.2 Am^2. The rod dimensions and magnetic moment are related through equation 4.2.2, which is also used to determine the magnetic moment of the torquer rod.

$$M = \mu_{rod} n I A \tag{4.2.2}$$

where $\mu_{rod} = 1.66 \left(\frac{rod\_length}{rod\_diameter} \right)^2$ for a cylindrical torquer rod, [23]; n is the number of windings around the core; I is the direct current flowing through the wire; and A is the enclosed area of the coil.

As can be seen from equation 4.2.2, the decision regarding the rod dimensions inadvertently affects the number of windings, n, as well as the current, I, required to generate the specified magnetic moment.

The decision process that is implemented can briefly be summarised as follow.

1. To limit the amount of layers as well as the overall diameter, a wire with a nominal diameter of 0.2 mm is chosen with a resistivity of approximately 0.5411 $\Omega.m^{-1}$.

2. The dimensions of the magnetic torquer rod are chosen to adhere to the specifications. The length of the rod is chosen to be 60 mm with a diameter of 5 mm.

3. The direct current is investigated in the range of 10 mA to 500 mA, using 10 mA steps, for this combination of choices. For every current value, the amount of windings, equation 4.2.2, and the overall diameter of the rod, equation 4.2.3, is calculated.

$$Diameter = rod\_diameter + \frac{2n \times wire\_diameter^2}{winding\_length} \tag{4.2.3}$$

where the $winding\_length$ indicates the length of the rod around which the wire is wound.

With this process, it can be found that a current of 100 mA satisfies the magnetorquer requirements with the mumetal rod and copper wire specifications listed in table 4.11.

Table 4.11 – Rod and Wire Specifications

Rod Material	Mumetal	
Rod Diameter	5	mm
Rod Length	60	mm
Rod Permeability	0.0251	N.A^{-2}
Rod Density	8.747	g.cm^{-3}
Wire Material	Copper	
Wire Diameter	0.2	mm
Wire Length	30.51	m
Wire Resistivity	0.5411	Ω.m^{-1}
Wire Density	8.9	g.cm^{-3}
Total Windings	1477	
Total Diameter	7.868	mm

It is important to note the remnant (M_R) and saturation (M_{sat}) magnetic moments, as well as the inductance (L) associated with the torquer rods, since these may affect other circuit elements, such as the magnetometer. Equations 4.2.4 through 4.2.6 illustrates these calculations.

$$M_{sat} = \frac{B_{sat}V}{\mu_0} \tag{4.2.4}$$

$$M_R = \frac{B_r V}{\mu_0} \times \frac{\mu_{rod}}{\mu_{r(max)}} \tag{4.2.5}$$

$$L = \frac{\mu_{rod}\mu_0 n^2 A}{l} \tag{4.2.6}$$

where $B_{sat} = 0.75$ T is the saturation magnetic field density; V is the total volume of the rod; $B_r = 0.5$ T is the remnant magnetic field density; and l is the length of the rod around which the wire is wound.

The theoretical results for the chosen magnetorquer design are listed in table 4.12.

Table 4.12 – Magnetic Torquer Specifications

Resistance	16.5	Ω
Inductance	61.9	mH
Remnant Magnetic Moment	0.00032	Am^2
Saturation Magnetic Moment	0.703	Am^2

With the chosen magnetorquer satisfying all of the requirements, a prototype is manufactured, illustrated in figure 4.4, with a measured resistance of 17 Ω and overall length of 6.3 mm.
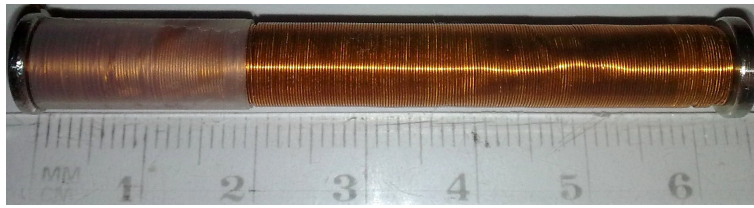
Figure 4.4 – Magnetic Torquer Rod Prototype

4.3 Hardware Implementation

The hardware implementation of the CubeSat consists of two steps: the selection of components; and the physical implemenation of these components. The application of the satellite greatly determines the necessary electronic components. Furthermore, each component must adhere to the specified minimum requirements.

After the component selections are validated, the circuitry can be illustrated with a schematic design from which a printed circuit board layout is created.

4.3.1 Component Selections

The attitude control of a satellite is done through a processor which is used to operate the stepper motors and magnetorquers. In turn, each of these peripherals require control circuitry that interfaces with the processor.

4.3.1.1 Processing Module

The processing unit is at the core of the electronics. This unit is responsible for operating the actuators and magnetometer while communicating with the on-board computer, or in this case the simulation computer.

REQUIREMENTS
In addition to a low power consumption and small physical size, the following processor requirements were identified.

- Analogue to digital conversion for the magnetometer measurements.

- Support for I^2C and USART communications.

- Pulse width modulation for the magnetorquers.

- Timers for scheduling control and measurement tasks.

A simple programmable integrated circuit (PIC) is sufficient in providing these functionalities while allowing the possiblity for upgrading to a more powerful microcontroller.

A *PIC16F767* 28-Pin quad flat no-lead package, measuring 6×6 mm^2, from *Microchip* was selected. This 5 V, low power microcontroller has a 10-bit ADC; I^{2}C and USART capabilities; three timers; and PWM capabilities. The 25 available input/output pins provides connectivity to all components while ensuring that a minimum number of unused pins remain.

IMPLEMENTATION

Since the actuators of the satellite are often simultaneously driven, an interrupt service routine is used to provide near parallel processing. The PIC is setup to use a 4 MHz clock which simplifies timing operations while maintaining processing capabilities.

4.3.1.2 Communications Module

A variety of communication methods exist that enable the exchange of data and information between systems. Communication between the on-board computer (OBC) and the satellite subsystems is of high importance. The *PIC16F767* possesses a Master Synchronous Serial Port (MSSP) module[5] as well as a Universal Synchronous Asynchronous Receiver Transmitter (USART) module. For the simulation, a desktop computer is used as OBC which communicates via USART with the PIC, thus enabling hardware-in-the-loop testing.

REQUIREMENTS

To mediate this USART communication, a *MAX232* chip is required which converts the PIC voltage level, 5 V, to the *RS-232* voltage levels, up to 15 V, which is used by the computer. Without this conversion, the computer would interpret the received data incorrectly.

IMPLEMENTATION

A baud rate of 9600 is implemented with the USART module configured on the *PIC16F767* for 8-bit, asynchronous communication. To reduce processing and memory requirements, a predefined message structure is used. Although this increases message overhead, it simplifies the command extraction process.

The actuator commands, first for the motors and then for the torquer rods, are sent from the computer to the PIC until the end of message[6] (EOM) sequence is received. The predefined message structure, including the EOM sequence, is illustrated in figure 4.5, where characters are indicated between single quotation marks.

---

[5] With Inter-Integrated Circuit (I^{2}C) and Serial Peripheral Interface (SPI) modes.
[6] This sequence can be anything, however it should not correspond to a possible actuator command.
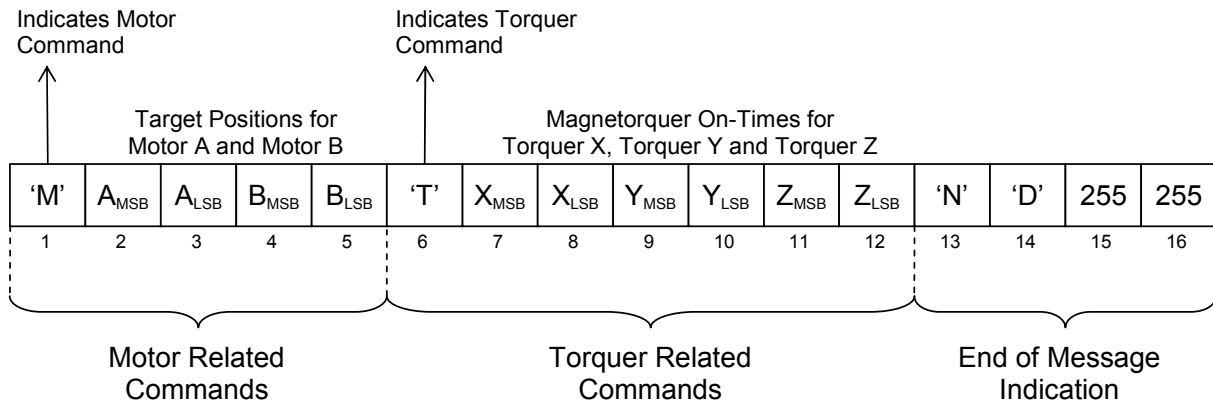
Figure 4.5 – Structure of Received Message

Once the message is successfully decoded, an acknowledge character, arbitrarily chosen as the hexadecimal value[7] *0xFC*, is sent to the computer together with the current motor positions which can be used for troubleshooting and motor position validation.

In addition, the magnetometer measurements which are taken every 10 s, is also sent to the computer using the predefined message structure indicated in figure 4.6.
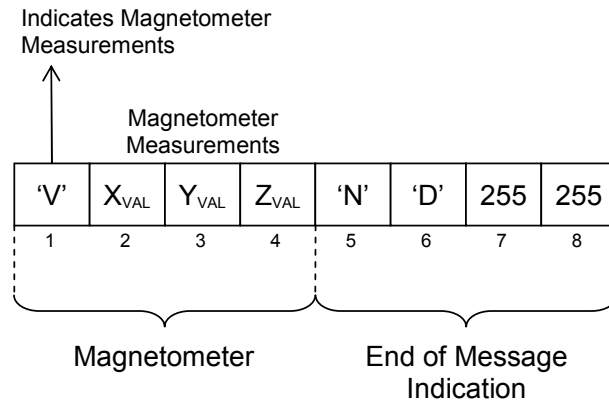
Figure 4.6 – Structure of Sent Message

4.3.1.3 Stepper Motors

Stepper motors exhibit a long lifetime, which is necessary for space applications, while delivering precise position control without needing continuous feedback. They are therefore preferred to other DC motors and are aptly suited for the accuracy required by the attitude control system. To achieve 2-axis positioning of the solar sail panel, two stepper motors are required for the structures discussed in section 4.1.

REQUIREMENTS
The primary requirements of the stepper motors can be summarised as the force generated by the motor and the accuracy obtainable due to the step resolution. In addition a

---

[7]The decimal representation being 252.

low mass and small physical size are preferrable for use in the CubeSat. These requirements are listed in table 4.13.

Table 4.13 – Stepper Motor Requirements

Motor Torque	> 0.2	mNm
Gear Torque	> 20	mNm
Step Resolution	< 0.1	mm/step
Mass	< 50	g
Diameter	< 10	mm

The physical dimensions of the stepper motors are coupled to the translation stage design, as such the design may need to be revised depending on the dimensions of the selected motor. Because of the size of the gears as well as the step resolution, the effects of backlash can be ignored.

SELECTION
Two *AM0820-V-5-56* stepper motors[8] from *Faulhaber* were selected for the translation stage. The nominal torque of the *AM0820* motor is listed as $\tau = 0.65$ mNm, which results in a force, $F = 0.25$ N, using

$$|\tau| = rF \tag{4.3.1}$$

with the inner radius of the pinion gear[9], $r = 2.6$ mm.

In addition, the full step angle of $18°$ results in $360°/18° = 20$ full steps per revolution with the circumference of the pinion gear being $2\pi(2.6) = 16.34$ mm. By using half-stepping, the minimum step resolution that is obtainable with only the stepper motor is 0.408 mm/step, equation 4.3.2.

$$\frac{Circumference}{\#Steps\ per\ revolution} = \frac{16.34}{20 \times 2} \tag{4.3.2}$$

It is thus apparent that a gear must be used in order to satisfy the design requirements. An efficiency rate of 70% is associated with the planetary gearhead *Series 08/1 64:1* from *Faulhaber*, thus the achievable torque is increased to $41.6 \times 70\% = 29.12$ mNm when using full-steps.

Using half stepping with this gear head delivers 2560 steps per revolution which, when revisiting equation 4.3.2, results in a step resolution of 0.0064 mm/step. Half stepping improves the step resolution that can be obtained and also delivers a smoother motion, however the torque is reduced by approximately 30%, [51], to $29.12 \times 70\% = 20.38$ mNm.

Table 4.14 illustrates the specifications of the selected stepper motors. The length of the motors, 34.7 mm, is small enough not to affect the translation stage design.

---

[8]The datasheet of which can be found in Appendix C
[9]Discussed in section 4.1.1.2

Table 4.14 – Stepper Motor Specifications

	Required		Achieved	
Motor Torque	> 0.2	mNm	0.65	mNm
Gear Torque	> 20	mNm	20.38	mNm
Step Resolution	< 0.1	mm/step	0.0064	mm/step
Mass	< 50	g	7.9	g
Diameter	< 10	mm	8	mm

IMPLEMENTATION

The driver circuit that is implemented for the stepper motors, is the *Dual Full Bridge Low Voltage Motor Driver, A3901* IC, from *Allegro MicroSystems*. To reduce the need for additional circuits, four output pins[10] of the PIC are used for each motor as illustrated in figure 4.7.
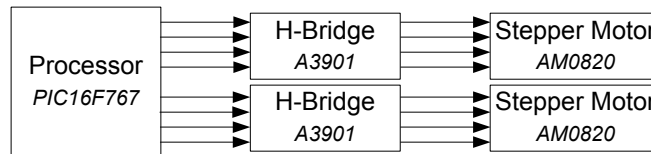
Figure 4.7 – Stepper Motor Interfacing Diagram

These pins are driven HIGH or LOW[11] to advance through the steps in the motors' rotation sequence, while the stepping speed at which the motors operate are limited by two factors.

- The minimum torque that is needed to satisfy the design specifications.

- The maximum distance that must be covered between control signal sampling times.

As the stepper motor's speed increases, it produces less torque. For the required 20 mNm torque a minimum motor torque of 40.82 mNm is required ($40.82 \times 70\% \times 70\% = 20$), taking into consideration a 70% efficiency rate and using half-steps, which corresponds to a maximum speed of approximately 1600 RPM[12].

The minimum speed can be calculated by identifying the maximum distance that has to be traversed within the 10 s control signal sampling times. Because of the very low torques, as well as the slow changes in sail position, the distance was determined as the difference between the maximum range and the zero position. The specified range, as mentioned in section 4.1.1, of ±30 mm therefore results in a worst case scenario speed of 30 mm per 10 s. The revolutions required for this translation can be calculated using

$$Revolutions = \frac{Distance}{Circumference} \times 64 = \frac{30}{16.336} \times 64 \approx 118$$

---

[10]Only two pins are necessary if inverting buffers are used.

[11]HIGH = 5 V; LOW = 0 V

[12]This speed was obtained from the motor's datasheet, refer to Appendix C.

which equates to $118 \times 6 = 708$ RPM. By implementing a 2 ms interrupt service routine (ISR) to control the motor inputs, a speed of 500 steps/s (750 RPM) is achieved thus satisfying the motor design requirements.

Two bytes are used for each stepper motor to indicate the motor position using the convention that the bytes indicate the number of half steps that the motor is from its starting position. The number of half steps associated with a distance of 30 mm can be calculated using

$$\#Half\ Steps = \frac{Distance}{(Half step\ Resolution)} = \frac{30}{0.0064} \approx 4687$$

which corresponds to $4687 \times 0.0064 = 29.999$ mm. This result is an acceptable approximation for 30 mm, since the step resolution was only required to be 0.1 mm/step.

MAINTENANCE
Even though the stepper motors provide precise positioning, minor displacements due to the mechanics of the stepper motor and rack and pinion may alter the position of the motors. In effect an offset is created where a step count of 0 would not correspond to a position of 0 mm.

Thus, to ensure the accuracy of the stepper motors, optical sensors are implemented to zero the position of the motors when required. Because only the zero position on the racks are important, it is only necessary to implement two optical sensors, *SG-2BC* from *Kodenshi*. When the sensors are pulsed, an LED emits a pulse which is then reflected back to a phototransistor. Thus by modifying the reflectivity of the rack, the optical sensor can indicate the zero position.

To determine the direction in which the zero position is located, the rack must have a high reflectivity (white) zone on one end and a low reflectivity (black) zone on the other end, illustrated in figure 4.8.

Figure 4.8 – Reflectivity for Optical Sensors

In order to centre the motors, the optical sensors are pulsed providing a 5 V signal in the reflective zone and a 0 V signal in the non-reflective zone. If the motor is in the reflective zone, it is stepped until the optical sensor indicates a 0 V which corresponds to the zero position.

If it is in the non-reflective zone, it is stepped in the opposite direction until the sensor indicates a 5 V. For this scenario, a correction of one step is necessary toward the non-reflective zone in order to zero the motor.

With this implementation, only two sensors are required with one I/O pin used for pulsing the sensors and two I/O pins implemented to indicate the reflectivity.

4.3.1.4 Magnetic Torquers

Three magnetic torquer rods are implemented to provide 3-axis magnetic attitude control for the CubeSat in LEO. The circuitry for these torquers are designed to allow current to flow in both directions across the rods, thereby allowing for positive and negative magnetic moments.

REQUIREMENTS
The mechanical requirements of the magnetorquers have already been discussed in section 4.2 therefore only the software requirements will be discussed here.

To prevent the magnetic torquer rods from interfering with the magnetometer measurements, the on-time of the rods are limited to 80% of the sampling time, $T_S = 10$ s. This allows a 2 s period for magnetic field measurements to be taken. In addition, the magnetic moments need to be centred across the 8 s magnetorquer activity period[13].

SELECTION
Because of the specific requirements and the restrictions on the physical size, the magnetic torquer rods were designed and built, as discussed in section 4.2. Although it is more time consuming to develop the magnetorquers in this way, the result is a cheaper, tailor-made solution which satisfies all of the design requirements.

The software requirements does not affect the design or selection of the magnetorquers, instead it specifies the limits which must be adhered to in the code used to control the magnetorquer rods.

IMPLEMENTATION
The magnetorquers are driven by six output pins, two for each rod, as well as a PWM signal. The purpose of this PWM signal is to reduce the time-averaged current to the necessary 100 mA target current. This replaces the need for a series resistor while improving the power efficiency.

With the magnetorquer resistance of 17 Ω, a current of $5V/17\Omega = 294$ mA is produced. To reduce this current to the required 100 mA, the PWM duty cycle must be adjusted to

$$\frac{Target\ I}{Current\ I} \times 100 = \frac{100}{294} \times 100 = 34\%$$

The PWM signal is combined with the control signals using two Schmitt-trigger NAND chips, *SN74HC132* from *Texas Instruments*, illustrated in figure 4.9.

---

[13]This represents a $0.5T_S$ delay which is similar to the zero-order-hold characteristic.
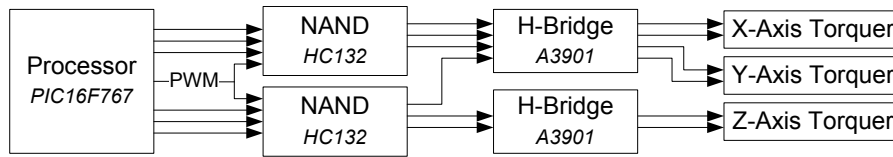
Figure 4.9 – Magnetic Torquer Rods Interfacing Diagram

A logic NAND chip is selected since it delivers a faster response than a logic AND. However, because of this, the signals are effectively inverted and therefore the duty cycle must be altered to $100 - 34 = 66\%$ in order to produce an inverted signal.

Thereafter, the combined signal is passed through a similar H-Bridge as used for the stepper motors, which supports an output current of up to 400 mA. The *A3901* full bridge driver allows the generation of positive and negative torques, depending on the direction in which the current flows. The magnetorquers can also be switched off by driving both control inputs to the same voltage level.

To control the on-time of the magnetorquers the 2 ms ISR is used with a 2-byte value indicating the direction of the torque as well as the on-time. Because the magnetic moments of the rods are centred, the minimum on-time of the torquer rods are restricted to 4 ms, (0.8 mAm^2). Therefore, a value of 2000 would correspond to $2000 \times 4ms = 8$ s, (0.16 Am^2), of positive magnetic moment, whereas -2000 would represent 8 s of negative magnetic moment.

4.3.1.5 Magnetometer

A wide range of magnetic field sensors are available, many of which are suitable for accurately measuring the Earth's magnetic field, [50]. Of these sensors there are two types that are primarily used for ADCS namely the fluxgate and the anisotropic magneto-resistive (AMR) magnetometers.

Fluxgate magnetometers tend to require more electrical power and are larger than AMR sensors, although they can provide a better accuracy. The AMR magnetometers, in contrast, are cheaper and available in small, surface mount packages making it an appropriate choice for the CubeSat design.

REQUIREMENTS
The magnetometer is not used for attitude determination, but only to provide measurements which are used in the determination of the magnetorquer on-times. Therefore, the accuracy of the magnetometer can be lowered. In addition, the accuracy of the magnetometer is directly coupled to the resolution of the magnetic moments and the capabilities of the analogue-to-digital converter (ADC).

In LEO, the Earth's magnetic field varies between 22 μT and 55 μT, as such a magnetometer is required with a full scale (FS) range of at least ± 0.6 Gauss (60 μT), allowing for offsets up to 5 μT. Because the resolution, or accuracy, of the magnetometer is primarily

limited by the ADC, the required resolution can be defined so as to allow the full scale range to be measured across a 10-bit ADC. The maximum required resolution can thus be calculated with

$$Resolution = \frac{120\mu T}{2^{10}} = \frac{120\mu T}{1024} \approx 117\ nT$$

The required magnetometer resolution should therefore be less than 117 nT over a range of $\pm 60\ \mu$T.

SELECTION

The *HMC1053* 3-axis AMR magnetometer from *Honeywell* was selected for the magnetic measurements. This magnetometer provides 3-axis measurements and is available in a leadless chip carrier (LCC) package, measuring $7.4 \times 7.4 \times 2.8$ mm³. Table 4.15 lists the required, and achieved, specifications for the magnetometer.

Table 4.15 – Magnetometer Specifications

	Required		Achieved	
Resolution	< 117	nT	12	nT
FS Range	> ± 60	μT	± 600	μT
Orthogonality			0.01	°
Linearity			0.1% FS	
Sensitivity			1	mV/V/Gauss

IMPLEMENTATION

The *PIC16F767* is used to sample the magnetometer measurements, when the magnetorquers are off. Because the voltage levels corresponding to the magnetic field measurements are in the μV range, an operational amplifier is required to convert these levels to between 0 and 5 V for the ADC. This interfacing between the PIC and magnetometer is illustrated in figure 4.10.
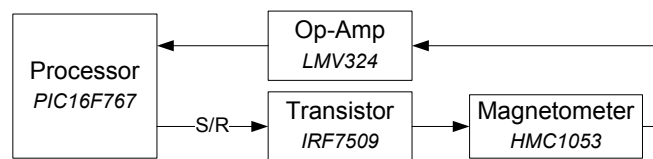
Figure 4.10 – Magnetometer Interfacing Diagram

The magnetometer is a Wheatstone bridge device with a measurement sensitivity of 1 mV/V/Gauss. In other words, 1 mV of output is obtained per 1 V of bridge voltage per gauss. With a bridge voltage of 5 V, this equates to a $(5\ \text{V} \times 0.6)/1\ \text{mV} = 3000\ \mu\text{V}$ difference for a 0.6 Gauss (60 μT) magnetic field.

As already mentioned, this 3000 μV must be amplified in order for the ADC to accurately detect measurement changes. An ADC operating range between 0.5 and 4.5 V, with a 2.5 V reference voltage, provides a 4 V allocation for the $\pm 3000\ \mu$V ($\pm 60\ \mu$T) range of values. The op-amp gain associated with this 4 V range can thus be calculated, as illustrated in equation 4.3.3.

$$\frac{4 \ V}{6000 \ \mu V} = 666.7 \approx 667 \tag{4.3.3}$$

The resistors that are typically available restricts this gain even further. Using a typical differential amplifier configuration, with the available resistors having values R1 = 5.1 KΩ and R2 = 2.7 MΩ, provides a practical gain of R2/R1 $\approx$ 529 which corresponds to a 3.17 V range between 0.91 V (-60 μT) and 4.09 V (60 μT).

With the 10-bit ADC, voltage increments of $5/1024 = 4.88$ mV is detectable resulting in an ADC count, for the range between 0 and 60 μT, of

$$\frac{4.09 - 2.5 \ \text{V}}{4.88 \ \text{mV}} \approx 326$$

which gives a final implemented magnetic field resolution of $60 \ \mu$T$/326 \approx 184$ nT. Similarly, the ADC count which corresponds to the various voltage measurements can be calculated with equation 4.3.4.

$$\frac{x \ V}{5 \ V} \times 1024 \tag{4.3.4}$$

Using this equation, with the current implementation having a reference voltage of 2.5 V and gain of 529, the op-amp voltages, their corresponding magnetic field values as well as the ADC counts can be calculated, as listed in table 4.16.

Table 4.16 – Magnetometer ADC

Magnetic Field [μT]	Op-Amp Output Voltage [V]	ADC Count
-60	0.91	186
-55	1.04	213
-22	1.92	393
0	2.5	512
22	3.08	631
55	3.96	811
60	4.09	838

To obtain an accurate magnetic field measurement, more than 10 samples are needed which are then averaged. Accurate measurements are thus available by taking 16 samples, while this also allows the average to be determined on the PIC using a simple bit shift operation.

Furthermore, to ensure the continued accuracy of the magnetometer, a set/reset (S/R) signal is necessary which conditions the magnetic domains of the magneto-resistive elements. These S/R signals also provide an effective technique for the cancellation of any electronic offsets by taking the difference between measurements after altering the S/R state[14].

---

[14]This process is described in more detail in Appendix D.

4.3.2 Circuit Design and Layout

With the required functionality of the various eletronic and mechanical components completed, the physical circuit must be designed and implemented before the PIC software can be developed and tested.

4.3.2.1 Initial Design and Layout

The first step to producing the circuit board is to map the I/O pins of the PIC to the corresponding functionalities and electronic components. This mapping of the I/O pins provides a logical summary of the required connections with a clear indication of unused pins.

The calculations and circuit design decisions are not associated with the thesis outcomes and will therefore not be discussed in detail. The information for these decisions can be found in the respective component datasheets and also in a variety of textbooks, [17], [51], [52], [53], and [54]. By applying this information, an initial circuit schematic, illustrated in figure 4.11, can be constructed using software such as *Design Explorer* from *Altium*.

Figure 4.11 – Circuit Schematics

After confirming the schematic design, it is possible to depict the printed circuit board design (PCB) with the physical size and connections of the various components. Because the circuit board must fit within a CubeSat, the entire layout must be completed on a circuit board less than 10×10 cm^2, as illustrated in figure 4.12.

Figure 4.12 – Printed Circuit Board Layout

This initial circuit layout acts as a prototype, allowing relatively cost-free adjustments where necessary before a final design is completed.

4.3.2.2 Revising the PCB

The hardware implementation and testing often brings to light further design requirements. Whether it is because of additional functionality, or for the sake of improvement, such requirements can introduce a change in the components or even layout of the circuit elements. With this in mind, the following adjustments were made to the initial circuit.

- To use pin *RA4* a pull-up resistor was added.

- The stepper motors were rewired in order for both motors to be controlled on *Port B*.

- A reference voltage of 2.5 V was added for the magnetometer on pin *RA3*.

- The *IRF7509* IC connection was moved from pin *RA3* to pin *RC5*.

- The gain of the magnetometer op-amp was altered, thus changing the gain resistors to 2.7 MΩ and 5.1 KΩ.

These changes are considered internal to the circuit layout, though external changes are also necessitated by the absence of the other CubeSat circuits. A 5 V constant voltage regulator is thus implemented to simulate the power supply component, which is also used to provide the 2.5 V reference voltage for the ADC. The use of a computer in place of the on-board computer also required the addition of a *MAX232* IC to convert the signal between the PIC and *RS-232* voltage levels.

70

4.4 Software Implementation

The software implementation can be divided into two categories. Firstly the PIC code, written with *MPLAB IDE* from *Microchip*, is used for physically controlling the electronic and mechanical components. On a secondary level, the simulation code is written in *Matlab* to do simulated tests, with and without the hardware components. These two categories of code are discussed next.

4.4.1 Controlling the Hardware

The PIC must be programmed to manage the actuators of the CubeSat as well as provide communication with a computer. To summarise, the PIC must be able to provide the following functionality.

- Control of the translation stage with stepper motors.

- The enabling and disabling of the magnetic torquers for specific time periods.

- Periodic sampling of the magnetometer measurements.

- Communication with the computer using USART.

These functions can further be divided into time-critical functions and non-time-critical functions. As such, the control of the actuators are identified as time-critical functions whereas the communication functionality can be categorised as a non-time-critical function. The non-time-critical functions are placed within the main program, illustrated in figure 4.13, and are responsible for receiving and decoding messages; determining the control signals; and returning results to the computer.
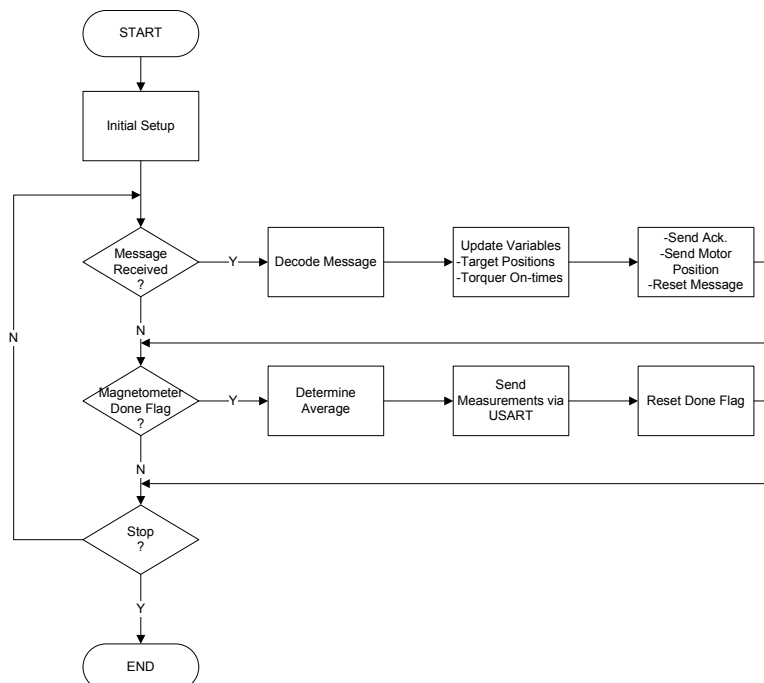
Figure 4.13 – Flowchart of the Main Program

As already mentioned, the time-critical functions are associated with the actuator control signals. The actuator signals are time-critical because the control must happen within the 10 s sampling period.

A 2 ms ISR is used to manage the control signals, thereby keeping track of the timing intervals while not overloading the processor. Figure 4.14 illustrates the flow of a typical interrupt service routine.
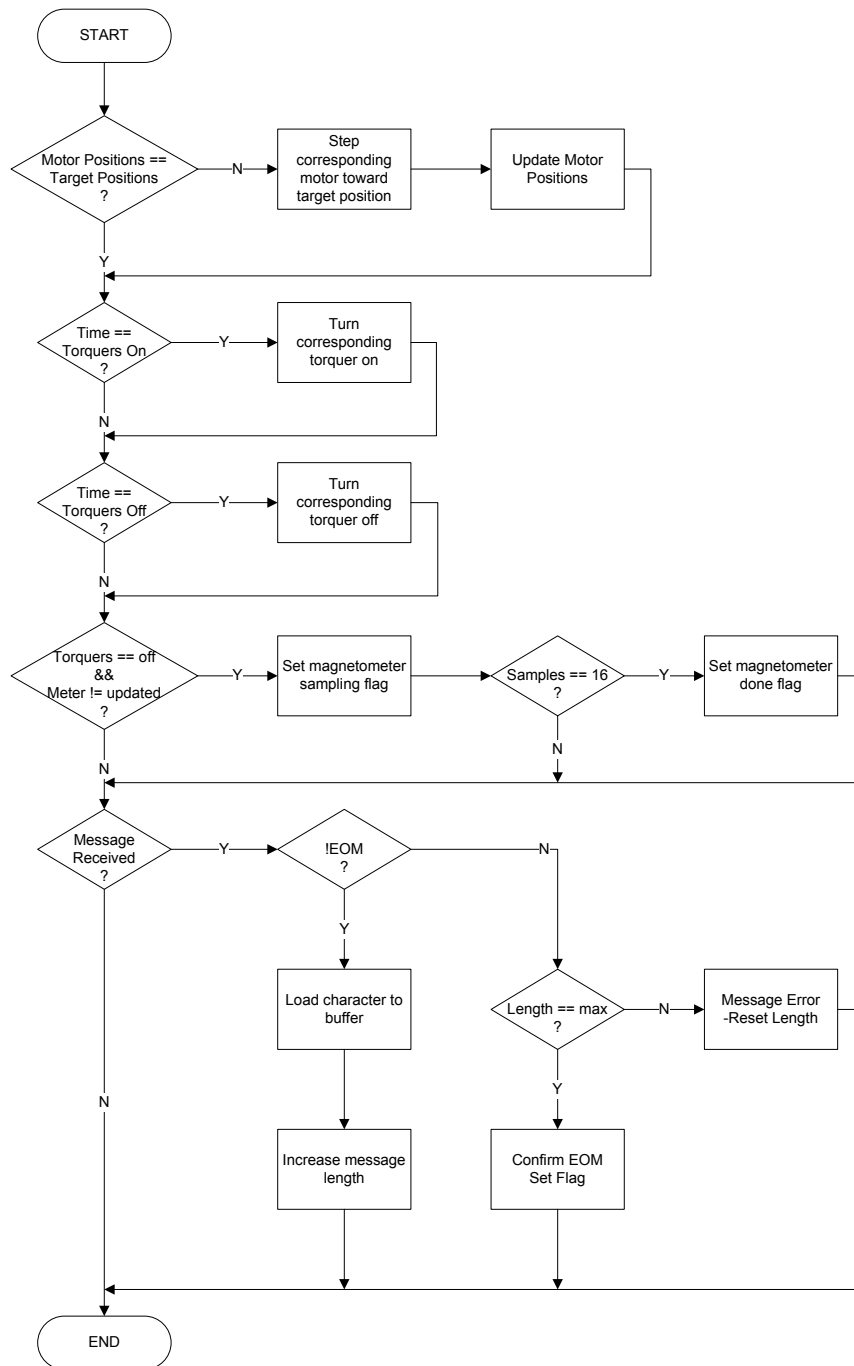
Figure 4.14 – Flowchart of ISR Functions

Since the two stepper motors operate with the same functions it is only shown once in the flowchart. For each motor, the current position is compared to the target position after which, if necessary, the motor advances one step in the target direction.

Similarly, the functions for the magnetorquers remain the same for each of the torquers and are therefore summarised in the generic function blocks. The number of ISR calls are tracked, thus allowing time-keeping in 2 ms intervals which is used to determine the start and stop times of the magnetorquers. To centre the magnetorquer pulses can be done by simply subtracting the half of the on-time from the centre time of 5 s.

The time-keeping ability also ensures that the magnetometer measurements are taken when the magnetorquers are switched off, although the actual measurements are taken in the main program. The buffering of received characters on the USART channel is also performed in the ISR. If the message is received successfully, a flag is set indicating that the message must be decoded in the main program.

The buffering of messages allows for communication to take place at any time interval, while the continuous switching between the ISR and main program ensures that no interference is possible with the timely execution of the actuator control commands.

4.4.2 Simulating with Matlab

Matlab is a powerful tool which is implemented to illustrate the feasibility of the proposed CubeSat through the use of detailed simulations. As such, it is used to simulate the orbit of the CubeSat using approximations of the satellite and orbit models, while the estimator and control algorithms can also be tested on the modelled data.

The *Simulink* model, figure 4.15, illustrates the connections between the satellite models, the control and the estimation algorithms.
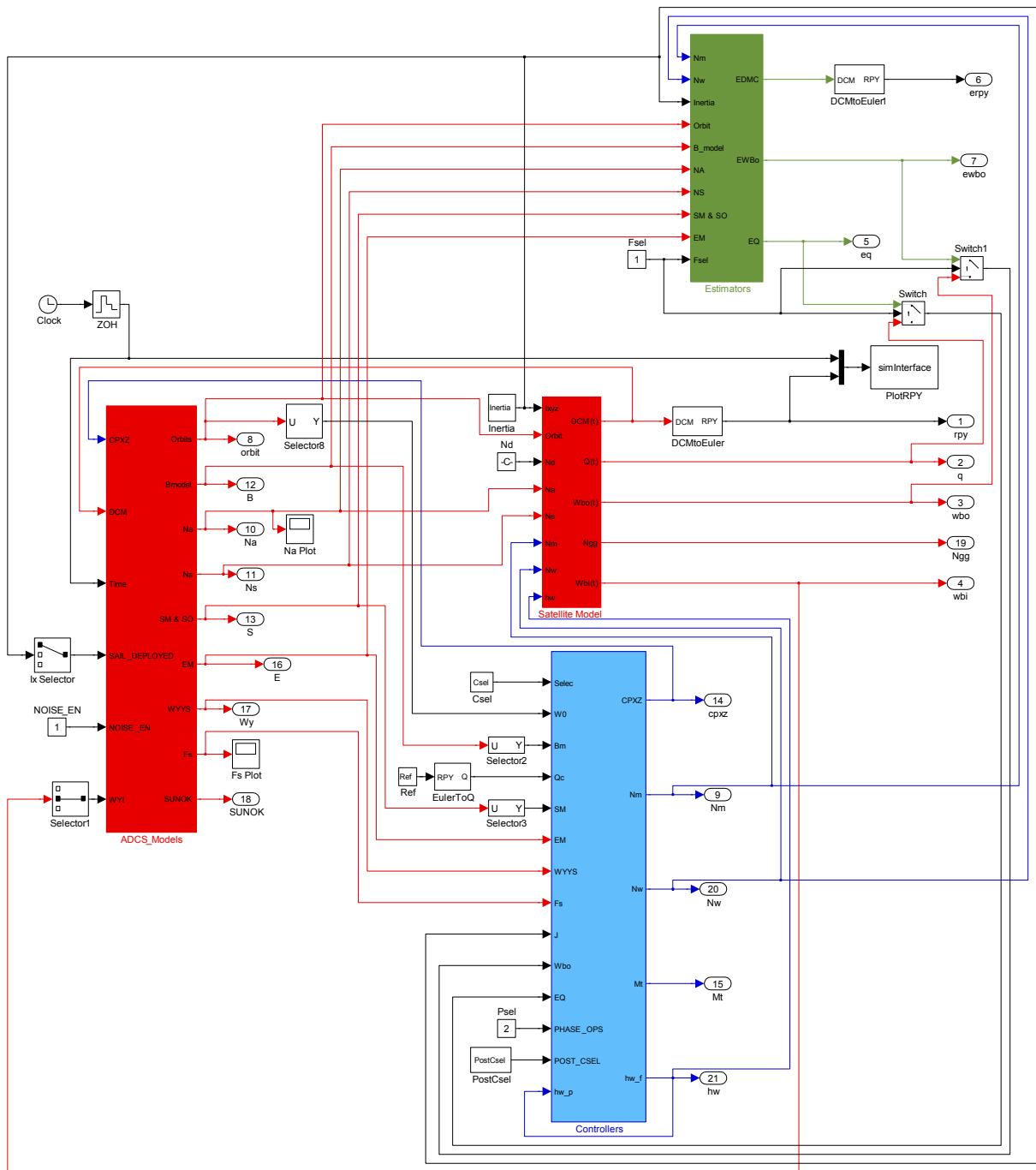
Figure 4.15 – CubeSat Simulink Model

By implementing a simple graphical user interface, illustrated in figure 4.16, it is possible to simulate only certain phases of the satellite's orbital lifetime with the selected attitude controllers.

More information regarding the simulation design, setup and implementation, including simulation results, are available in chapter 5.
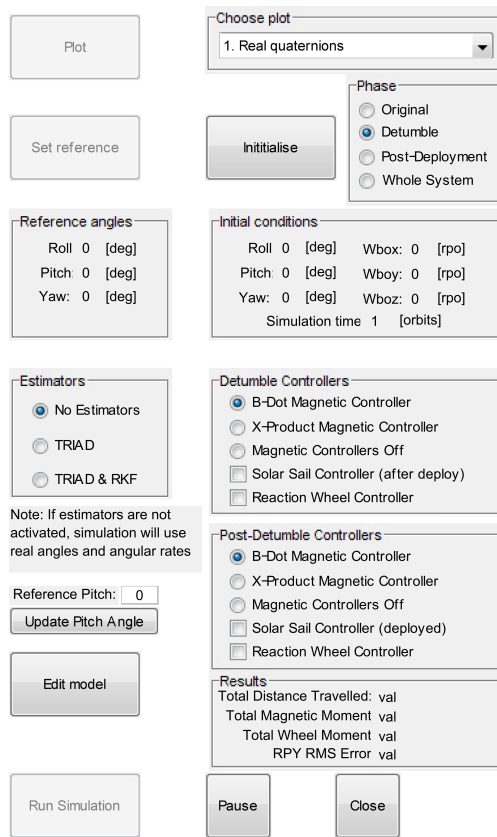
Figure 4.16 – Matlab Graphical User Interface

4.4.2.1 Hardware in the Loop Testing

Through the results of the simulations, the theoretical feasibility of various attitude control algorithms can be investigated while the validation and effectiveness of these control algorithms are only possible after the satellite has been launched. The mechanical and electronic implementation of the control system can however be tested and validated using hardware-in-the-loop simulations. The original simulation remains unaltered, however the calculated control signals are sent to the PIC via a serial connection. Figure 4.17 illustrates the additions required to the *Simulink* model, figure 4.15, to allow serial communication and thus the simulation of the hardware components.
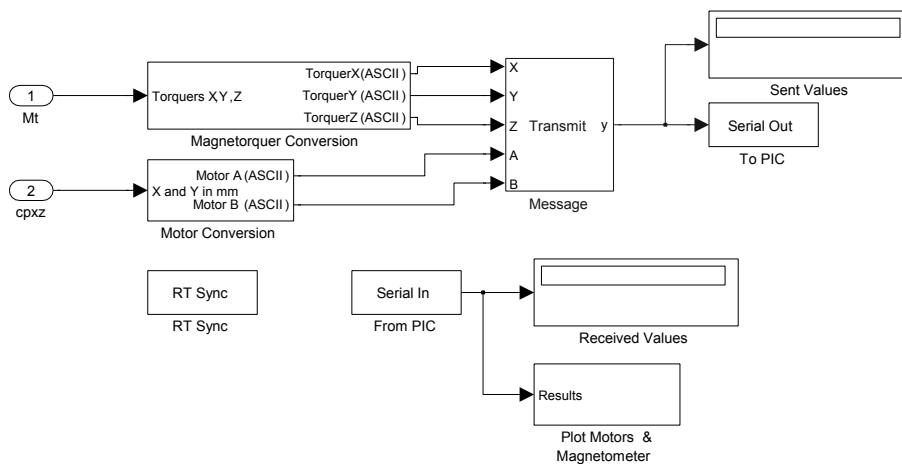
Figure 4.17 – Hardware in the Loop Interfacing

As can be seen from figure 4.17, the control signals are first converted to byte representations which are then combined into a predefined message structure. This message is then sent to the PIC, decoded and implemented in the hardware components. The simulation is run in real-time, making it possible to visually validate the movement of the translation stage with the calculated distances.

To illustrate the operation of the magnetorquer rods, a series of LEDs are implemented to indicate the on-time of the rods. Although the magnetometer measurements remain unchanged, by sending these measurements to the computer the accuracy as well as correct operation of the magnetometer can be verified.

As a result, the practical implementation and feasibility of the mechanical structures have been confirmed and validated against the simulation results.

Chapter 5

Results and Discussion

Computer simulations are the most powerful and least expensive tools available to investigate the feasibility and effectiveness of various control algorithms.

In this chapter the basic configuration used for the CubeSat simulations are introduced, followed by the initial simulation results of the solar sail and magnetorquer controllers. The addition of a y-axis reaction wheel is then investigated while comparing the results that were obtained using various reaction wheel controller gains.

The chapter is concluded with a discussion in which the optimal added reaction wheel simulation is compared to the initial solar sail simulation, without the reaction wheel.

5.1   Simulation Design Setup

The current system design was created to investigate the effectiveness and to illustrate the use of a solar sail on a cube satellite. Three magnetorquer rods and a solar sail were used to manipulate the satellite's attitude. In addition to this base scenario, the effects of using a reaction wheel for controlling the pitch axis attitude was also investigated.

After the satellite has been deployed from the P-POD [55] (Poly Picosatellite Orbital Deployer), a Bdot [46] magnetic controller was implemented to quickly dump the X_B and Z_B axes angular rates while the Y_B axis was aligned normal to the orbital plane. When the satellite is in a safe Y-Thompson spin [49], the sail is deployed thereby reducing the ω_{yi} spin rate to $-0.25 \, °/s$.

Once the satellite has been succesfully detumbled, the Bdot magnetic controller is replaced by the cross-product [46] and solar sail controller. A Q-Feedback PD controller was implemented for the solar sail controller, while the magnetic attitude controller was based on the cross-product control law using a PD quaternion feedback error vector **e**. The control equations for this base scenario are illustrated in equations 5.1.1 and 5.1.2.

$$r_{cntr\_z} = -120\hat{\omega}_{xo} - 0.6\hat{q}_{1e}$$

$$r_{cntr\_x} = +120\hat{\omega}_{zo} + 0.6\hat{q}_{3e} \tag{5.1.1}$$

$$\mathbf{e} = \begin{bmatrix} 80\hat{\omega}_{xo} + 0.2\hat{q}_{1e} \\ 180\hat{\omega}_{yo} + 0.3\hat{q}_{2e} \\ 80\hat{\omega}_{zo} + 0.2\hat{q}_{3e} \end{bmatrix} \tag{5.1.2}$$

with r_{cntr_x} and r_{cntr_z} the distances that the sail is shifted in the X_B and Z_B axes; $\hat{\omega}_{xo}$, $\hat{\omega}_{yo}$, and $\hat{\omega}_{zo}$ the estimated orbit referenced angular rates; and $\hat{q}_{1e}$, $\hat{q}_{2e}$, and $\hat{q}_{3e}$ the estimated attitude quaternion errors.

Due to the orientation of the solar sail, the solar radiation pressure is dominant in the orbit fixed inertially referenced direction $\bar{Y}_O^I$. Because of this alignment a dominant control torque can be generated around the roll, ϕ, and yaw, ψ, axes. Less magnetic control torques are therefore required for these axes, allowing the magnetic torquer controller to focus on controlling the pitch, θ, angle. This design decision becomes apparent when investigating the current controller gains shown in equations 5.1.1 and 5.1.2.

The same is true when investigating the reaction wheel simulation, although the reaction wheel is implemented to control the pitch attitude while the y-axis magnetic control torque is only used to control the speed of the reaction wheel.

The configuration setup of the simulation, including the initial angular rates and final reference angles, is listed in table 5.1. This configuration has been used for all of the comparisons that are done in sections 5.2 and 5.3.

Table 5.1 – Simulation Configuration

Noise	Enabled		
Simulation Time	5 orbits		
Estimator	TRIAD		
Controllers:	Solar Sail Controller		
	Magnetic Controller		
	Reaction Wheel Controller		
Initial Angles:	Roll (ϕ)	-5	°
	Pitch (θ)	20	°
	Yaw (ψ)	5	°
Initial Rates:	ω_{xi}	0	°/s
	ω_{yi}	-0.25	°/s
	ω_{zi}	0	°/s
Reference Angles:	Roll (ϕ)	0	°
	Pitch (θ)	0	°
	Yaw (ψ)	0	°

To effectively compare the different simulations, some common criteria were needed to illustrate the efficiency of the simulation. The following criteria were identified for these comparisons.

Distance Travelled The summation of the absolute distances travelled by the solar sail panel in both the X_B and Z_B axes.

Magnetorquer On-Time The summation of the on-time for all three of the magnetorquers.

Control Torques The sum of the controllable torques required to successfully control the satellite's attitude. The controllable torques referred to are the magnetic, solar radiation pressure, and reaction wheel torques.

RPY RMS Error The root mean square (RMS) error between the actual and reference roll, pitch, and yaw (RPY) angles.

Each criterion, except for the RPY RMS error, was calculated over the period of the simulation, 5 orbits. By taking into account that the control signals have a sampling time of 10 s, one can then calculate the distance travelled using equation 5.1.3.

$$
distance = \sum_{t=1}^{T_R/10} |r_{cntr\_x}(10t) - r_{cntr\_x}(10t - T_s)|
$$

$$
+ \sum_{t=1}^{T_R/10} |r_{cntr\_z}(10t) - r_{cntr\_z}(10t - T_s)| \tag{5.1.3}
$$

with the control signal sampling time $T_s = 10\ s$, and the simulation run time $T_R = 30000\ s$.

The maximum magnetic moment, discussed in section 4.2, is $0.2\ Am^2$ with a maximum on-time of 80%[1]. Thus $0.2\ Am^2$ can be generated in 10 s, while $0.8 \times 0.2 = 0.16\ Am^2$ can be generated in $0.8 \times 10 = 8\ s$. Using this information, one can calculate the magnetorquer on-time using equation 5.1.4.

$$
M_{on-time} = \sum_{t=0}^{t=T_R/10} (|M_X(10t)| + |M_Y(10t)| + |M_Z(10t)|) \times \frac{8}{0.16} \tag{5.1.4}
$$

---

[1]As mentioned previously, the 80% on-time allows accurate magnetic measurements to be taken while the magnetorquers are off.

with the simulation run time $T_R = 30000\ s$; and M_X, M_Y, and M_Z the magnetic moments generated in the orbit referenced axes.

The control torque is probably the most important factor when comparing the different simulations. The lower the control torque is, the less control effort is required to adjust the satellite's attitude and therefore the power consumption is decreased. The settling time of the controlled signals have a large influence on the magnitude of these control torques. As one can expect, a faster settling time requires more control effort resulting in higher control torques.

The total magnetic control torques, N_{MT}, solar disturbance torques, N_{Solar}, and reaction wheel torques, N_W, can be calculated using equations 5.1.5 to 5.1.7.

$$N_{MT\_total} = \sum_{t=0}^{t=T_R} |N_{MT\_X}(t)| + |N_{MT\_Y}(t)| + |N_{MT\_Z}(t)| \tag{5.1.5}$$

$$N_{Solar\_total} = \sum_{t=0}^{t=T_R} |N_{Solar\_X}(t)| + |N_{Solar\_Y}(t)| + |N_{Solar\_Z}(t)| \tag{5.1.6}$$

$$N_{W\_total} = \sum_{t=0}^{t=T_R} |N_{W\_X}(t)| + |N_{W\_Y}(t)| + |N_{W\_Z}(t)| \tag{5.1.7}$$

For the base scenario (without the reaction wheel), the reaction wheel torques $N_W = 0$. For the reaction wheel scenarios, only one reaction wheel is used to control the pitch attitude, therefore equation 5.1.7 can reduce to

$$N_{W\_total} = \sum_{t=0}^{T_R} |N_{W\_Y}(t)|$$

The total control torque is a summation of the above mentioned individual torques, as illustrated in equation 5.1.8.

$$N_{total} = N_{MT\_total} + N_{Solar\_total} + N_{W\_total} \tag{5.1.8}$$

The root mean square error was calculated by taking the square root of the mean square error between the actual and reference roll, pitch, and yaw angles, as illustrated in equation 5.1.9.

$$RMSE = \sqrt{\frac{\sum_{t=n}^{T_R} |\phi - \phi_{ref}|^2 + |\theta - \theta_{ref}|^2 + |\psi - \psi_{ref}|^2}{T_R + 1 - n}} \qquad (5.1.9)$$

with the simulation run time $T_R = 30000\ s$; ϕ, θ, and ψ the real RPY angles; and ϕ_{ref}, θ_{ref}, and ψ_{ref} the reference RPY angles. The RMS error start time, n, can be varied to exclude the transient effects on the RMS error. The original simulations are discussed next.

5.2 Initial Simulation Scenarios

In this section the initial simulation scenarios are investigated. Firstly the original simulation without the reaction wheel controller is evaluated. The initial reaction wheel scenario is then described and investigated after which the two scenarios are compared.

5.2.1 Base Scenario without Reaction Wheel

The roll, pitch, and yaw angles of the base simulation, without the reaction wheel, are illustrated in figure 5.1. Controlling the pitch angle to within $2°$ of the reference angle took 3.46 orbits (20922 s) as illustrated by the absolute error in figure 5.2. The absolute error is the difference between the actual and reference roll, pitch, and yaw angles.
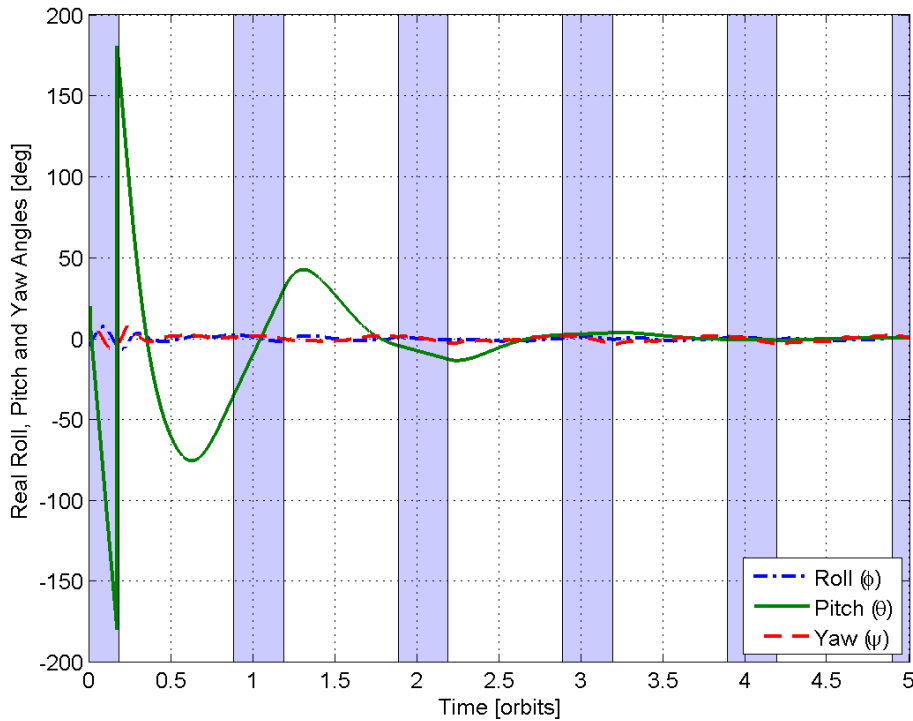
Figure 5.1 – RPY Angles of the Base Scenario - No Wheel
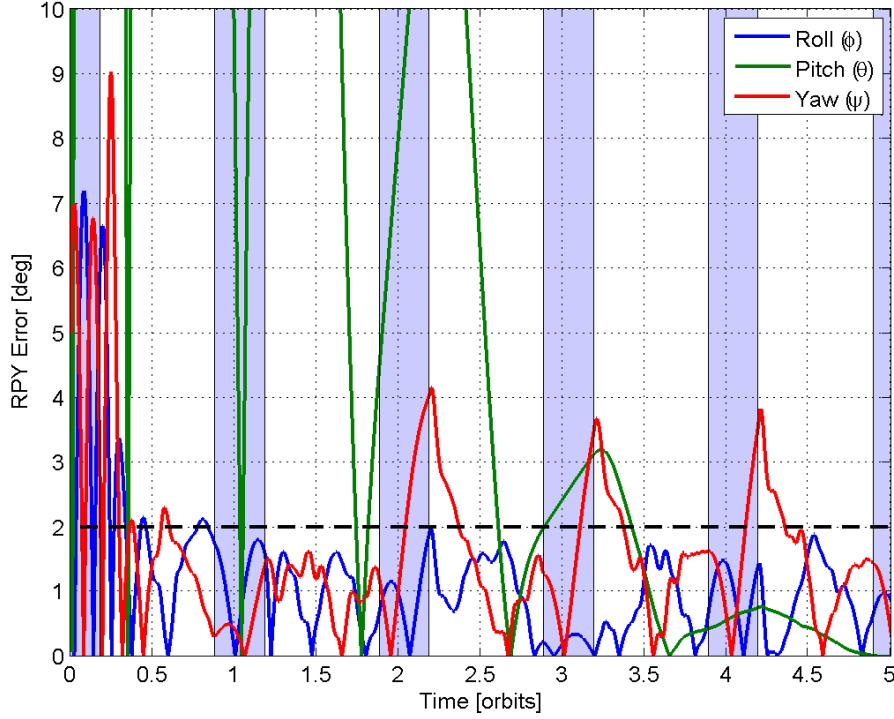
Figure 5.2 – Absolute RPY Error of the Base Scenario - No Wheel

The root mean square error after a transition period of n orbits are listed in table 5.2. The transition period indicates the number of orbits, at the start of the simulation, to ignore in the RMSE calculation.

Table 5.2 – RPY RMS Errors of the Base Scenario - No Wheel

Transition Period [orbits]	RMSE [°]
0	19.93
1	7.36
2	3.15
3	1.50
4	1.31

When comparing the RMS errors to the RPY angles illustrated in figures 5.1 and 5.2, one can clearly see that the contribution made to the RMS error during the transition period is a direct result of the settling time and the initial conditions in which the satellite is in eclipse and has an ω_{yi} spin rate of $-0.25\,°/s$.

For comparison purposes it is therefore better to compare the RMS errors after the settling time, t_s, has been reached, although it is important to note the different settling times for the various simulations.

The results obtained from the original simulation are listed in table 5.3. Because of the nature of the cross-product control law, an error in the X and Z axes affects the torque generated with the Y-axis magnetic torquer rod.

Table 5.3 – Simulation Results of the Base Scenario - No Wheel

	With Noise		Without Noise	
Total Translated Distance	1.60	m	0.64	m
Total Magnetorquer On-Time	1444	s	1439	s
2° Settling Time	20922	s	20638	s
Control Torque	16.44	mNm		
Magnetic Torque	8.64	mNm		
Solar Sail Torque	7.80	mNm		

As can be seen from these results, the translated distances are greatly increased due to the effects of noise, while the magnetic controller is more robust against the effects of noise.

The real ECI angular rates are shown in figure 5.3.
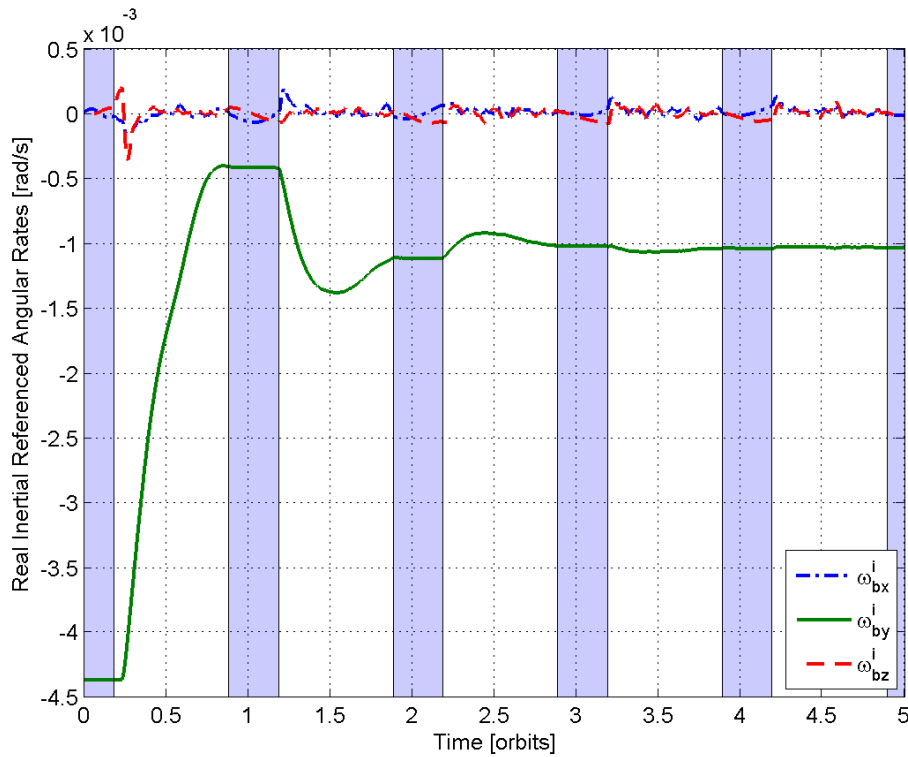
Figure 5.3 – Real ECI Angular Rates of the Base Scenario - No Wheel

The resulting magnetic moments and solar sail XZ-translation are illustrated in figures 5.4 and 5.5.
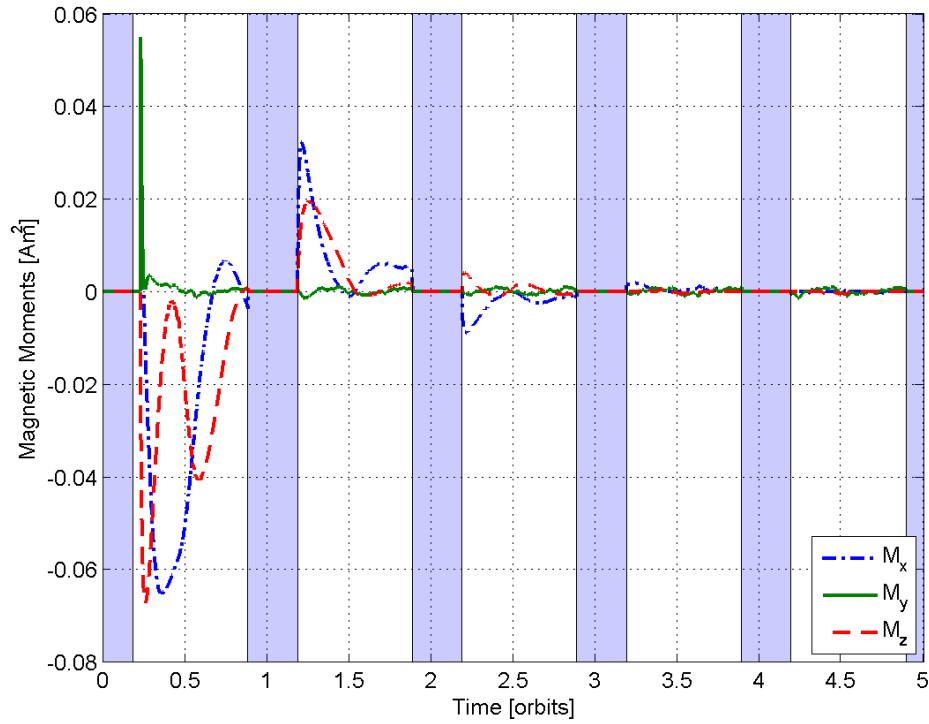
Figure 5.4 – Magnetic Controller Moments of the Base Scenario - No Wheel
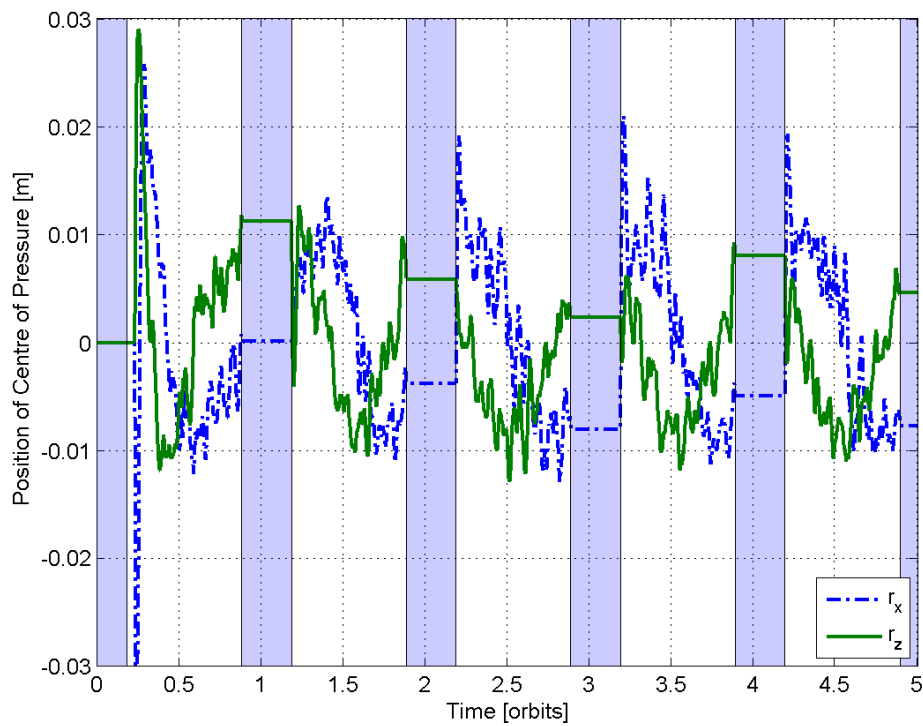
Figure 5.5 – Motor Translation of the Base Scenario - No Wheel

5.2.2 Base Scenario with Reaction Wheel

The current controllers have already been investigated and improved to obtain the best gain selection for the attitude control of the satellite. It was therefore decided to extend the controllers to include a reaction wheel which would be used to control the pitch rate and angle of the satellite. The Y-axis magnetic torquer would then only be used to control the speed of the reaction wheel. Due to the small size and weight of the cube satellite, it was decided to investigate the effects of a relatively small reaction wheel. The specifications of the chosen reaction wheel are listed in table 5.4.

Table 5.4 – Reaction Wheel Specifications

Maximum Torque	2	mNm
Nominal Momentum	15	mNm.s
Maximum Momentum	30	mNm.s

The solar sail panel translation controllers have remained the same. But since the reaction wheel is now responsible for the pitch controls, and the Y-axis magnetic torquer is used to control the speed of the reaction wheel, the control equations change as illustrated in equation 5.2.1, with the quaternion feedback PD reaction wheel controller illustrated in equation 5.2.2.

$$\mathbf{e} = \begin{bmatrix} 80\hat{\omega}_{xo} + 0.2\hat{q}_{1e} \\ K_Y(h_{wy} - h_{wy-ref}) \\ 80\hat{\omega}_{zo} + 0.2\hat{q}_{3e} \end{bmatrix} \tag{5.2.1}$$

$$N_{wy} = K_D J_{YY} \hat{\omega}_{yo} + K_P J_{YY} \hat{q}_{2e} \tag{5.2.2}$$

where K_Y is the magnetic controller derivative gain used to control the speed of the reaction wheel, K_D is the derivative gain and K_P is the proportional gain used by the reaction wheel controller to control the pitch angles. $J_{YY} = 1.376$ is the inertia of the satellite along the Y-axis with the solar sail deployed and h_{wy} is the reaction wheel momentum. The reference momentum, h_{wy-ref}, was chosen to be -0.015 Nm.s to accommodate a momentum range from -0.03 Nm.s to 0 Nm.s.

A 10% error was associated with the momentum wheel, therefore $|h_{wy} - h_{wy-ref}| = 0.1 \times 0.015 = 0.0015$ Nm.s. The initial magnetic controller derivative gain, K_Y, was chosen so that the resultant error would be near the X and Z axes errors. Using equations 5.2.1, 5.2.3 and 5.2.4, we can calculate the initial value of $K_Y = 187$.

$$e_X = 80(\hat{\omega}_{xo}) + 0.2(\hat{q}_{1e}) = 80(0.001) + 0.2(1) = 0.28 \tag{5.2.3}$$

$$e_Y = K_Y(0.0015)$$

$$K_Y = \frac{e_Y}{0.0015} = \frac{0.28}{0.0015} = 186.\dot{6} \tag{5.2.4}$$

with e_X and e_Y the feedback errors in the X and Y axes; $\hat{\omega}_{xo}$ the estimated X axis angular rate; and $\hat{q}_{1e}$ the estimated X axis quaternion error. To determine the expected value of the feedback error, a worst case quaternion error, $\hat{q}_{1e} = 1$ was used with $\hat{\omega}_{xo} = 0.001$ corresponding to the orbital Y axis angular rate.

Because the e_Z and e_X gains are identical, as illustrated in equation 5.2.1, the same result would have been obtained if the e_Z feedback error, with $\hat{q}_{3e} = 1$ and $\hat{\omega}_{zo} = 0.001$, was used rather than the e_X feedback error.

The proportional and derivative gains of the reaction wheel controller can be calculated using equations 5.2.5 to 5.2.7, [56], with an optimally damped scenario, $\zeta = 0.707$.

$$K_D = 2\zeta\omega_n \tag{5.2.5}$$

$$K_P = 2\omega_n^2 \tag{5.2.6}$$

$$e^{-\zeta\omega_n t_s(2\%)} \leq 0.02 \tag{5.2.7}$$

To prevent the reaction wheel torque from saturating too quickly, it was decided to limit the proportional gain with regards to the maximum possible torque, as shown in equation 5.2.8.

$$K_P < \frac{N_{max}}{J_{YY}} < 0.00145 \tag{5.2.8}$$

This effectively limits the natural frequency, ω_n [rad/s], which in turn affects the derivative gain and minimum 2% settling time, $t_s(2\%)$ [s], that can be accounted for, as illustrated in equations 5.2.9 to 5.2.11[2].

---

[2]These equations are derived from equations 5.2.5 to 5.2.7.

$$\omega_n < \sqrt{\frac{N_{max}}{2J_{YY}}} < 0.0270 \tag{5.2.9}$$

$$K_D < 2\sqrt{\frac{N_{max}}{2J_{YY}}} < 0.0381 \tag{5.2.10}$$

$$t_s(2\%) > \frac{-\ln(0.02)}{\zeta\omega_n} > 206 \tag{5.2.11}$$

To visualise the effects of varying the K_D and K_P gains, the natural frequency ω_n has been tweaked. A maximum frequency $\omega_n = 0.0269$ rad.s^{-1} was chosen and divided into sixteenths. A good range of gains was thereby achieved, as illustrated in table 5.5.

Table 5.5 – Range of Gain Values due to ω_n Limitation

ω_n [rad/s]	K_D	K_P
$1/16 \times 0.0269$	2.38E-3	5.65E-6
$2/16 \times 0.0269$	4.76E-3	2.26E-5
$4/16 \times 0.0269$	9.51E-3	9.05E-5
$8/16 \times 0.0269$	1.90E-2	3.62E-4
$12/16 \times 0.0269$	2.85E-2	8.14E-4
0.0269	3.80E-2	1.45E-3

The K_D and K_P gains are associated with the control of the RPY angles. It was found that the gains associated with two sixteenths of the natural frequency, $\omega_n = 0.00336$ rad.s^{-1}, controlled the RPY angles efficiently, while the angles would not drift too far from the reference angles when the satellite enters eclipse. That is to say, the angular rates are regulated in such a way that good control is possible during sun exposure, while the angular rates that are reached when the satellite enters an eclipse does not cause the satellite to rapidly drift away from its reference RPY angles.

The gains that were chosen for the base scenario with the reaction wheel are $K_Y = 187$, $K_D = 4.76$E-3, and $K_P = 2.26$E-5. The RPY angles for this scenario are illustrated in figure 5.6, with the absolute error in figure 5.7.
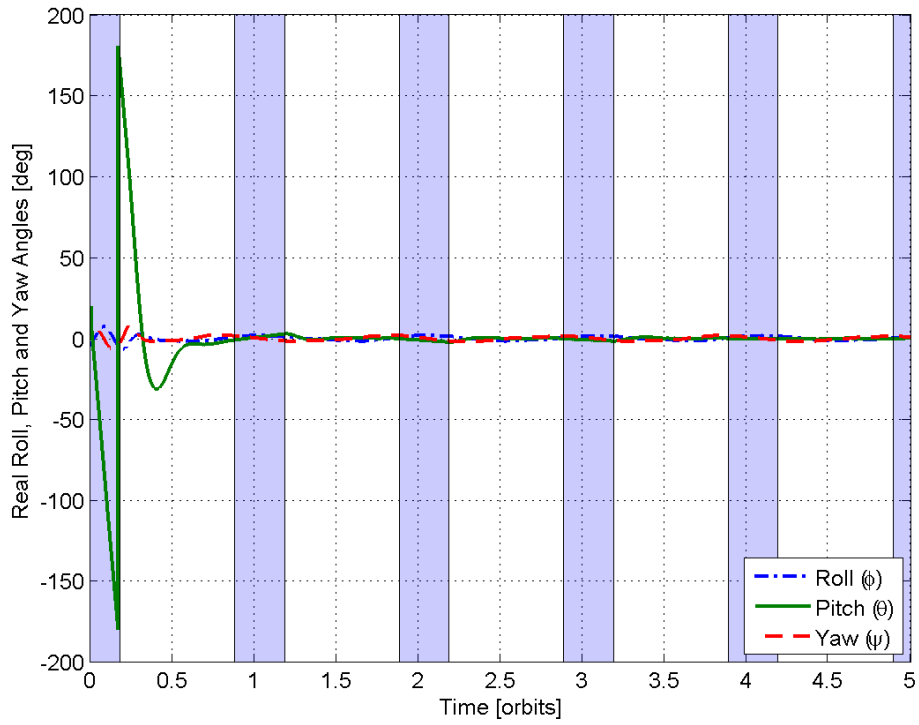
Figure 5.6 – RPY Angles of the Base Reaction Wheel Scenario - $K_Y = 187$
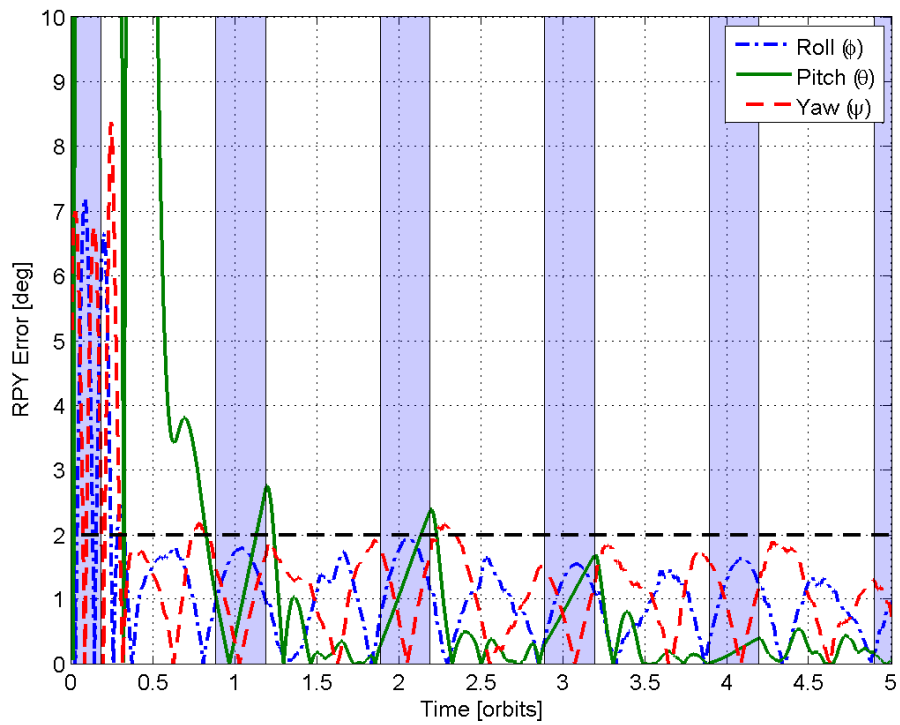
Figure 5.7 – Absolute RPY Error of the Base Reaction Wheel Scenario - $K_Y = 187$

As can be seen from figures 5.6 and 5.7, the roll, pitch, and yaw angles are initially controlled to within 2° of the reference angle in 0.83 orbits (5028 s). During the eclipse periods, the pitch angle slowly drifts away from the pitch reference angle. This does not have a great effect, since the angle is swiftly corrected once the satellite exits its eclipse period. The absolute RPY error remains within the 2° margin when the satellite is exposed to the sun.

The root mean square error, with gain $K_Y = 187$, after a transition period of n orbits are listed in table 5.6.

Table 5.6 – RPY RMS Errors of the Base Reaction Wheel Scenario - $K_Y = 187$

Transition Period [orbits]	RMSE [°]
0	15.23
1	1.05
2	0.96
3	0.97
4	0.95

When comparing these RMS errors to the scenario without the reaction wheel, table 5.2, it already becomes apparent that the reaction wheel delivers a faster performance, decreasing the 2° settling time by more than two orbits. The results obtained from the simulation are listed in table 5.7.

Table 5.7 – Simulation Results of the Base Reaction Wheel Scenario - $K_Y = 187$

	With Noise		Without Noise	
Total Translated Distance	1.39	m	0.51	m
Total Magnetorquer On-Time	1937	s	1891	s
2° Settling Time	5028	s	4973	s
Control Torque	37.61	mNm		
Magnetic Torque	12.32	mNm		
Solar Sail Torque	7.46	mNm		
Reaction Wheel Torque	17.83	mNm		

The real ECI angular rates are shown in figure 5.8. When comparing the wheel momentum, figure 5.9 to the ECI angular rates, one can see that the wheel is spun in the opposite direction to lower the satellite's pitch rate.
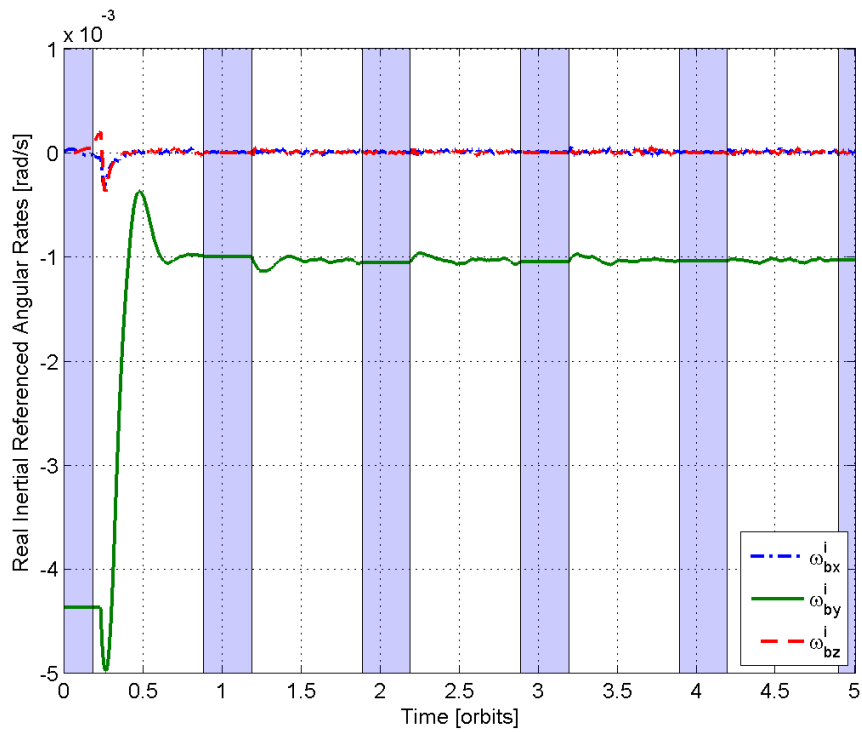
Figure 5.8 – Real ECI Angular Rates of the Base Reaction Wheel Scenario - $K_Y = 187$
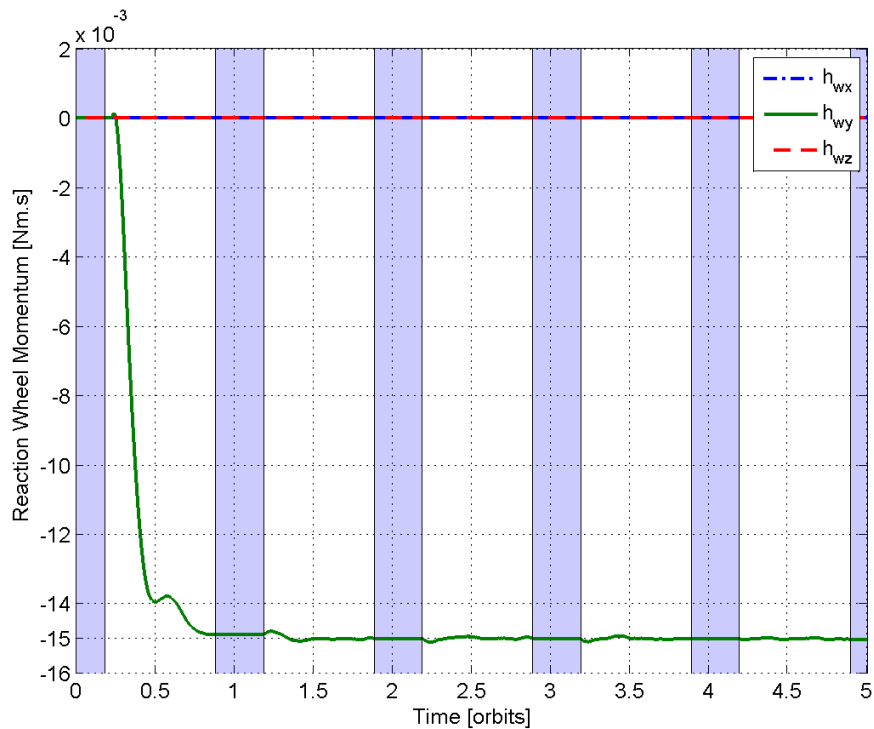
Figure 5.9 – Wheel Momentum of the Base Reaction Wheel Scenario - $K_Y = 187$

As can be seen from figure 5.9, the nominal wheel momentum was only achieved after 1.34 orbits (8127 s). Although this is a relatively slow change, the RPY angles are controlled a lot faster than the base scenario without the reaction wheel.

The distance travelled has also decreased by 21.87 cm, while the magnetorquer on-time has increased by 493 s. The resulting magnetic moments and solar sail XZ-translation are illustrated in figures 5.10 and 5.11.
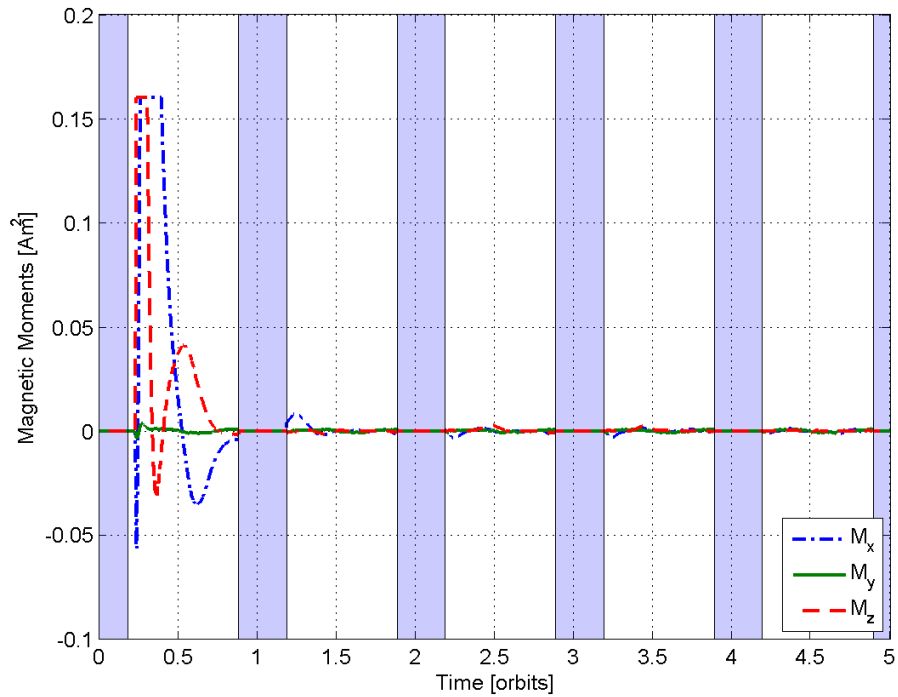
Figure 5.10 – Magnetic Controller Moments of the Base Reaction Wheel Scenario - $K_Y = 187$
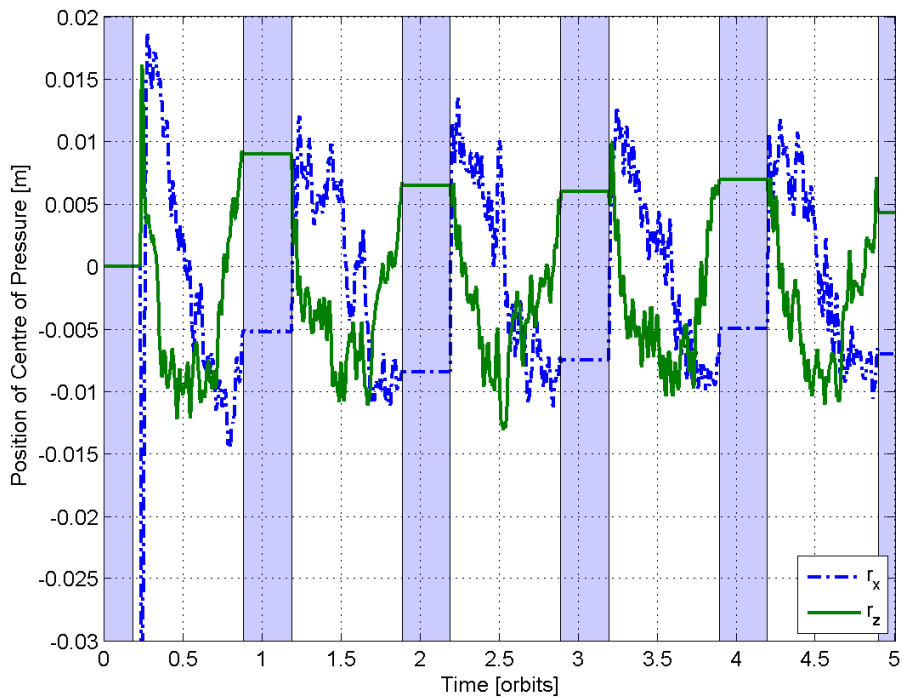
Figure 5.11 – Motor Translation of the Base Reaction Wheel Scenario - $K_Y = 187$

5.2.3 Base Scenario Comparison

To gauge the feasibility of the reaction wheel controller, the two base scenarios described in sections 5.2.1 and 5.2.2 were compared. This comparison is summarised in table 5.8. The comments column indicates the percentage change that is apparent regarding the reaction wheel scenario. The RMS RPY error was calculated after a transition period of one orbit.

Table 5.8 – Comparison of the Base Scenarios

		No Wheel	Wheel	Comments
Gain K_Y			187	
2° Settling Time	[s]	20922	5028	**75**% Decrease
Magnetorquer On-Time	[s]	1444	1937	34% Increase
Solar Sail Translation	[m]	1.60	1.39	**13**% Decrease
Control Torque	[mNm]	16.44	37.61	129% Increase
RMS RPY Error	[°]	7.36	1.05	**86**% Decrease

The settling time is a lot faster for the reaction wheel scenario thereby reducing the RMS RPY error. The reaction wheel scenario has a larger control torque value, mainly due to the additional reaction wheel torques, therefore more control effort is required. The composition of the control torque value is illustrated in table 5.9.

Table 5.9 – Composition of Base Scenario Control Torque

		No Wheel	Wheel	Comments
Control Torque	[mNm]	16.44	37.61	129% Increase
Magnetic Torque	[mNm]	8.64	12.32	43% Increase
Solar Sail Torque	[mNm]	7.80	7.46	4% Decrease
Reaction Wheel Torque	[mNm]	-	17.83	

It was concluded from these results, that the reaction wheel scenario was feasible. Further adjustments to the controller gains were needed to find the best case reaction wheel scenario. In the next section, various magnetic controller derivative gains K_Y are investigated to obtain the best performance while minimising the control effort associated with the response.

5.3   Improved Reaction Wheel Scenarios

To increase the speed of change regarding the reaction wheel momentum, it is necessary to increase the magnetic controller derivative gain, K_Y. In this section the gain has been increased to obtain a fast response which served as an upper limit in the gain selection process. After this, a best case scenario is investigated to maximise performance while at the same time minimising the control effort required. In conclusion, the differences between the scenarios are summarised and compared.

5.3.1   Fast Momentum Change Simulation

The limit for the speed of the momentum change was chosen in order to achieve a momentum dump in 0.5 orbits (3023 s), that is to say that the speed had to be increased to realise a change in momentum from one momentum value to another in less than 0.5 orbits.

After running extensive simulations, it was found that a derivative gain $K_Y = 798$ was required to achieve a wheel momentum change within 0.5 orbits. The reaction wheel gains $K_D = 4.76\text{E-}3$, and $K_P = 2.26\text{E-}5$ were left unchanged. The RPY angles for this scenario are illustrated in figure 5.12, with the absolute error in figure 5.13.
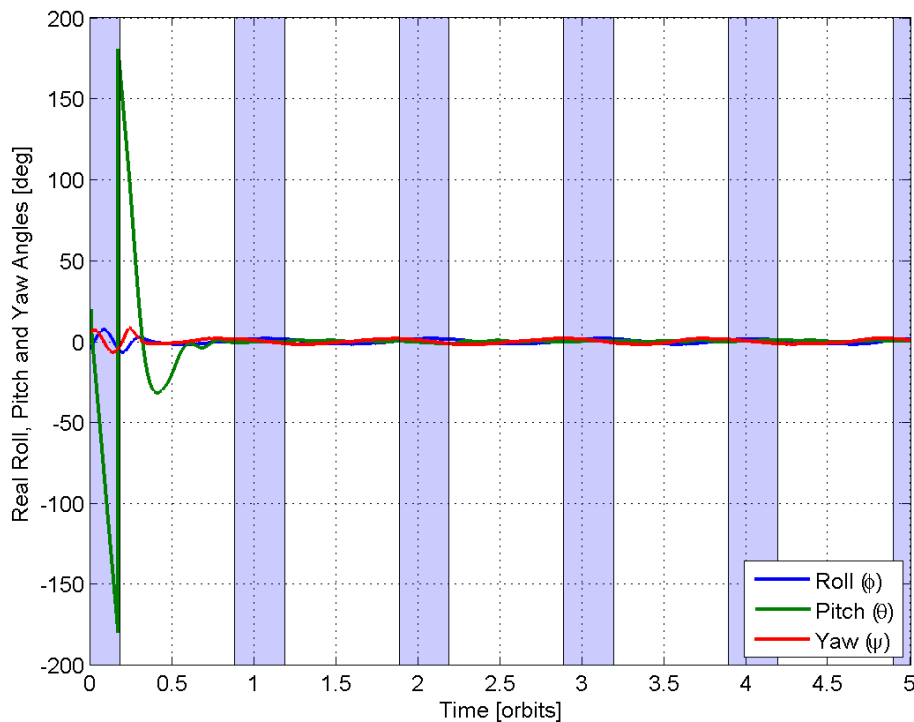
Figure 5.12 – RPY Angles of the Reaction Wheel Scenario - $K_Y = 798$
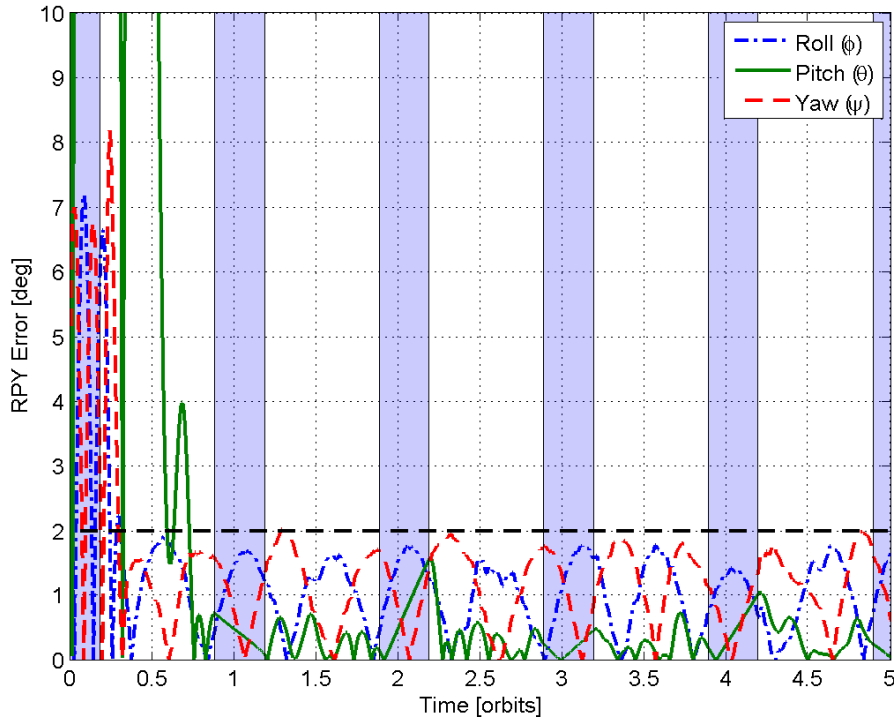
Figure 5.13 – Absolute RPY Error of the Reaction Wheel Scenario - $K_Y = 798$

As can be seen from figures 5.12 and 5.13, the roll, pitch, and yaw angles are initially controlled to within 2° of the reference angle in 0.73 orbits (4414 s). Except for this change in the 2° settling time, the response remains virtually the same as that of the base reaction wheel scenario, figures 5.6 and 5.7.

The root mean square error, with gain $K_Y = 798$, after a transition period of n orbits are listed in table 5.10.

Table 5.10 – RPY RMS Errors of the Base Reaction Wheel Scenario - $K_Y = 798$

Transition Period [orbits]	RMSE [°]
0	15.27
1	1.06
2	1.06
3	1.03
4	1.06

The RMS error remains within the 2° boundary, but because of the increased magnetic torquer gain, the control becomes more agressive leading to a slight ($\approx 0.1°$) increase in the RMS error in comparison to the base reaction wheel scenario.

The results that were obtained during the simulation are listed in table 5.11.

Table 5.11 – Simulation Results of the Reaction Wheel Scenario - $K_Y = 798$

	With Noise		Without Noise	
Total Translated Distance	1.40	m	0.51	m
Total Magnetorquer On-Time	2646	s	2403	s
2° Settling Time	4414	s	4384	s
Control Torque	43.73	mNm		
Magnetic Torque	15.67	mNm		
Solar Sail Torque	7.81	mNm		
Reaction Wheel Torque	20.25	mNm		

The real ECI angular rates are shown in figure 5.14. The reference wheel momentum is achieved, and maintained, in less than half an orbit (3023 s), as illustrated in figure 5.15.
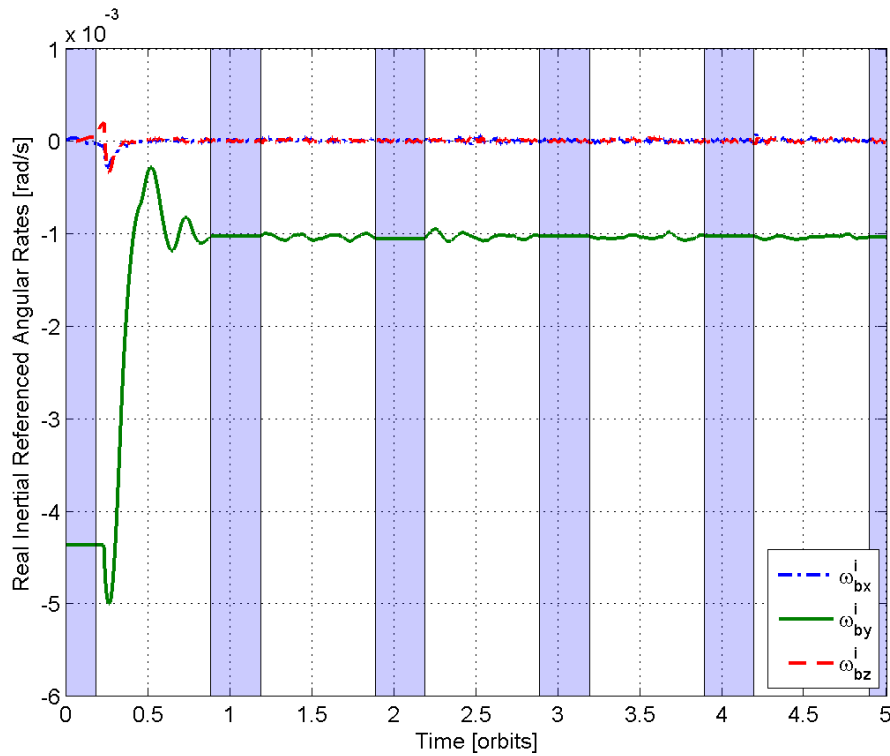
Figure 5.14 – Real ECI Angular Rates of the Reaction Wheel Scenario - $K_Y = 798$
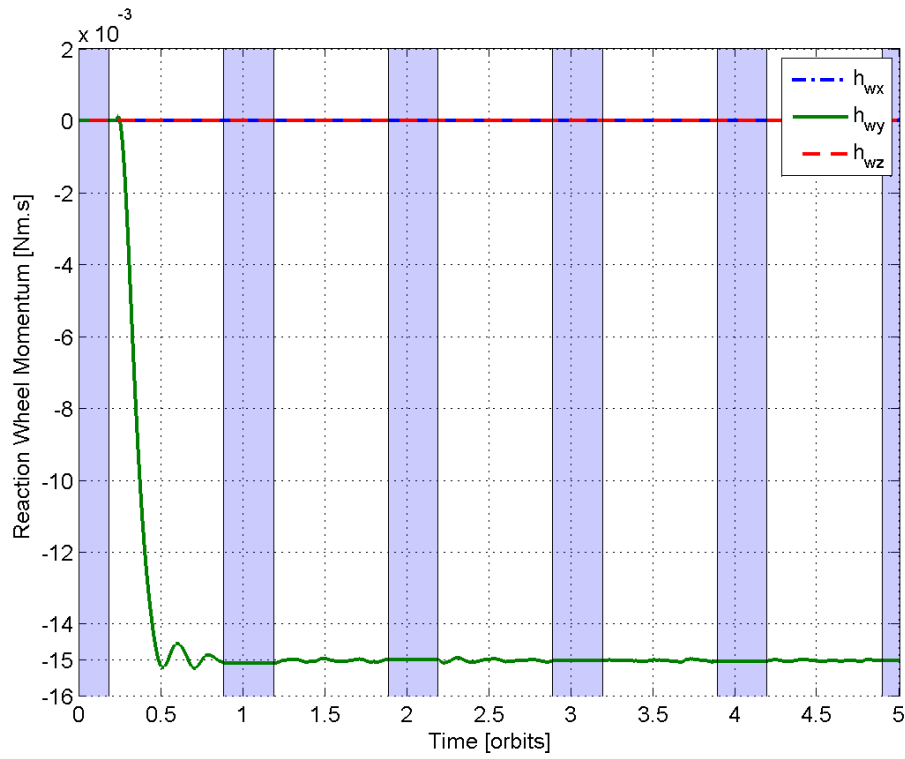
Figure 5.15 – Wheel Momentum of the Reaction Wheel Scenario - $K_Y = 798$

The resulting magnetic moments and solar sail XZ-translation are illustrated in figures 5.16 and 5.17.
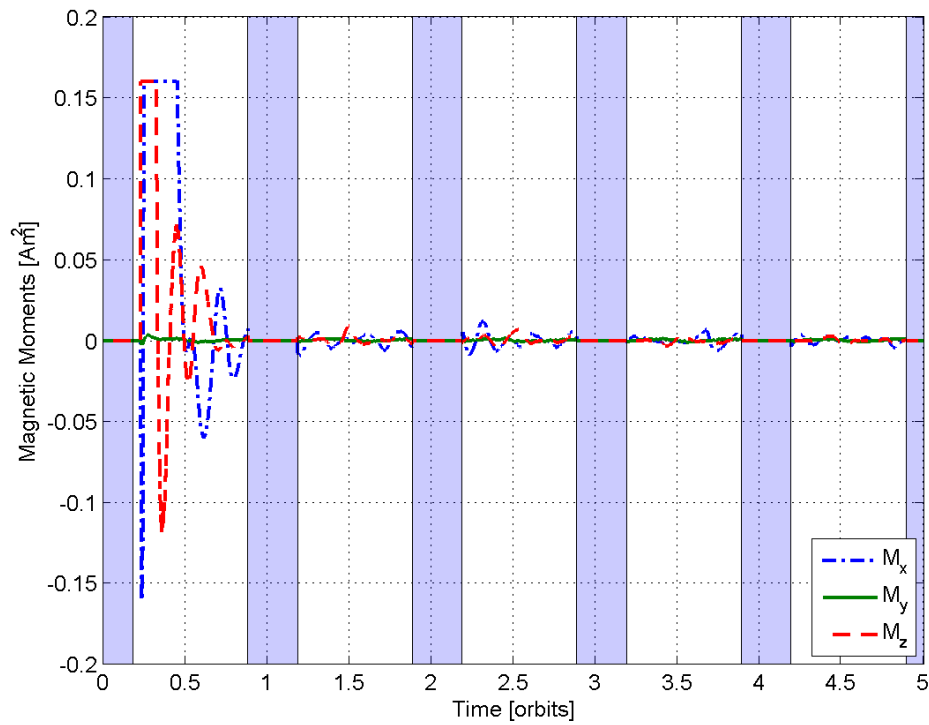
Figure 5.16 – Magnetic Controller Torques of the Reaction Wheel Scenario - $K_Y = 798$
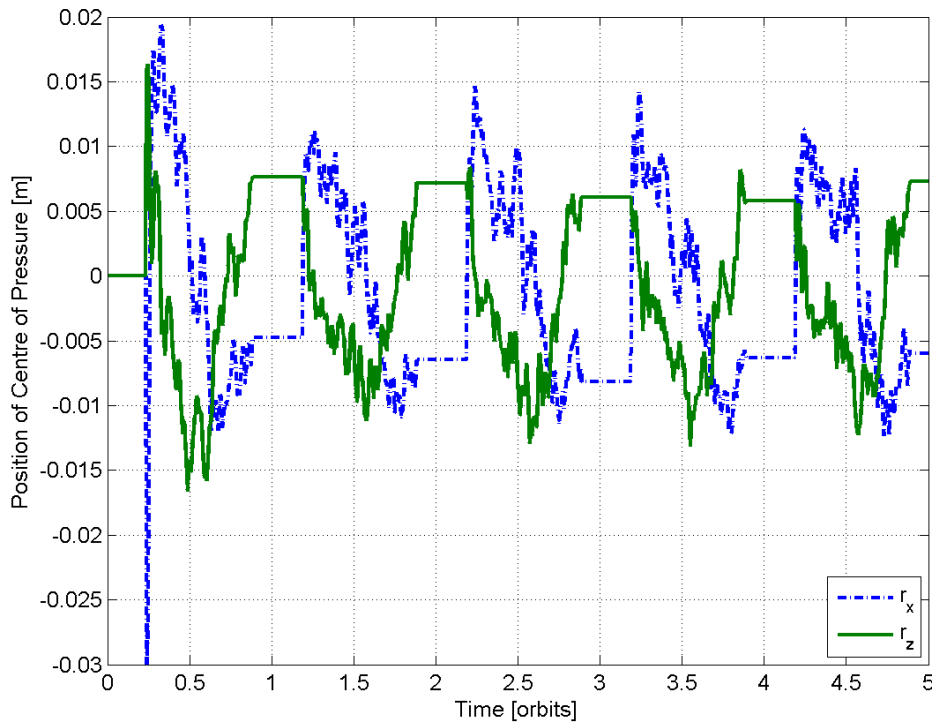
Figure 5.17 – Motor Translation of the Reaction Wheel Scenario - $K_Y = 798$

When comparing this simulation to the base scenario, with gain $K_Y = 187$, we see that the RMS RPY error and distance travelled changed very little, while the magnetorquer on-time increased by 709 s. This increase was expected, and as a result the reference reaction wheel momentum was achieved in 0.5 orbits.

5.3.2   Optimal Momentum Change Simulation

When comparing the 0.5 orbit dump simulation to the base reaction wheel scenario, we see that a 427% increase in magnetic controller gain, K_Y is required to achieve the target wheel momentum change speed. Even with this increase, the wheel momentum speed has only increased by 168% while the required control effort has increased by 16.27%. It was therefore apparent that further investigation was required to obtain a middle-way solution in which the performance would be maximised while the control effort would be minimised.

For this solution, the goal was to investigate the effects when changing the K_Y gain in order to achieve a momentum dump in less than 1 orbit. Since no active attitude control is performed during the eclipse period, it was necessary to adjust the K_Y gain to allow the reaction wheel to reach the reference momentum before the satellite enters into eclipse.

It was found that a derivative gain $K_Y = 200$ provided a wheel momentum change in 0.87 orbits (5243 s), just before the satellite enters into eclipse. The reaction wheel

gains $K_D = 4.76\text{E-}3$, and $K_P = 2.26\text{E-}5$ were again left unchanged. The RPY angles for this scenario are illustrated in figure 5.18, with the absolute error in figure 5.19.
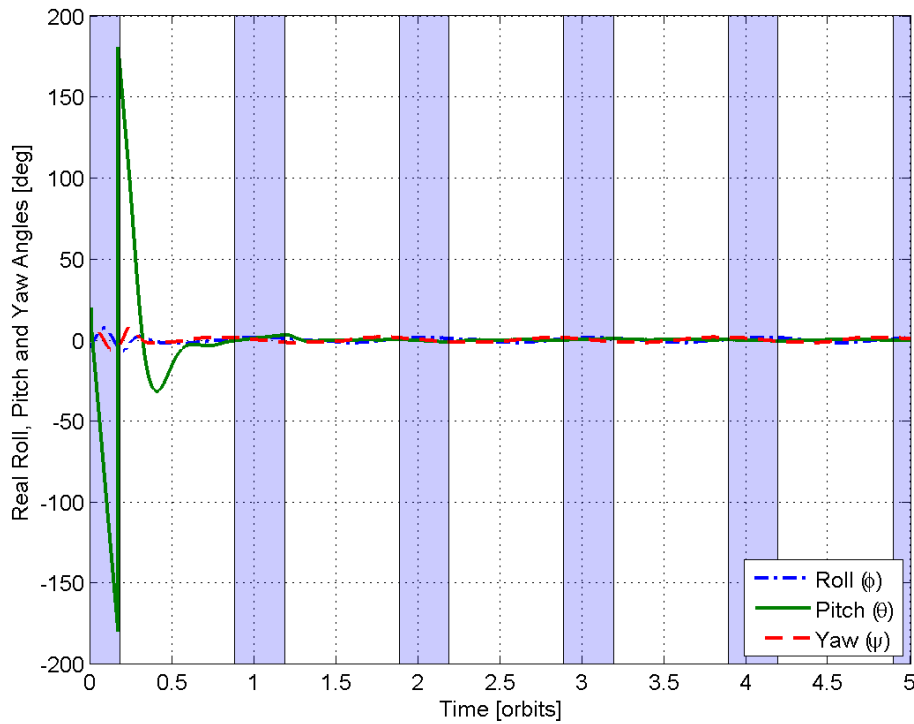
Figure 5.18 – RPY Angles of the Reaction Wheel Scenario - $K_Y = 200$
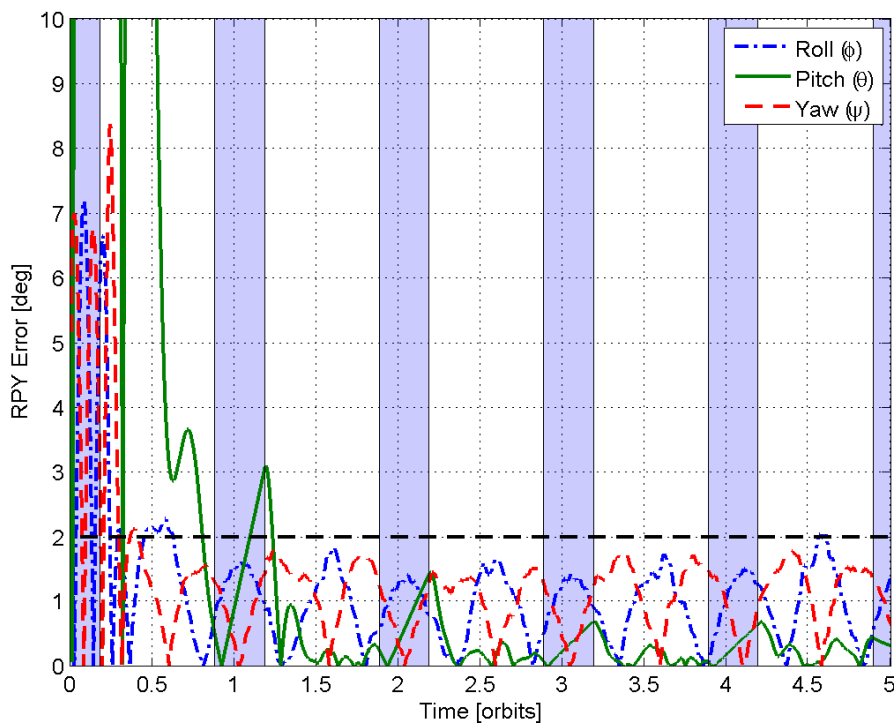
Figure 5.19 – Absolute RPY Error of the Reaction Wheel Scenario - $K_Y = 200$

As illustrated in figures 5.18 and 5.19, the roll, pitch, and yaw angles are initially controlled to within 2° of the reference angle in 0.81 orbits (4898 s). This change was expected from analysing the previous reaction wheel simulations, sections 5.2.2 and 5.3.1.

The root mean square error, with gain $K_Y = 200$, after a transition period of n orbits are listed in table 5.12.

Table 5.12 – RPY RMS Errors of the Base Reaction Wheel Scenario - $K_Y = 200$

Transition Period [orbits]	RMSE [°]
0	15.23
1	1.01
2	0.96
3	0.95
4	0.96

As can be seen from the RMS error, there is a minimum deviance from the reference RPY angles. The initial RMS error is solely attributed to the effect of the initial angular rates during the eclipse period. The results obtained from the simulation are listed in table 5.13.

Table 5.13 – Simulation Results of the Reaction Wheel Scenario - $K_Y = 200$

	With Noise		Without Noise	
Total Translated Distance	1.40	m	0.54	m
Total Magnetorquer On-Time	1950	s	1901	s
2° Settling Time	4898	s	4934	s
Control Torque	37.44	mNm		
Magnetic Torque	12.32	mNm		
Solar Sail Torque	7.54	mNm		
Reaction Wheel Torque	17.58	mNm		

The real ECI angular rates are shown in figure 5.20. The reference wheel momentum is achieved, and maintained, in 0.87 orbits (5243 s), as illustrated in figure 5.21.
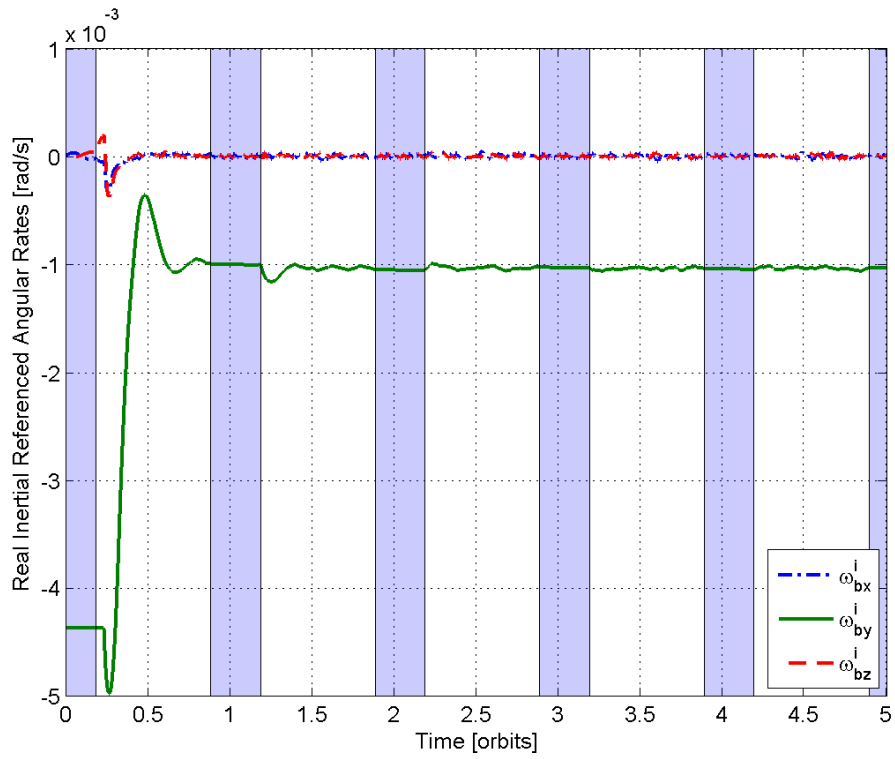
Figure 5.20 – Real ECI Angular Rates of the Reaction Wheel Scenario - $K_Y = 200$
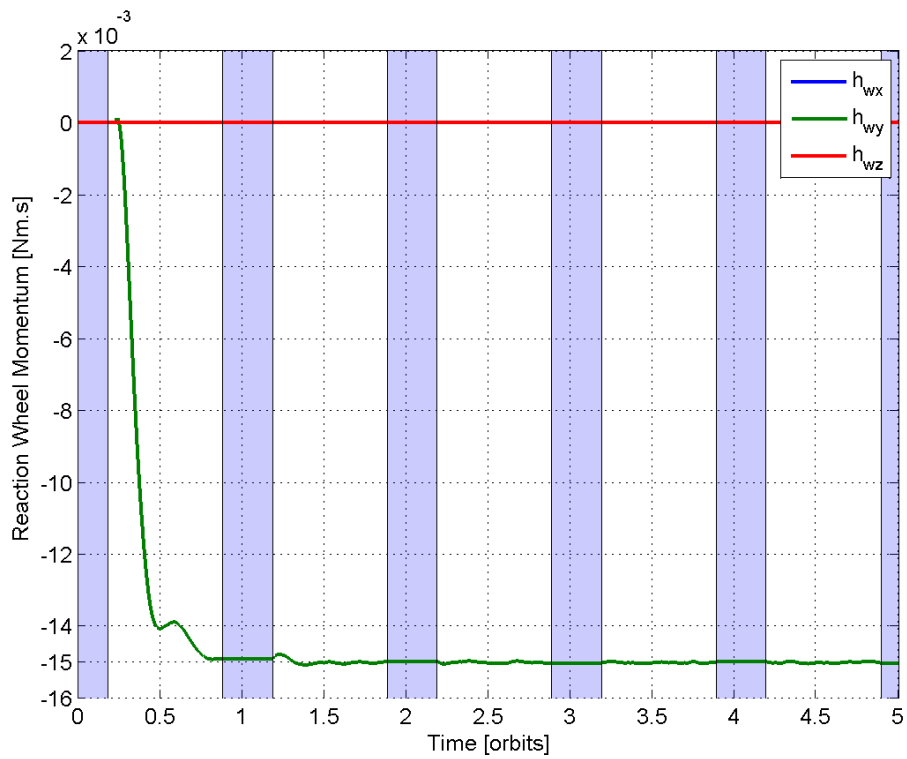
Figure 5.21 – Wheel Momentum of the Reaction Wheel Scenario - $K_Y = 200$

The resulting magnetic moments and solar sail XZ-translation are illustrated in figures 5.22 and 5.23.
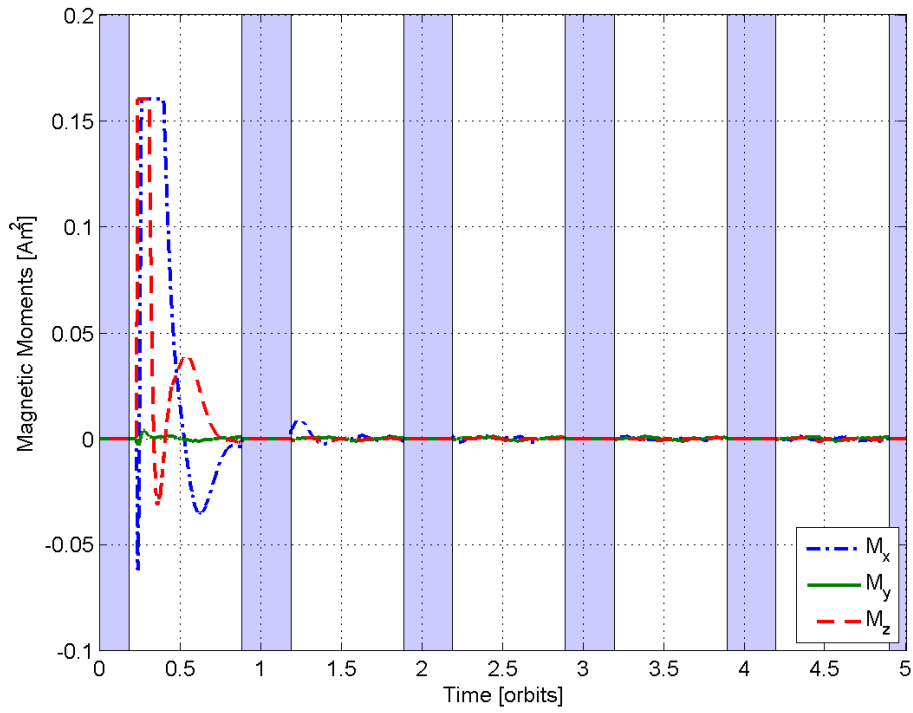
Figure 5.22 – Magnetic Controller Moments of the Reaction Wheel Scenario - $K_Y = 200$
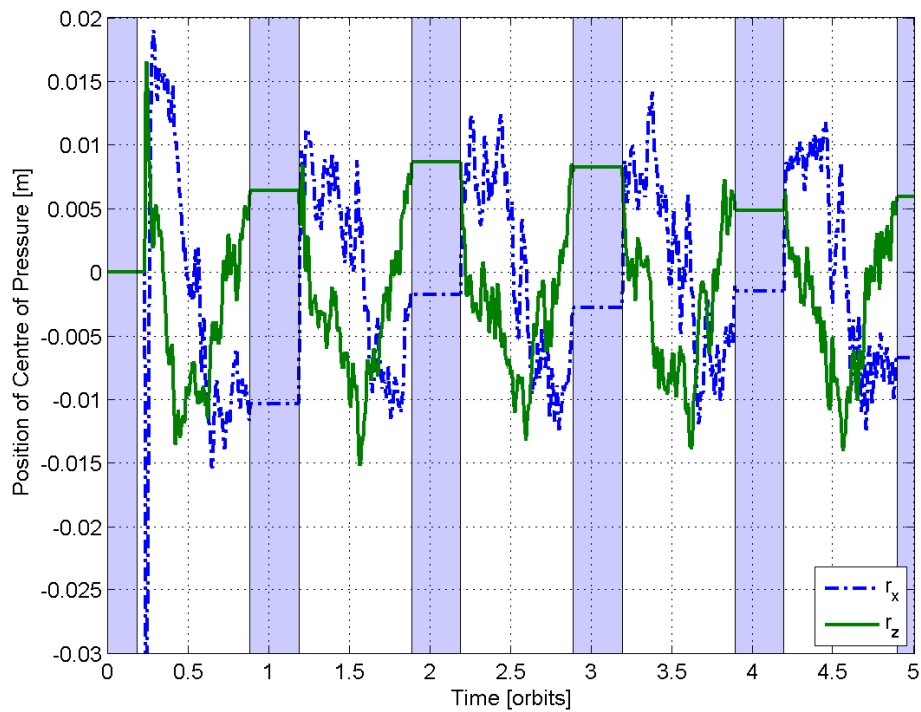
Figure 5.23 – Motor Translation of the Reaction Wheel Scenario - $K_Y = 200$

5.3.3 Reaction Wheel Comparisons

The different reaction wheel scenarios that were described in section 5.3 are compared in table 5.14. The RMS RPY errors were calculated after a transition period of one orbit and the wheel settling time is the time taken to reach the reference reaction wheel momentum from initial conditions.

Table 5.14 – Comparison of the Reaction Wheel Scenarios

		Base Scenario	Fast Change	Optimal Scenario
Gain K_Y		187	798	200
2° Settling Time	[s]	5028	4414	4898
Magnetorquer On-Time	[s]	1937	2646	1950
Solar Sail Translation	[m]	1.39	1.40	1.40
Control Torque	[mNm]	37.61	43.73	37.44
RMS RPY Error	[°]	1.05	1.06	1.01
Wheel Settling Time	[s]	8127	3023	5243

It was already illustrated in section 5.2.3 that the reaction wheel scenarios have a much faster settling time and lower RMS RPY errors when compared to the scenario without a reaction wheel. It is also apparent from table 5.14 that the solar sail translation does not differ that much for the different reaction wheel scenarios. These criteria were therefore deemed less important when comparing the different reaction wheel scenarios with each other. The composition of the control torque is illustrated in table 5.15.

Table 5.15 – Composition of Reaction Wheel Scenario Control Torque

Gain K_Y		187	798	200
Control Torque	[mNm]	37.61	43.73	37.44
Magnetic Torque	[mNm]	12.32	15.67	12.32
Solar Sail Torque	[mNm]	7.46	7.81	7.54
Reaction Wheel Torque	[mNm]	17.83	20.25	17.58

The main differences between the various reaction wheel scenarios are apparent when comparing the magnetorquer on-time; control torques and reaction wheel settling times. These three criteria are interconnected with the chosen control gain, for example a larger gain will extend the magnetorquer on-time; increase the control torques and decrease the reaction wheel settling time.

As previously mentioned, the base reaction wheel scenario has a relatively slow wheel momentum change. The 0.5 orbit dump scenario is faster but at the cost of greatly increasing the control gains. After extensive testing, an optimal scenario with gain $K_Y = 200$, incorporating the lower control effort and faster settling times of the two extreme scenarios, was identified.

This optimal case represents the best reaction wheel scenario and is compared to the base scenario without a reaction wheel in the next section.

5.4 Discussion

In chapter 5, two basic control systems were investigated to control the attitude of the cube satellite. The first system that was used for comparison purposes was previously investigated and optimised, [48]. The second system investigated, used a reaction wheel to control the pitch component of the satellite's attitude, while the wheel speed was controlled with a magnetorquer.

The best case reaction wheel scenario has been identified and is compared to the base scenario without the reaction wheel in table 5.16.

Table 5.16 – Final Scenario Comparison

		No Wheel	Wheel	Comments
Gain K_Y		-	200	
2° Settling Time	[s]	20922	4898	**76**% Decrease
Magnetorquer On-Time	[s]	1444	1950	35% Increase
Solar Sail Translation	[m]	1.60	1.40	**13**% Decrease
Control Torque	[mNm]	16.44	37.44	128% Increase
RMS RPY Error	[°]	7.36	1.01	**86**% Decrease
Wheel Settling Time	[s]	-	5243	

It is immediately apparent that the reaction wheel scenario has better performance characteristics. Using a reaction wheel for the pitch control reduces the magnetic torquer on-time. At the same time the magnetic torquer is used to maintain the reference reaction wheel momentum, therefore the on-time is interconnected to the magnitude of the reference wheel momentum. Table 5.17 illustrates the composition of the control torque.

Table 5.17 – Composition of Control Torque

		No Wheel	Wheel	Comments
Control Torque	[mNm]	16.44	37.44	128% Increase
Magnetic Torque	[mNm]	8.64	12.32	43% Increase
Solar Sail Torque	[mNm]	7.80	7.54	3% Decrease
Reaction Wheel Torque	[mNm]	-	17.58	

As can be seen from table 5.17, the increase in the control torque is mainly attributed to the addition of the reaction wheel torque whereas the increase in the magnetic torque has a minimal effect.

The efficiency of the magnetorquers are limited by the magnitude of the earth's magnetic field, therefore the reaction wheel tends to outperform the magnetorquers and is thus the best choice even at the price of the added control effort.

Chapter 6

Conclusion

This chapter concludes the thesis with a concise summary of the objectives that have been achieved. First the computer simulations are evaluated, after which the mechanical structures and electronic hardware are commented on. This chapter ends with further recommendations based on these observations and results.

6.1 Computer Simulation Evaluation

It has been proven that active 3-axis attitude control for a CubeSat is possible by using three magnetorquer rods, each producing a maximum magnetic moment of 0.16 Am^2, and a movable 25 m^2 solar sail.

In an attempt to reduce the time required for this attitude control, a y-axis reaction wheel has also been simulated. As discussed in chapter 5, the necessary attitude control was achieved with a 76% decrease in the 2° settling time when compared to the initial solar sail simulation.

The implementation of the reaction wheel also provides redundancy to the satellite control system. In the event that the reaction wheel fails, it is only necessary to adjust the magnetorquer control algorithm to retain 3-axis attitude control using the remaining torquer rods and the solar sail controller.

6.2 Structural and Hardware Evaluation

Two translation stages were designed, manufactured and tested. The second design being preferred due to the increased stability and decreased height, as mentioned in section 4.1. Limitations on the accuracy of the in-house manufacturing resulted in a certain amount of play on the support beams, which can cause the translation stage to get stuck. More precise manufacturing might alleviate this problem. If not, additional supports can be added or a ball-bearing design can be investigated, although the latter

may be subject to the effects of outgassing.

A prototype magnetorquer rod has also been designed with a length of 60 mm and diameter of 5 mm. This design allowed for the required magnetic moment of 0.2 Am^2 at 100 mA. By increasing the diameter of the rod, the required current can be reduced however the overall diameter would then exceed the maximum 8 mm design requirement. The solution would be to increase the length as well as the diameter of the torquer rod, although to minimise the interference between the torquer rods the configuration within the CubeSat must be considered. In addition the remnant magnetic moment would increase, while the implemented moment remains limited at 0.16 Am^2 (80% of 0.2 Am^2).

6.2.1 Commercial-Off-the-Shelf Components

The *AM0820* stepper motors from *Faulhaber* are also available in vacuum graded versions with low outgassing characteristics. For the prototype, non-vacuum motors were implemented with the *Delrin* pinion gear fixed to the motor's metal shaft using super glue. Although this has proved to be adequate, space grade epoxy is preferred[1] when joining the metal and *Delrin* materials.

The speed at which the stepper motors were implemented can also be increased to 1500 RPM by using a 1 ms ISR. This would allow the coverage of the full 60 mm range within the 10 s sampling period. This increase in speed is not necessary because of the slow control which is achieved with the solar sail and might only overtax the microprocessor. In addition, the motor only produces 0.4 mNm of torque at 1500 RPM providing a force of 9.85 N which can have an effect on the capability of the motors depending on the final weight of the translation stage load.

6.2.2 Hardware-in-the-Loop Simulation

The hardware-in-the-loop simulation served to illustrate the practical performance that the control algorithms have on the hardware components. Although the magnetometer could not be fully tested, due to the "constant" magnetic field, its implementation with the actuators were tested. It was also possible to view the magnetorquer on-times, using LEDs, while the stepper motors were being driven at the same time.

6.3   Further Recommendations

The mechanical structure can be improved as follows.

- The precise machining of the structural components would reduce the risk of the translation stage getting stuck.

---

[1] A press-fit solution would however be best.

- The centre of the racks must be precisely determined and marked in order to zero the stepper motors using optical sensors.

- The size and weight of the structure has already been sufficiently reduced, but can be reduced even further by restricting the range of the rack to the 60 mm range and altering the structure for this range.

The following considerations must be taken into account for improvements in the electronic drive circuitry.

- A 16-bit ADC can be implemented to achieve the maximum accuracy that is possible with the current magnetometer.

- The usage of a PWM signal with the stepper motors can increase power efficiency.

Furthermore, if this prototype is chosen to be implemented and launched it is recommended to apply epoxy to all the screws to fix them in place during vibration tests. The magnetorquers should also be placed in an acceptable L or T configuration to limit the interference between these torquer rods.

Appendix A

Delrin Gear Information

Polyoxymethylene is an engineering plastic that has been commercialised by *DuPont* under the name *Delrin*. This is a hard, low friction plastic that is often used as a substitute to metal. These properties and more can be found on the *DuPont* website or in the *Delrin* datasheet, [57].

Because of these properties it was decided to use *Delrin* material for the rack and pinion system. Various international gear manufacturers, listed in table A.1 were investigated for a *Delrin* rack and pinion that would be suitable for the chosen stepper motor, Appendix C.

Table A.1 – Gear Manufacturers

Manufacturer	Website
Davall Gears	www.davall.co.uk
Halifax Rack & Screw	www.hrs-ccl.co.uk
HPC Gears	www.hpcgears.com
Llewellin's Gears	www.llewellins.co.uk
Nordex Incorporated	nordex.com
Ondrives Precision Manufacturing	www.ondrives.com/index.php
T.E.A. Machine Components	www.teausa.net/index.aspx
WMH Transmissions Limited	www.wmh-trans.co.uk

HPC Gears was chosen since they had a spur gear that could tightly fit onto the stepper motor shaft. They supplied both the racks and spur gears with identical pitch, thus ensuring that the gears meshed together satisfactorily. The *ZPG0.4-13* spur gear was chosen with the *ZR0.4-400* rack. The 400 mm long rack was further machined into pieces that were 100 mm in length for use within the CubeSat.

Appendix B

Mechanical Structures

Autodesk Inventor 2009 is the computer aided design software that was used to design the translation stages for the solar sail panel. Figure B.1 illustrates the initial, volume-based, translation stage design.
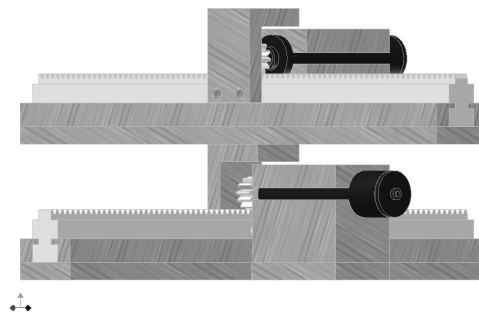
Figure B.1 – Volume Based Structure

Due to the concerns regarding the overall stability of the structure, the translation stage was redesigned in an attempt to increase the stability and decrease the height. The stability-based design is illustrated in figure B.2 and discussed below.
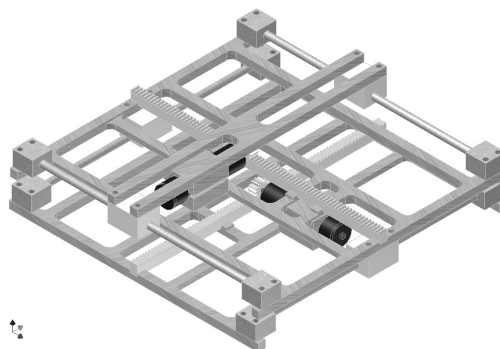
Figure B.2 – Stability Based Structure

The weight and rigidity of the translation stage had to be taken into account during the manufacturing of these structures. To minimise the structure's weight, aluminium was used for the structural plates as well as the end stops. The support beams, however, were manufactured from stainless steel which has a higher density and can therefore support more weight without bending.

The stainless steel rods, obtained from *Pure Steel Products*, are electro-polished to provide a low friction surface upon which the runners move. Electro-polishing is described as the controlled electrochemical removal of surface metal thereby providing a smooth finish, [58].

To exploit the low friction properties of these rods, the runners that move along the support beams, as well as the gears and racks, were made from *Delrin*. Furthermore, the corners of the structural plates were rounded to allow the effective distribution of any forces imparted upon the structure due to vibrations.

The stability of this structure was found to be better than the volume-based design. In addition, because the rack remains stationary, it was possible to decrease the height of the rack and motor supports thus decreasing the overall height and weight of the structure, as discussed in section 4.1.

Appendix C

Stepper Motor Information

A variety of motors were investigated from various manufacturers, listed in table C.1. Local and international suppliers/manufacturers were compared, but because of the size specification it was apparent that the motors would have to be ordered from an international manufacturer specialising in smaller motors.

Table C.1 – Motor Manufacturers

Manufacturer	Website
FAULHABER	www.faulhaber.com
Lin Engineering	www.linengineering.com
New Scale Technologies	www.newscaletech.com
Physik Instrumente	www.physikinstrumente.com
Phytron Inc.	www.phytron.com
Portescap	www.portescap.com

Different options were considered including translation stages and linear motors. The *AM0820* stepper motor from *FAULHABER* was chosen because of its accuracy, weight, and size advantages in comparison with the alternatives. An extract of the datasheets for the stepper motor as well as its planetary gearhead are illustrated in figures C.1 and C.2

PRECI*step*

Stepper Motors   0,65 mNm
Two phase, 20 steps per revolution

AM0820-ww-ee

ww =		V-3-18		V-5-56		A-0,225-7		Drive mode
		Voltage	Current	Voltage	Current	Voltage	Current	
1	Nominal voltage	3	–	5	–	2	–	V DC
2	Nominal current per phase (both phases ON)	–	0,15	–	0,08	–	0,225	A
3	Phase resistance (at 20°C)		18		56		7,3	Ω
4	Phase inductance (1kHz)		5,2		16		2,1	mH
5	Back-EMF amplitude		0,8		1,4		0,5	V/k step/s
6	Holding torque [1] (at nominal current in both phases)	0,65						mNm
7	Holding torque [1] (at twice the nominal current)	1						mNm
8	Step angle (full step)	18						degree
9	Angular accuracy [2]	± 10						% of full step
10	Residual torque	0,06						mNm
11	Rotor inertia	2,75						$\cdot 10^{-9}$ kgm^2
12	Resonance frequency (at no load)	170						Hz
13	Electrical time constant	0,29						ms
14	Ambient temperature range	–30 ... +70						°C
15	Winding temperature tolerated, max.	130						°C
16	Thermal resistance winding-ambient air	76						°C/W
17	Thermal time constant	180						s
18	Shaft bearings	sintered bronze sleeves (standard)		ball bearings, preloaded (optional)				
19	Shaft load, max.:							
	– radial (3 mm from bearing)	0,3		3,0				N
	– axial	0,2		1,5				N
20	Shaft play, max.:							
	– radial (0,2N)	15		12				µm
	– axial (0,2N)	140		~0				µm
21	Isolation test voltage	200						V DC
22	Motor dimensions:							
	– diameter	8						mm
	– length	13,8						mm
	– shaft diameter	1,0						mm
23	Weight	3,3						g

[1] with bipolar driver
[2] 2 phases ON, balanced phase currents
[3] Curves measured with a load inertia of 10 $\cdot 10^{-9}$ kgm^2
[4] Testing the motor at lower supply voltages in current mode will result in a decrease in torque at higher speed, even with the same current setting

Voltage mode (V) [3]
Driver AD VL M1S

Current mode (A) [3] [4]
Driver AD CM M1S
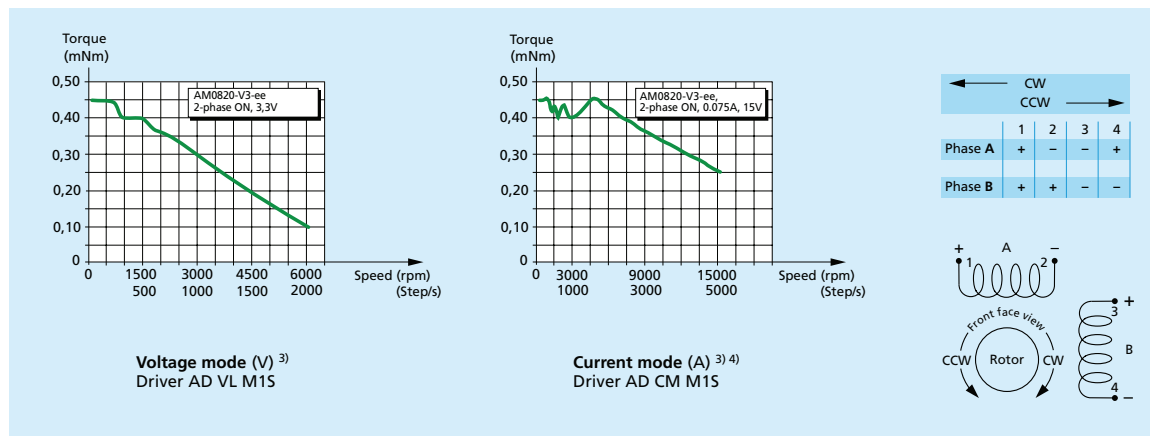
For additional technical information,
refer to the specific page "Notes on technical data"
Edition 2008 Oct. 23   Page 1/2

Specifications subject to change without notice.
www.precistep.com

Figure C.1 – Stepper Motor AM0820 Datasheet

Planetary Gearheads   60 mNm

For combination with
Stepper motor: AM0820

Series 08/1

	08/1	08/1 K
Housing material	steel	steel
Geartrain material	steel	steel
Recommended max. input speed for:		
– continuous operation	8000 rpm	8000 rpm
Backlash, at no-load	≤ 3°	≤ 3°
Bearings on output shaft	sintered sleeve bearings	preloaded ball bearings
Shaft load, max.		
– radial (4,5 mm from mounting face)	≤ 0,8 N	≤ 5 N
– axial	≤ 1 N	≤ 3 N
Shaft press fit force, max.	≤ 5 N	≤ 5 N
Shaft play (on bearing output):		
– radial	≤ 0,03 mm	≤ 0,02 mm
– axial	≤ 0,10 mm	≤ 0,05 mm
Operating temperature range	– 30° … + 100° C	– 30° … + 100° C

Specifications

reduction ratio	weight without motor	length without motor	length with motor AM0820	output torque continuous operation	output torque intermittent operation	direction of rotation (reversible)	efficiency
		L2	L1	M max.	M max.		
	g	mm	mm	mNm	mNm		%
4 :1	2,9	9,6	23,4	60	120	=	90
16 :1	3,8	12,3	26,1	60	120	=	80
64 :1	4,6	15,0	28,8	60	120	=	70
256 :1	5,4	17,7	31,5	60	120	=	60
1 024 :1	6,3	20,4	34,2	60	120	=	55
4 096 :1	7,1	23,1	36,9	60	120	=	48

ø8 (AM0820)   ø8 $_{-0,05}^{0}$ ø4 $_{+0,004}^{+0,012}$ ø1,5 $_{-0,010}^{0}$ ø4 $_{-0,008}^{0}$

1,3 $_{-0,03}^{0}$

3

3,93 ±0,2

1

L2 ±0,25

L1 ±0,5

5,90 ±0,2

4,15 ±0,2

08/1   **08/1 K**

Specifications subject to change without notice

Page 1/1

www.precistep.com

Edition 01.01.08
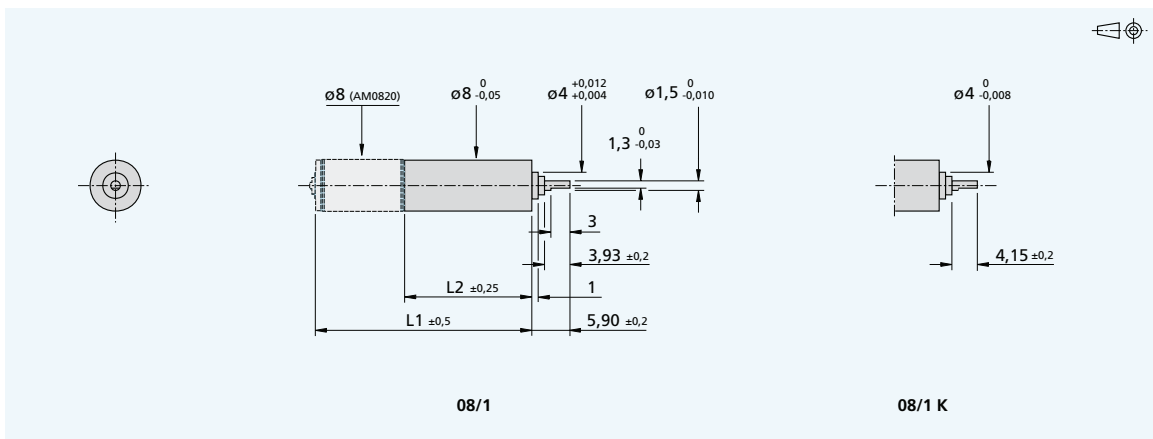
Figure C.2 – Planetary Gearhead 08/1 Datasheet

113

Appendix D

Magnetometer Information

The *HMC1053* anisotropic magneto-resistive sensor from *Honeywell* that was implemented has a set/reset function which can be used to cancel any electronic offsets that are applicable to the measurements. The datasheet, as well as the application notes listed in table D.1, are available at *www.magneticsensors.com/datasheets.html#datasheets*.

Table D.1 – Magnetic Sensor Application Notes

Note	Title
AN211	Applications of Magnetic Position Sensors
AN212	Handling Sensor Bridge Offset
AN213	Set/Reset Function for Magnetic Sensors
AN215	Cross Axis Effect for AMR Magnetic Sensors
AN216	Mounting Tips for LCC Magnetic Sensors

By using the set/reset function, the polarity of the magnetic field sensor output can be reversed while the electronic offsets remain the same. This results in $V_{set} = V^+ + V_{offset}$ and $V_{reset} = V^- + V_{offset}$ as illustrated in figure D.1 which was adapted from *AN212*.
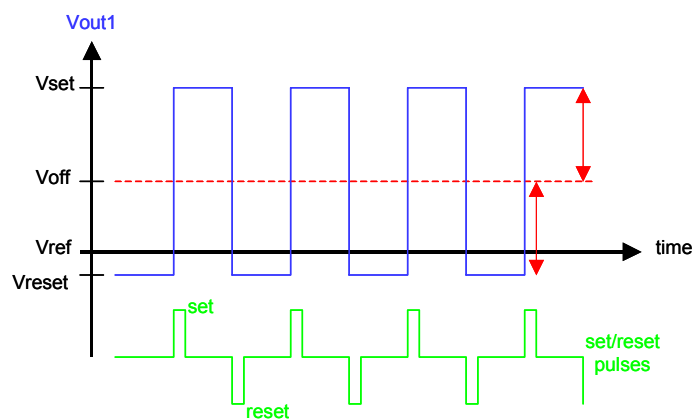
Figure D.1 – Set/Reset Functionality

By taking the average of the difference between the set and reset measurement voltages results in the cancellation of these offsets, as illustrated in equation D.0.1.

$$\frac{(V^+ + V_{offset}) - (V^- + V_{offset})}{2} = \frac{V^+ + V^-}{2} = V_{measurement} \qquad \text{(D.0.1)}$$

Bibliography

[1] A.K. Maini and V. Agrawal, *Satellite Technology: Principles and Applications.* John Wiley & Sons, Ltd., 2007.

[2] P. Fortescue, J. Stark and G. Swinerd, *Spacecraft Systems Engineering*, 3rd ed. John Wiley & Sons, Ltd., 2003.

[3] S. Garber and R. Launius. (2010, Aug. 19). *A Brief History of NASA*[Online]. Available: http://history.nasa.gov/factsheet.htm

[4] B. Feuerbacher and H. Stoewer, *Utilization of Space: Today and Tommorow.* Springer, 2006.

[5] O. Montenbruck and E. Gill, *Satellite Orbits: Models, Methods, and Applications.* Springer, 2000.

[6] Unknown. (2010, Aug. 23). *CubeSat Design Specification*[Online]. Available: http://www.cubesat.org/images/developers/cds_rev12.pdf

[7] L. David. (2010, Aug. 23). *CubeSats: Tiny Spacecraft, Huge Payoffs*[Online]. Available: http://www.space.com/businesstechnology/cube_sats_040908.html

[8] E.J. Overby, "Attitude Control for the Norwegian Student Satellite nCube," M.S. thesis, Norwegian Univ. of Sci. and Tech., Trondheim, Norway, 2004.

[9] S.S. Ose, "Attitude Determination for the Norwegian Student Satellite nCube," M.S. thesis, Norwegian Univ. of Sci. and Tech., Trondheim, Norway, 2004.

[10] K. Svartveit, "Attitude Determination of the NCUBE Satellite," M.S. thesis, Norwegian Univ. of Sci. and Tech., Trondheim, Norway, 2003.

[11] B.O. Sunde, "Attitude Determination for the Satellite nCubeII: Kalman Filter," M.S. thesis, Norwegian Univ. of Sci. and Tech., Trondheim, Norway, 2004.

[12] G. Bozovic, O. Scaglione, C. Koechli, M. Noca, and Y. Perriard, *SwissCube: Development of an Ultra-Light and Efficient Inertia Wheel for the Attitude Control and Stabilization of CubeSat Class Satellites*, 59th International Astronautical Congress, 2008, Glasgow, Scotland (IAC-08 B4.6)

[13] Unknown. (2010, Aug. 24). *SwissCube: The First Swiss Satellite*[Online]. Available: http://swisscube.epfl.ch/

[14] M. Iai, J. Kataoka and T. Shima, "A PDA-Controlled Pico-Satellite, Cute-1.7, and its Radiation Protection," *Proc. 18th Annual AIAA/USU Conference on Small Satellites*, Logan, Utah, 2004.

[15] Unknown. (2010, Aug. 24). *AMSAT - CubeSat Information*[Online]. Available: http://www.amsat.org/amsat-new/satellites/cubesats.php

[16] F.W. Taylor, *Elementary Climate Physics.* Oxford University Press, 2005.

[17] R. Schmitt, *Electromagnetics Explained.* Elsevier, 2002.

[18] J. Shipman, J.D. Wilson and A. Todd, *An Introduction to Physical Science,* 12th ed. Houghton Mifflin Company, 2009.

[19] R.P. Feynman, *QED: The Strange Theory of Light and Matter*. Princeton University Press, 1985.

[20] A. Luque and A. Hegedus, *Handbook of Photovoltaic Science and Engineering.* John Wiley & Sons, Ltd., 2003.

[21] A. Goetzberger and V.U. Hoffmann, *Photovoltaic Solar Energy Generation.* Springer, 2005.

[22] E.E. Nichols and G.F. Hull, "The Pressure Due to Radiation," *Astrophysical J.,* vol. 17, no. 5, pp. 26-50, 1903.

[23] W.H. Steyn, "Class Notes 2009", unpublished.

[24] J.R. Wertz and W.J. Larson, *Space Mission Analysis and Design,* 3rd ed. Microcosm Press, Kluwer Academic Publishers, 1999.

[25] C.R. McInnes, *Solar Sailing: Technology, Dynamics and Mission Applications.* Praxis Publishing Ltd., 1999.

[26] B. Wie, "Solar Sail Attitude Control and Dynamics, Parts 1 and 2," *J. Guidance, Control, and Dynamics,* vol. 27, no. 4, pp. 526-544, Aug. 2004.

[27] J.L. Wright, *Space Sailing.* Gordon and Breach Science Publishers, 1992.

[28] V. Lappas, B. Wie, C. McInnes, L. Tarabini, L. Gomes and K. Wallace, "Microsolar Sails for Earth Magnetotail Monitoring," *J. Spacecraft and Rockets,* vol. 44, no. 4, pp. 840-848, Aug. 2007.

[29] M. Whorton, G. Laue and C. Adams, "NanoSail-D: The First Flight Demonstration of Solar Sails for Nanosatellites," *Proc. 22nd Annual AIAA/USU Conference on Small Satellites*, Logan, Utah, 2008.

[30] S. Clark. (2010, July 26). *Falcon 1 Suffers Another Setback*[Online]. Available: http://spaceflightnow.com/falcon/003/

[31] J. Amos. (2010, Aug. 30). *Mini-Camera Pictures Japan's Ikaros Solar Sail*[Online]. Available: http://www.bbc.co.uk/news/10328584

[32] J. Ryall. (2010, Aug. 30). *Solar Sail Hybrid Launches Today from Japan*[Online]. Available: http://news.nationalgeographic.com/news/2010/05/100517-science-space-solar-sail-japan-ikaros-venus/

[33] Unknown. (2010, Aug. 30). *Ikaros Project*[Online]. Available: http://www.jspec.jaxa.jp/e/activity/ikaros.html

[34] M.J. Sidi, *Spacecraft Dynamics and Control: A Practical Engineering Approach*. Cambridge University Press, 1997.

[35] Unknown. (2010, Sept. 1). *Pointing Control System*[Online]. Available: http://hubble.nasa.gov/technology/pcs.php

[36] Unknown. (2010, Sept. 1). *HST - Hubble Space Telescope*[Online]. Available: hubble.nasa.gov/a_pdf/news/SM2-MediaGuide.pdf

[37] D. Sinclair, C.C. Grant and R.E. Zee, "Developing, Flying and Evolving a Canadian Microsatellite Reaction Wheel - Lessons Learned,", *Proc. 15th CASI Astronautics Conference*, Toronto, Canada, 2010.

[38] D. Sinclair, C.C. Grant and R.E. Zee, "Enabling Reaction Wheel Technology for High Performance Nanosatellite Attitude Control," *Proc. 21st Annual AIAA/USU Conference on Small Satellites*, Logan, Utah, 2007.

[39] P. Berlin, *Satellite Platform Design*, 5th ed. Department of Space Science, University of Lulea, Kiruna, Sweden, 2007.

[40] G. Maral, M. Bousquet and Z. Sun, *Satellite Communications Systems: Systems, Techniques and Technology*, 5th ed. John Wiley & Sons, Ltd., 2009.

[41] J.R. Wertz, *Spacecraft Attitude Determination and Control*. D. Reidel Publishing Company, Inc., 2002.

[42] W.H. Steyn, "A Multi-Mode Attitude Determination and Control System for Small Satellites," Ph.D. dissertation, Dept. Elect. and Electron. Eng., Stellenbosch Univ., Stellenbosch, South Africa, 1995.

[43] M.D. Shuster and S.D. Oh, "Three-Axis Attitude Determination from Vector Observations," *J. Guidance, Control and Dynamics*, vol. 4, no. 1, pp. 70-77, Feb. 1981.

[44] I.Y. Bar-Itzhack and J. Reiner, "Recursive Attitude Determination from Vector Observations: Direction Cosine Matrix Identification," *J. Guidance, Control, and Dynamics*, vol. 7, no. 1, pp. 51-56, Feb. 1984.

[45] N.G. Orr, J.K. Eyer, B.P. Larouche and R.E. Zee, "Precision Formation Flight: The CANX-4 and CANX-5 Dual Nanosatellite Mission," *Proc. The 4S Symposium - Small Satellites Systems and Services*, ESA-ESTEC, Noordwijk, The Netherlands, 2008.

[46] W.H. Steyn and Y. Hashida, "An Attitude Control System for a Low-Cost Earth Observation Satellite with Orbit Maintenance Capability," *Proc. 13th Annual AIAA/USU Conference on Small Satellites*, Logan, Utah, 1999.

[47] J. Schoonwinkel, "Attitude Determination and Control System of a Nanosatellite," M.S. thesis, Dept. Elect. and Electron. Eng., Stellenbosch Univ., Stellenbosch, South Africa, 2007.

[48] W.H. Steyn and V. Lappas, "Cubesat Solar Sail 3-Axis Stabilization Using Panel Translation and Magnetic Torquing," *Aerospace Science and Technology*, 2010, doi:10.1016/j.ast.2010.09.009

[49] W.T. Thompson, "Spin Stabilization of Attitude Against Gravity Torque," *J. Astronautical Sci.*, vol. 9, no. 1, pp. 31-33, 1962.

[50] M.J. Caruso, T. Bratland, C.H. Smith and R. Schneider. (2010, Nov. 11). *A New Perspective on Magnetic Field Sensing*[Online]. Available: http://www.ssec.honeywell.com/magnetic/datasheets/new_pers.pdf

[51] S.R. Ball, *Analog Interfacing to Embedded Microprocessors*, 2nd ed. Elsevier, 2004.

[52] K.R. Fowler, *Electronic Instrument Design: Architecting for the Life Cycle.* Oxford University Press, 1996.

[53] R.C. Jaeger and T.N. Blalock, *Microelectronic Circuit Design*, 2nd ed. McGraw Hill, 2003.

[54] J.F. Wakerley, *Digital Design: Principles and Practices*, 4th ed. Pearson Education Inc., 2006.

[55] W. Lan. (2010, June 2). *Poly Picosatellite Orbital Deployer Mk III ICD*[Online]. Available: http://cubesat.org/images/LaunchProviders/mkIII/p-pod%20mk%20iii%20icd.pdf

[56] R.C. Dorf and R.H. Bishop, *Modern Control Systems*, 10th ed. Pearson Prentice Hall, 2005.

[57] Unknown. (2010, May 23). *Design Guide - Module III*[Online]. Available: http://plastics.dupont.com/plastics/pdflit/americas/delrin/230323c.pdf

[58] Unknown. (2010, May 19). *Electropolishing - Useful Information for Stainless Steel Products*[Online]. Available: http://www.puresteel.co.za/info.html